INFORMATION TO USERS

This manuscript has been reproduced from the microfilm master. UMI films the text directly from the original or copy submitted. Thus, some thesis and dissertation copies are in typewriter face, while others may be from any type of computer printer.

The quality of this reproduction is dependent upon the quality of the copy submitted. Broken or indistinct print, colored or poor quality illustrations and photographs, print bleedthrough, substandard margins, and improper alignment can adversely affect reproduction.

In the unlikely event that the author did not send UMI a complete manuscript and there are missing pages, these will be noted. Also, if unauthorized copyright material had to be removed, a note will indicate the deletion.

Oversize materials (e.g., maps, drawings, charts) are reproduced by sectioning the original, beginning at the upper left-hand corner and continuing from left to right in equal sections with small overlaps. Each original is also photographed in one exposure and is included in reduced form at the back of the book.

Photographs included in the original manuscript have been reproduced xerographically in this copy. Higher quality 6" x 9" black and white photographic prints are available for any photographs or illustrations appearing in this copy for an additional charge. Contact UMI directly to order.

UMI

A Bell & Howell Information Company
300 North Zeeb Road, Ann Arbor MI 48106-1346 USA
313/761-4700 800/521-0600

EXPERIMENTS IN THE USE OF THE GLOBAL POSITIONING SYSTEM FOR SPACE VEHICLE RENDEZVOUS

A DISSERTATION
SUBMITTED TO THE DEPARTMENT OF ELECTRICAL ENGINEERING
AND THE COMMITTEE ON GRADUATE STUDIES
OF STANFORD UNIVERSITY
IN PARTIAL FULFILLMENT OF THE REQUIREMENTS
FOR THE DEGREE OF
DOCTOR OF PHILOSOPHY

Kurt Ronald Zimmerman
December 1996

I certify that I have read this dissertation and that in my opinion it is fully adequate, in scope and quality, as a dissertation for the degree of Doctor of Philosophy.

Robert H. Cannon, Jr.
Department of Aeronautics and Astronautics
(Principal Adviser)

I certify that I have read this dissertation and that in my opinion it is fully adequate, in scope and quality, as a dissertation for the degree of Doctor of Philosophy.

Gene F. Franklin
Department of Electrical Engineering

I certify that I have read this dissertation and that in my opinion it is fully adequate, in scope and quality, as a dissertation for the degree of Doctor of Philosophy.

Bradford W. Parkinson
Department of Aeronautics and Astronautics

I certify that I have read this dissertation and that in my opinion it is fully adequate, in scope and quality, as a dissertation for the degree of Doctor of Philosophy.

Mark A. Horowitz
Department of Electrical Engineering

I certify that I have read this dissertation and that in my opinion it is fully adequate, in scope and quality, as a dissertation for the degree of Doctor of Philosophy.

Jonathan P. How
Department of Aeronautics and Astronautics

Approved for the University Committee on Graduate Studies:

Abstract

Humanity's destiny in space is intimately tied to highly automated mechanisms, and as such, the ability for humans and machines to cooperate as an integrated team will determine the success of ambitious space missions of the future.

Autonomous vehicles are only as capable as the information afforded to them by their sensors, which has led to an ever increasing need for more advanced sensors. Technologies related to the Global Positioning System (GPS) have matured to the point where they are well suited for real-time control of autonomous vehicles both in space and terrestrially. This dissertation reports research performed in the Stanford Aerospace Robotics Lab to create and demonstrate new basic knowledge and techniques for using GPS to increase the sensing capabilities of free-flying space robots, and more generally, to explore how this advanced sensor can improve the capabilities of the human-robot team in space and on earth.

A comprehensive prototype system was built and demonstrated. The system consisted of a microcosm simulation of the space environment, two prototype space vehicles, consummate software systems, and an intuitive human-robot interface. The space environment was emulated through a constellation of GPS pseudo-satellites (pseudolites) and an air-bearing support system which provided the drag-free, zero-g characteristics of space in two dimensions for the prototype space vehicles. Proof-of-concept demonstrations showed that GPS sensing alone can be sufficient to perform precise intercept and capture of a free-floating target by an autonomous free-flying space robot. Other demonstrations showed how this type of sensor could enable unprecedented capabilities in space such as performing distributed science missions using several vehicles flying in formation.

The breakthrough of Differential Carrier Phase GPS technology, combined with the novel, inexpensive local GPS pseudo-satellite transmitters, enabled the successful in-lab demonstration of GPS-based control for precise robotic navigation. Since the experiments were carried out indoors where GPS satellite signals could not be received, the constellation of six GPS pseudolite transmitters was used exclusive of the NAVSTAR GPS satellites. The indoor GPS environment created by the close-range pseudolite transmitters required development of new algorithms for resolving vehicle positions and attitudes from the carrier phase measurements.

By performing these proof-of-concept experiments, many new arenas for application of GPS sensing have been conceived, ranging from the use of pseudolites for advanced space

missions to indoor sensing of mobile manufacturing robots. In addition, new methods for initializing and calibrating GPS sensors were developed, and future directions for increasing the utility of this type of sensor were identified.

To my family -
Ron L., Pat, Greg, Ron M., and Lynn,
without whose constant love and support
this endeavor would not have been possible.

Acknowledgments

Someone once said, "If I have seen farther than others, it is because I was standing on the shoulders of giants." Though this thesis may not have quite the impact of *Principia*, it does share in common the fact that it simply would not have been possible in the absence of the legacy of my predecessors. In that light, I am ever grateful to my principal advisor, Professor Robert H. Cannon, Jr., for the excellent research environment he has created and for the technical and philosophical guidance he has provided. That makes one shoulder. The other belongs to Professor Bradford W. Parkinson who had the insight to enable my graduate research by initiating the placement of the Global Positioning System way back when I was in elementary school.

I thank my reading committee, Professors Gene F. Franklin, Jonathan P. How and Mark A. Horowitz for their careful review of my dissertation and for their helpful suggestions throughout my work. I thank them, along with all of the superb and friendly professors at Stanford from whom I have taken courses over the years.

Just as my advisors have provided shoulders to stand upon, there are likewise distinguished pillars amongst former graduates who must be recognized. Marc Ullman and Clark Cohen set the precedent for this work. Marc not only designed and built the highly reliable robot system and related facilities, he more importantly instilled in me the "whole systems" engineering philosophy. Clark introduced me and a whole slew of impressionable graduate students to the seemingly magical powers of differential carrier phase GPS with his pioneering work in attitude determination using GPS. I thank him for his guidance along the way, as well as for leading a number of my peers who additionally served as a GPS support group.

Former ARL graduates Stan Schneider, Vince Chen, and Gerardo Pardo-Catellote are to be commended for their programming wizardry which has fortunately been encapsulated in the software tools used universally throughout the lab – including *ControlShell*, *StethoScope*, and the *Network Data Delivery Service*. It has been inspirational to see both their dedication to their work and their courage to bring it to market. I also need to thank Stan for providing valuable guidance when I entered Stanford as well as for giving me direction upon graduating from Stanford.

On the side of hardware wizardry, Stuart Cobb has never ceased to amaze me with the depth and breadth of his electronics knowledge and his practicality. The importance of his

GPS pseudolite transmitter design to this research is readily apparent and goes without saying. I thank Stu and the other members of the GPS lab, including Dave Lawrence, Paul Montgomery, and Harris Teague for collectively helping figure out how Clark did it.

The ARL's system administrators Denny Morse, Dave Meer, and Steve Ims, are the unsung heroes of the lab. Their work often goes unrecognized largely because they do it so well. Problems with the computer network are so *in*frequent that most users are unaware of the complexity of the system. I thank them for making the *sun-valley* network an invaluable engineering resource.

I thank office administrator Jane Lintott for offering me jelly beans, even when I gave her lots of work to do; electronics designer Godwin Zhang for nimbly wiring my electronics systems; mechanical designer Gad Shelaf for helping me design several components; and Aldo Rossi for machining my parts in less time than it took me to walk from the shop to the lab.

If I have been accused of being in graduate school for a long time, I would have to respond, "Why rush to depart such wonderful friendships?" Special friendships that have endured over the full duration of my stay at Stanford, listed in *reverse* alphabetical order, so as to not create jealousy, include Howard Wang, Ed Wilson, H.D. Stevens, Jeff Russakow, Tim McLain, Eric Miles, Dave Miles, Rick Marks, Gordon Hunt, Sanford Dickert and Young Man Cho. Recent friendships and camaraderie from the past include Bruce Woodley, Stef Sonck, Heidi Schubert, Bijan Sayyar-Rodsari, Larry Pfeffer, Kortney Leabourne – who made me run the hills, Hank Jones, Steve Fleisher, Bill Dickson, Andrew Conway, Bill Ballhaus, and Larry Alder.

Occasionally I ventured away from the lab. During those times I found myself amongst other friends, including my roommates over the years Jim Kramer, Andrew Daiber, and Paul Ning; members of "The Bullpen" Steve Merrihew and Salma Saaed; and running buddy and fellow musician Jim Reese. Thanks for sharing the best of times.

The National Science Foundation is appreciately acknowledged for funding my first three years of graduate studies, and NASA TRIWG is gratefully thanked for sponsoring this research under contract NCC 2-33-S18.

And most of all, I thank my family for being the beating heart amidst the shoulders, providing breath to my life with their ceaseless love, support, and encouragement. It is to them that I dedicate this body of work.

Contents

List of Figures

Chapter 1

Introduction

This dissertation presents theoretical and experimental investigations into the use of the Global Positioning System (GPS) as the sole feedback sensor for controlling the relative positions and attitudes of multiple space vehicles. A recent technique for extracting information from the GPS signal, known as Differential Carrier Phase GPS, can achieve measurement resolution down to the sub-centimeter level at bandwidths high enough for real-time automatic control. A complete prototype system was devised and used as a platform to perform proof-of-concept experiments. The culmination of these experiments was the precise intercept and capture of a free-flying target by a prototype autonomous free-flying space robot. The scope of this thesis encompasses the experimental demonstration of methods for using GPS for real-time control of autonomous systems and the use of GPS in unconventional manners, such as indoors, through the use of artificial GPS satellites or *pseudolites*.

1.1 Motivation

1.1.1 The Human-Robot Team in Space

The inception of the Mir and International Space Stations marks humankind's transition from routine visits into space to permanent extraterrestrial residence. As with the conquest of frontiers in the past, technological innovation, in the form of automated systems, will play the key role in establishing permanent human presence in space. The unprecedented challenges of space have severely limited our attempts to use mere extensions of terrestrial construction and maintenance practices in orbit. The incremental movement into space

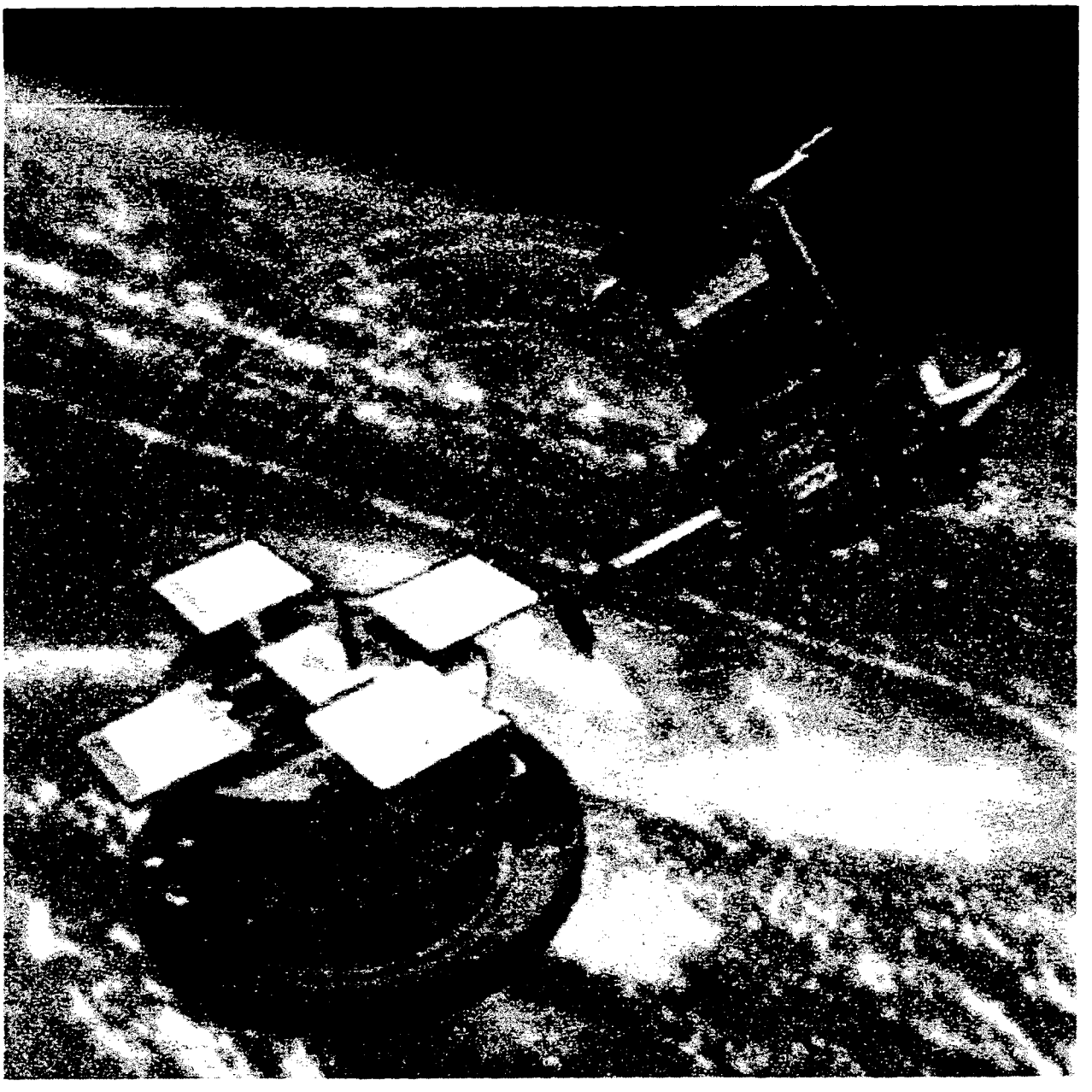

Figure 1.1: **Concept of an Autonomous Space Vehicle Retrieving a Satellite**

Under this scenario, both the robot and the satellite are equipped with GPS receivers. The GPS measurements made by the satellite are broadcast to the robot via a radio transmitter so that the robot can determine precise relative position and attitude.

is a consequence of the incremental change in the tools humans have used to perform work in space. For example, the human still needs to be physically present at the work site, working hands-on with the satellite, using derivatives of conventional terrestrial tools such as wrenches and screwdrivers that have been modified for space. The astronaut is encumbered by problems such as limited range of motion and reduced visibility imposed by a bulky space suit, unfamiliar work conditions, short work periods due to radiation risks, and high support costs of a large ground support team. A new tool – *the autonomous space robot* – will completely revise the way that humans work in space.

1.1.2 Task Level Control

Space robots working in Low Earth Orbit will be most effective if the human is employed at the supervisory level, directing *tasks*, while the robot manages the details of each task through local feedback control. For example, a human, working through a graphical world-model interface, would direct an assembly operation by merely indicating the parts to be assembled and how they should be assembled. The world model state is communicated to the robot (or robots), and the robot autonomously carries out the task through the use of stimulus-based strategic control and sensor-based feedback control. The robot continuously communicates its progress back to the world model interface, wherein the human – either nearby inside the space station or at great distance – can monitor the assembly process until it is completed [36] [45] [40] [15] [35].

This conceptual division of labor for the human-robot team, referred to as *Task Level Control*, is especially suited to the requirements, constraints, and characteristics of remote operation in Low Earth Orbit. Such considerations include: limited communications bandwidth, susceptibility to delayed and lost telemetry, well-understood dynamics and a fairly well-modeled environment. Typical operations include satellite retrieval, Orbital-Replacement-Unit (ORU) maintenance, and assembly of modules and truss structures.

The need for an effective means for directing space robots at a supervisory level has been recognized in studies such as [42]:

> [Current] space station robotic command and control procedures consume a great deal of IVA [Intra Vehicular Activity] time and thus reduce time available for other productive research and experiments. More efficient command and

control architectures are needed to reduce the on-orbit IVA time required for robotic operations.

Task Level Control is an effective paradigm for performing these operations, because humans currently are far better at visual perception, situation analysis, and task supervision, while robots excel at precision, repeatability, and speed.

The diversity of the operations that a robot can manage under the Task Level Control paradigm depends on the sophistication of its sensors, actuators, and control system. This thesis extends the versatility of Task Level Control through the development and intimate use of a novel sensor, the Differential Carrier Phase GPS receiver. In particular, Differential Carrier Phase GPS technology provides high-rate and punctual measurements of the relative position and orientation between multiple vehicles, thus enabling tasks such as autonomous rendezvous and multi-vehicle formation-flying. A conceptual photo of an autonomous space robot retrieving a satellite is depicted in Figure 1.1.

1.2 Research Goals

The research goals of this project were to address the issues discussed in the previous section, namely to develop from first principles a GPS-based generic system for sensing and controlling the relative positions and attitudes of multiple vehicles in space. Of course, the only way to fully test such a sensor is through a space flight experiment. However, flight experiments are expensive, difficult to garner, and typically not the first step one takes toward developing a fledgling technology. The first research goal, by necessity, was to develop an accurate experimental system with which to investigate GPS sensing and control issues *in the lab* well in advance of flying a mission. The research goals were:

- *Design a high-fidelity testbed* for studying autonomous free-flying vehicles with integrated real-time control and GPS sensing. A primary issue was to isolate and contain the GPS signal environment by recreating it in a laboratory setting. When using the NAVSTAR GPS, one must deal with the drawbacks of working outdoors such as unpredictable weather, motion of the satellites, intentional signal degradation, and the need for portable equipment. An important aspect of this system is the new characteristics of its near-field geometry compared with the essentially planar waves from NAVSTAR satellites.

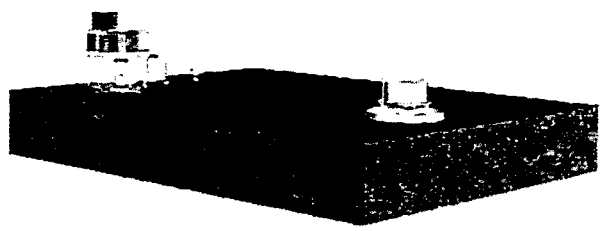

Figure 1.2: **Experiment Configuration: Scale Diagram**

This to-scale perspective diagram illustrates the configuration of the experimental apparatus used in this thesis. GPS signals are generated by six pseudolites distributed around the laboratory above the workspace of the vehicles. The robot combines its GPS measurements with the target's GPS measurements to estimate their relative position and attitude. With this real-time knowledge, the robot can be commanded to maintain a fixed formation with the target, or to rendezvous and capture the target.

- *Extend the state of current theory* of GPS sensing to include multiple vehicles, six degrees of freedom each, with near-field transmitters and *no fixed reference station.* (Existing algorithms were designed to handle attitude determination of a single vehicle with its position measured with respect to a *well-surveyed and fixed reference station.*)
- *Develop a generically reliable Differential Carrier Phase GPS sensor* and integrate it into a real-time control scheme for a multi-arm free-flying robot. Implicit in this goal is the broader need to investigate practical implementation issues such as calibration and initialization.
- *Experimentally demonstrate representative tasks* such as autonomous rendezvous and formation flying. These can be achieved only through successful integration of the sensor with the real-time control system.

The to-scale perspective diagram shown in Figure 1.2 illustrates the experimental apparatus constructed to achieve the stated goals. GPS signals are generated by six pseudolites distributed around the laboratory above the workspace of the vehicles. The robot combines its GPS measurements with the target's GPS measurements to estimate their relative position and attitude. With this real-time information, the robot can be commanded to rendezvous and capture the target. Vehicle mobility is achieved by floating on a cushion of air a few thousandths of an inch above an extremely flat and smooth granite air-bearing surface. This is done to simulate the zero-gravity, zero-drag conditions of space in two dimensions.

1.3 Fundamentals of the Global Positioning System

It is necessary to have some basic knowledge of the working principles of the Global Positioning System to understand the research issues addressed in this thesis, hence the following background is provided. Parkinson, et. al. [4] provides thorough coverage of the theory and applications of GPS. The term "Global Positioning System" generally refers to the NAVSTAR Global Positioning System. However, this thesis deals largely with novel uses of GPS (some of which are completely independent of the NAVSTAR system), so a distinction will be made between the NAVSTAR Global Positioning System and the other GPS-like systems investigated.

1.3.1 The NAVSTAR Global Positioning System

The NAVSTAR Global Positioning System consists of 24 satellites at an altitude of 20,300 km, traveling in circular orbits, and distributed in six orbital planes. Each of these satellites transmits a multi-component navigation signal shown schematically in Figure 1.3. The first three components, referred to as the L1 frequency components, are for civilian use, while the other two components, the L2 components, can be blocked from civil use by the U.S. Military at any time. For this reason, many commercial receivers operate on a single frequency and are designed to work exclusively with the L1 components of the GPS signal. Dual-frequency receivers can achieve better accuracies by taking advantage of the additional information supplied by the L2 component. The receivers used in this research project were single-frequency receivers, so only the L1 components of the GPS signal will be discussed further. Although dual-frequency receivers with the features required by this project do not yet exist, such receivers would likely change many aspects of this project.

All of the satellites in the NAVSTAR GPS constellation transmit on the L1 (1575.42 MHz) frequency band. The satellites are distinguished from one another through a spread spectrum technique involving modulation of the L1 carrier by a Pseudo-Random-Noise (PRN) Coarse Acquisition (C/A) code. This code is unique for each satellite and consists of a pseudo-random sequence 1023 bits long. A receiver can distinguish individual satellites by correlating the received signal with its own internal C/A code generator. The signal is additionally modulated by a 50 bits/sec data signal which contains, among other information, a time-of-broadcast tag.

1.3.2 GPS Sensing Techniques

A number of techniques, listed in Table 1.1, have been used to extract navigational information from the GPS signals.

- *Pseudo Ranging* - A receiver can compute the conventional pseudo-range estimate by taking measurements from four (or more) satellites to extract the four unknowns - three spatial dimensions and time. The received signals are subject to atmospheric distortions and intentional degradation known as Selective Availability, leading to accuracies in the range of 10 to 100m for this technique.

- *Differential GPS (DGPS)* - Relative positions between two local receivers can be obtained with greater accuracy (2 to 5 meters) by taking the difference between the two pseudo-range measurements. This technique is known as *Differential GPS*. Since atmospheric distortions are approximately the same for two local receivers, the differencing of the two positions removes distortion incurred errors.

- *Differential Carrier Phase GPS (DCP GPS)* - The Differential Carrier Phase technique involves reconstruction of the GPS carrier wave signal within the receiver [5]. The receiver phase-locks onto the signal and then measures the phase difference between antennas of the same receiver or between antennas of separate receivers. The basic principle is illustrated in Figure 1.4. Since the L1 carrier wavelength is 19.03 cm, the maximum achievable accuracy is 19.03 cm times the receiver phase resolution. Given that the phase resolution for the receiver used in this project is 256 samples per wavelength the theoretical accuracy is actually sub-millimeter (0.74 mm). In practice, though, several noise sources limit the typical accuracy to the centimeter level. One

Technique	Method	Accuracy	Special Requirements
Pseudo-range GPS (time-of-flight)	Measure signal TOF from each satellite	10-100m (absolute)	Susceptible to intentional degradation
Differential GPS (DGPS)	Take difference of the TOF measurements between two receivers	2-5m (relative)	Requires two local receivers with communication link
Differential Carrier Phase GPS (DCP GPS)	Reconstruct GPS carrier, measure phase diff. between two antennas	< 1cm (relative)	- Requires common oscillator, or synchronized receivers - Must solve integer ambiguity

Table 1.1: GPS Sensing Techniques

difficulty with this technique lies in determining the number of integer wavelengths within the total phase difference between the master and slave antennas. Differential Carrier Phase measurements can be made between two different receivers if the receivers are synchronized and the raw carrier phase measurements are accurately time-tagged.

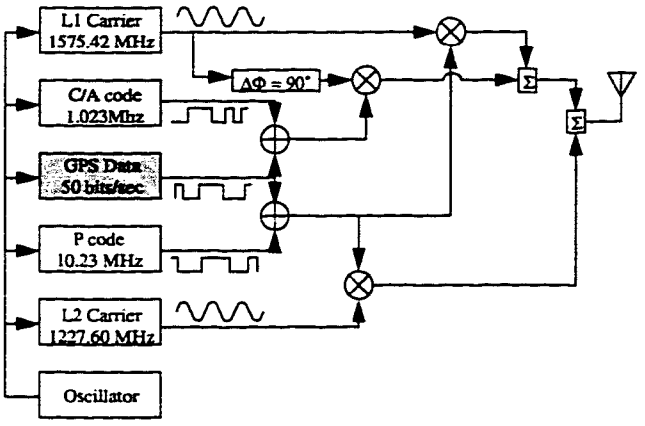

Figure 1.3: **GPS Signal Components**

1.4 Research Issues

The research issues pertinent to this thesis fall under two main categories. (1) *Sensing with a Pseudolite-based Positioning System* and (2) *GPS Sensing for Automatic Control.*

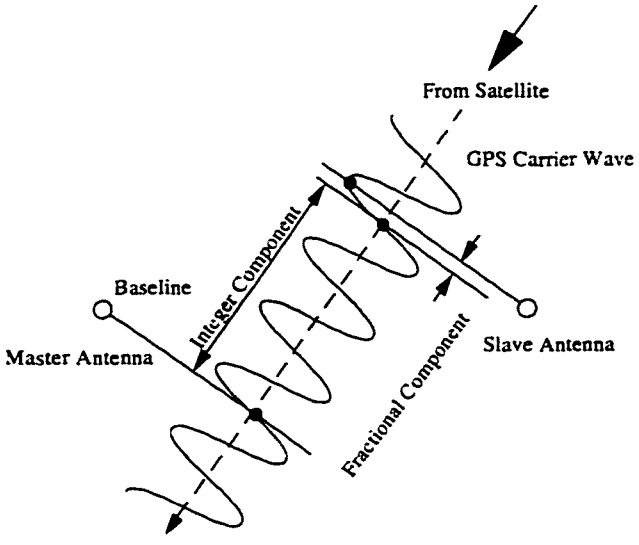

Figure 1.4: **Differential Carrier Phase GPS**

As previously stated, one of the primary objectives was to build a testbed to emulate GPS indoors; hence a number of research issues are related to the differences between the NAVSTAR GPS and the pseudolite-based indoor testbed. The primary distinction is the difference in proximity of the transmitters to the receivers. For this reason, the pseudolite-based system used in this thesis is referred to as a near-constellation pseudolite positioning system, while the NAVSTAR GPS is referred to as a far-constellation positioning system. A more explicit criteria form distinguishing between far- and near-constellation systems is provided in Chapter 2.

1.4.1 Sensing with a Pseudolite-based Positioning System

The prospect of using GPS indoors presents several fundamental problems, as first discussed in [50] and listed below:

- *No pseudo-range measurements* - Pseudo-range would be of limited use due to the relatively low accuracies attainable compared to the scale of the workspace. Therefore, in the interest of simplicity the pseudolites were not synchronized as would be required to calculate pseudo-range. This limitation prompted the reformulation of position and attitude algorithms *based on carrier-phase measurements alone.*

- *Spherical Wavefronts* - Since the transmitters are very close to the workspace, the assumption that the carrier wave advances as a plane is no longer valid. Instead, the wavefront must be treated as spherical. This leads to nonlinear phase measurement equations from which the position and attitudes must be derived.

- *Near-far problem* - The close proximity of the transmitting sources to the receivers leads to extreme variations in the power of the signal received as the vehicle traverses the workspace. The signal power of each of the pseudolites had to be carefully adjusted so that the signal power was within the dynamic range of receiver across the majority of the workspace.

- *Calibration of Pseudolite Positions and Antenna Baselines* - The locations of the phase centers of the pseudolite transmitter antennas and the vehicle receiver antennas need to be precisely determined in order to obtain accurate position solutions from the differential carrier phase measurements.

1.4.2 GPS Sensing for Automatic Control

Novel methods such as DCP GPS have enabled tight real-time feedback control, even though GPS was not nominally designed for this purpose. It is therefore necessary to employ clever methods to obtain reliable measurements from the GPS signals.

- *Loss of carrier phase tracking and integer cycle hand-off* - Carrier-phase tracking can be lost due to low signal strength or occlusion of the line-of-sight GPS signal by the vehicle's own structure or other nearby structures. This poses problems for real-time controllers for which measurement updates are expected every sample period. Whenever a pseudolite signal is lost or gained, the corresponding cycle ambiguity between antennas must be re-computed or "handed-off". This is done by calculating the *expected phase* from the most recent solution of the vehicle state propagated through a Kalman filter. Errors in the calculated *absolute* positions of the vehicles can lead to incorrect integer-cycle values during this process. The calculation of absolute positions of the vehicles are very sensitive to bias errors such as multipath, antenna phase center stability, and polarization of the GPS signal. Reduction of these sources of bias error is an ongoing area of research for improvement of this system.

- *High multipath environment* - Multipath (reflected signals) is recognized as one of the greatest detriments to the carrier phase measurements, and the problem is exacerbated in the indoor situation. Some existing techniques rely on the assumption that the multipath is repeatable, which is likely to be the case for a *single* spacecraft *in orbit* where multipath is created only by the vehicle's own structure [11]. However, for vehicles operating around disparate structures or other vehicles, the repeatability of the multipath is likely to be low, which may preclude the use of carrier-phase techniques.

1.5 Contributions

In meeting the goals of this research, the following contributions have been made to robotic sensing and control:

- A fundamental, quantitative understanding of the similarities and differences between far-constellation and near-constellation GPS was established and the theoretical basis for navigation using the latter was developed and shown experimentally. In order to study the critical aspects of the autonomous rendezvous problem, a fixed set of pseudolite transmitters was used inside a controlled laboratory environment. This first-ever indoor Global Positioning System provides sufficient similarity to the NAVSTAR Global Positioning System to study the autonomous rendezvous problem, but also has some differences that brought forth new challenges as well as new areas for application of GPS. The indoor GPS system offers a new form of simulation for developmental testing of space vehicles in an inexpensive manner that complements expensive GPS constellation simulators.

- GPS-based autonomous rendezvous between two free-flying vehicles was experimentally performed for the first time. Beyond demonstrating basic feasibility of using GPS for space operations, this proof-of-concept experiment exhibited typical tolerances that can be attained for autonomous space operations. This system can also serve as a guideline for designing space flight systems as it provides realistic specifications for parameters such as measurement update bandwidth, communication link contents and bandwidth, and computational requirements.

- Original techniques for integrating GPS sensor measurements with a real-time control system were devised. As noted above, GPS was not nominally designed to be used for tight real-time control. The raw GPS phase measurements were susceptible to corruption by multipath and loss of signal due to occlusion, vehicle configuration, limited dynamic range of the receiver, and multipath ambiguities. A series of signal processing steps in conjunction with a Kalman Filter were implemented to improve very significantly the reliability of the GPS sensor.

- A new theoretical formulation for relating carrier phase measurements to the positions and attitudes of two non-stationary vehicles was formed. The functional mapping is general and can be applied to both near-constellation as well as far-constellation systems. The functional mapping is characterized by geometric non-linearities introduced by the spherical-shaped wavefront emanating from each transmitter. These geometric non-linearities disappear as the distance between the transmitters and the receivers increases and the wavefronts tend toward planar, as in the far-constellation situation. Additionally, the mapping assumes no knowledge of pseudo-range, as this information was not available for the near-constellation GPS configuration used in this experiment. It is possible, however, to modify the implementation of this mapping to incorporate pseudo-range.

- A new method for synchronizing independent GPS receivers was developed using the concept of a "Master Pseudolite". This unique approach to synchronizing measurements from two disparate receivers was necessary so that differential phases between the two vehicles could be measured. The normal means for synchronizing receivers occurs in conjunction with pseudo-range determination. Since pseudo-range was not available from the indoor near-constellation, a new synchronization method was devised. This method could well be applied to future GPS-like systems described in Chapter 7.

- Innovative methods were introduced for calibrating antenna baselines and pseudolite positions. The custom-designed GPS environment required new methods for calibrating interdependent system parameters. Several approaches to calibrating transmitter and receiver antenna locations were investigated and analyzed for sensitivity to measurement errors.

- A new method was developed for resolving integer-cycle ambiguities between vehicles. This algorithm takes advantage of vehicle motion and near-constellation geometry to identify the cycle ambiguities. Initialization via measurement of signal power is also proposed. This capability could enable and motivate the use of near-constellation systems in space to augment the NAVSTAR GPS.

1.6 Related Research

This thesis would not have been possible without the foundations established by many other researchers. Diagram 1.5 shows the most relevant influences on this thesis, as well as future projects that are anticipated to benefit from this work.

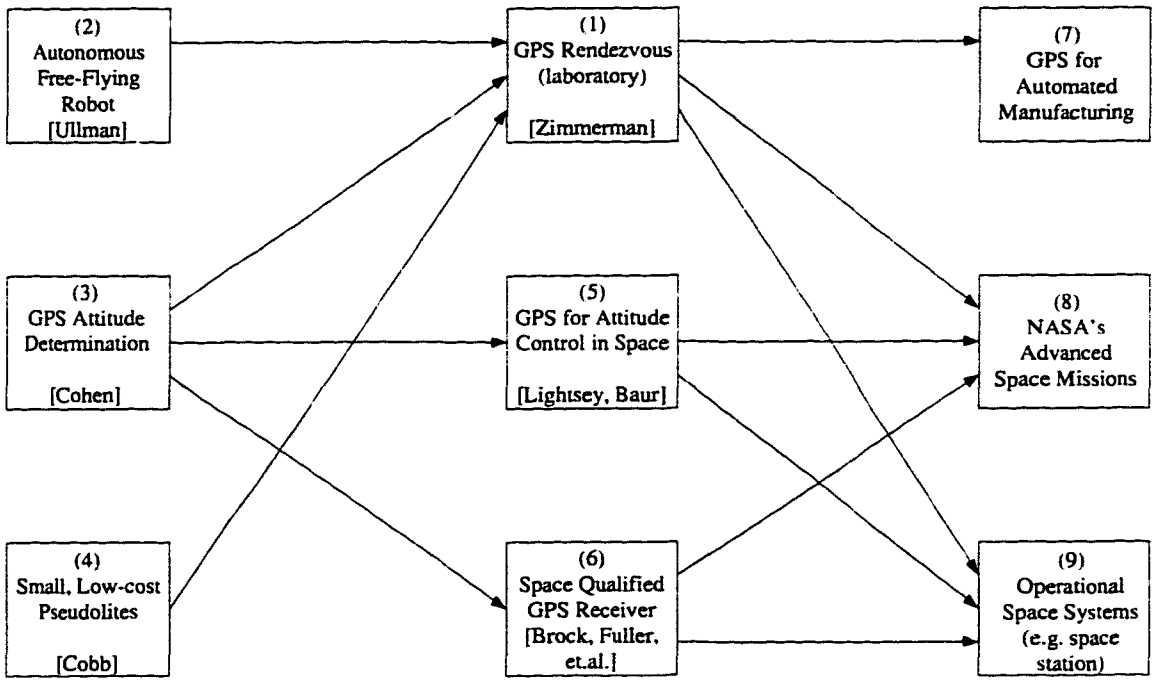

Figure 1.5: **Related Research Network**

This diagram shows how this research (1) benefited most directly from the works of Ullman (2), Cohen (3), and Cobb (4). In parallel with this effort, Lightsey and Bauer have investigated GPS attitude control in space, while Brock, Fuller, et. al. (6) have devised a space-qualified GPS receiver. These current projects will in turn benefit future applications such as GPS for automated manufacturing (7), NASA's major new advanced space projects (8), and operational space systems such as the International Space Station (9).

1.6.1 Predecessors

The approach to autonomous rendezvous pursued in this thesis was most directly influenced by the work of Ullman [45], Cohen [11], and Cobb [10].

Coordinated Control of a Multi-Arm Space Robot

In 1992, Ullman demonstrated coordinated control of a multi-arm free-flying space robot for rendezvous and capture of a free-floating target [45]. This pioneering work was successfully demonstrated through the use of an overhead vision sensing system which was employed to provide the positions and orientations of the robot and the target. A constraint of this vision system is that it operates in only two dimensions and requires an overhead, perpendicular view of fiducial markings on each object in the workspace[1].

The research presented in the present dissertation used Ullman's prototype space vehicle outfitted with a GPS sensor. Although the overhead vision system would not be practical for real space applications, a local vision system on-board the robot is a very realistic feature. The GPS system is therefore intended only to replace the overhead vision system as a more viable sensor for space. In the research reported here, data from the overhead vision system was still used as a means for evaluating the performance of the GPS system, but was not involved in controlling the spacecraft.

Recent GPS Innovations

Cohen devised the first GPS receiver for accurate attitude determination in 1992. Attitude determination via GPS had been attempted as early as 1983 on ships [23], but not until Cohen's work was there a system that could resolve attitude to a usable accuracy for any reasonable-sized spacecraft (less than 0.1 degrees for a 5 meter baseline). Cohen's work encompassed both the physical modification of commercial GPS hardware and derivation and implementation of new algorithms for attitude determination.

Shortly after Cohen's work, Cobb designed a small, low-cost, pseudolite transmitter that could produce the two primary components of the civilian GPS signal, i.e. the L1 carrier modulated by the C/A PRN code. The benefits of this design were not only its size and

[1]Kemper and Zimmerman expanded the vision system to track objects in three dimensions, six degrees of freedom. A summary of this algorithm is presented in Appendix C

cost, but also its simplicity[2]. Cobb's original pseudolite design could readily be modified to broadcast other components of the GPS signal to create a novel, customized GPS signal environment. These attributes made it possible to install a complete, low-cost, realistic, and easy-to-maintain GPS constellation in the laboratory.

1.6.2 Contemporaries

Amongst the contemporary research projects related to this thesis, there are those aimed at the same future applications, but investigating different GPS issues, and there are those working on similar GPS issues, but aimed at different future applications.

Similar applications, different issues

In 1989, Axelrad [1] investigated GPS for closed loop navigation of spacecraft, and in 1995 Lightsey advanced GPS space receiver algorithms to an *operational level* of flight-readiness. Lightsey's work complements this thesis work by addressing many of the on-orbit requirements for use of GPS for spacecraft attitude determination and control. His work does not, however, address the issue of *multi-vehicle control involving relative position*, as does this thesis. Lightsey, Bauer, et. al. are currently conducting space flight experiments to demonstrate GPS closed-loop attitude control in space [17]. Additionally, many of Lightsey's concepts have been incorporated into the first space-qualified attitude-determination receiver, developed by Space Systems Loral [3].

While this thesis addresses the problem of vehicle rendezvous from a closing distance of a few meters down to contact, Galdos and Upadhyay [22] and Montez and Zyla [52] have made theoretical studies on the use of Differential GPS for tracking rendezvous trajectories that close from several hundred kilometers down to a few meters.

Similar issues, different applications

Setting milestones in aviation history, Cohen, Pervan, et. al. [9], Conway [12], and Montgomery [27] addressed issues critical to integrating GPS sensing with real-time control of

[2]About 1/100th the volume of a commercial system of comparable performance at a cost of production less than one tenth the cost of a commercial system.

[3]The historical progression is as follows: Cohen modified Trimble Navigation's TANS receiver to be attitude capable, which became the commercial product known as the TANS Quadrex. The TANS Quadrex was then upgraded to perform attitude computations on-board the receiver, which became Trimble's TANS Vector. Space Systems Loral, under license from Trimble, revamped the TANS Vector into the first space-qualified receiver, the Loral Tensor [19].

autonomous aircraft. In 1994, Cohen, Pervan, et. al. devised a system that combined the NAVSTAR GPS with ground-based pseudolite "integrity beacons" to demonstrate autonomous landing of a commercial airliner, achieving accuracies well within Federal Aviation Administration (FAA) Category III (zero visibility) landing requirements. In 1995, Conway [12] demonstrated completely autonomous flight of a model helicopter using GPS as the only sensor, and in 1996 Montgomery [27] demonstrated autonomous takeoff, flight, and landing of a model airplane using GPS. Both Conway's and Montgomery's work differed from this project because they used NAVSTAR GPS signals, rather than pseudolites, and they used a fixed reference station at a surveyed location.

Teague [43] is currently studying GPS-based control of a large, flexible structure through the use of a pseudolite-only near-constellation very similar to the one used for this project.

1.6.3 Beneficiaries

NASA Applications

Support for the International Space Station and NASA's advanced space projects, including the New Millennium Program, both demand advances in sensors that can provide relative position and orientation information. It is clear that GPS can contribute greatly to these programs.

The International Space Station

The International Space Station (ISS) can take advantage of GPS in many ways, from the earliest stages of construction through full operation. The joining of station modules during construction will require knowledge of the relative positions and attitudes of the shuttle, the existing station structure, and the modules being attached. GPS sensors on each component could transmit data to a CAD-model display that the astronaut would use to direct and guide the module into place (e.g. in the hands of a large manipulator and free-flying robots). A similar system could be used for shuttle docking through construction phases and during normal operation of the station.

More importantly, GPS could be incorporated into free-flying autonomous space robots, as described in this thesis, to maintain the station. Reliability and accuracy of GPS sensors used near the space station could be greatly improved by placing a pseudolite-based

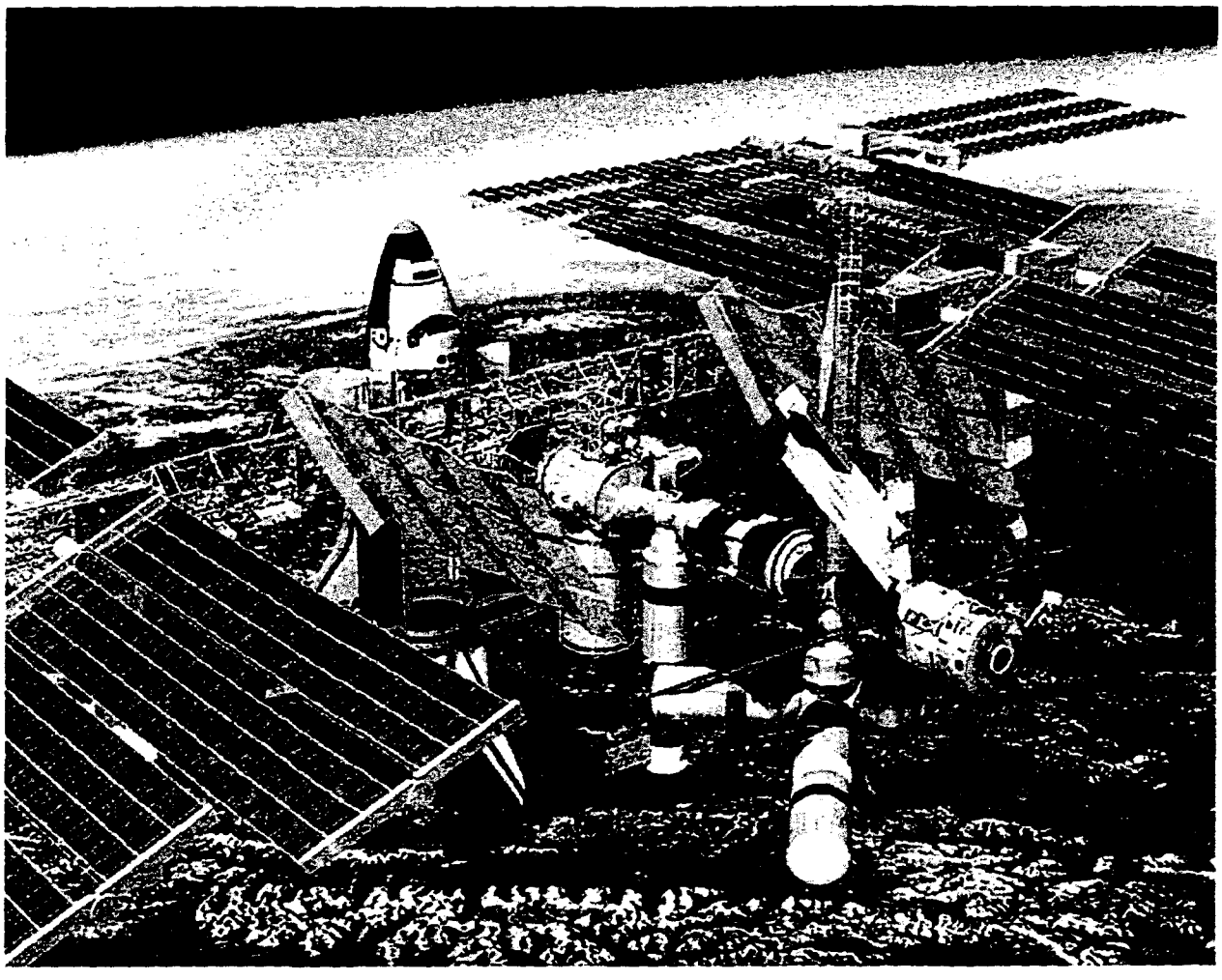

Figure 1.6: **The International Space Station**

The ISS can take advantage of GPS during construction and operational phases. Construction phases can use GPS for sensing modules as they are joined. Operational phase can use GPS for sensing robotic maintenance vehicles. Photo courtesy NASA

near-constellation positioning system on the space station structure itself to supplement the NAVSTAR GPS. Such a system would improve the sensor accuracy through better geometric resolution and would improve reliability by increasing the number of reference signals available when the NAVSTAR satellites become occluded by the space station structure itself. NASA is currently sponsoring two operational free-flying robotic vehicle projects directed toward space station maintenance, the Ranger Telerobotic Flight Experiment and

the Autonomous Extra-Vehicular Camera (AERCam). Both of these could potentially benefit directly from the contributions of this thesis.

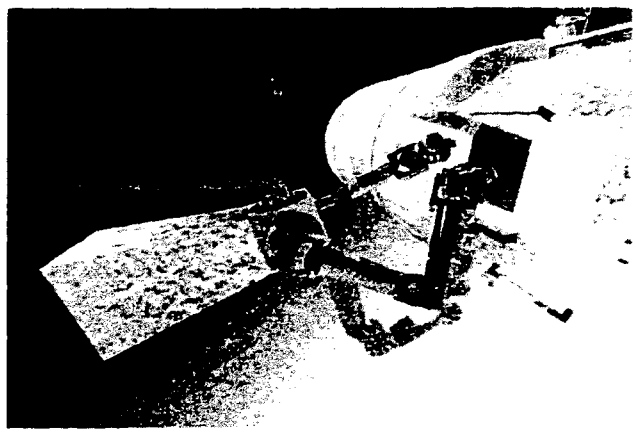

Figure 1.7: **The Ranger Telerobotic Flight Experiment**

The Ranger Telerobotic Flight Experiment is aimed at demonstrating the capability to perform space operations remotely from the ground. Photo courtesy the University of Maryland Space Systems Laboratory

The Ranger Telerobotic Flight Experiment

The Ranger Telerobotic Flight Experiment is a project to demonstrate the capability to perform space operations remotely from the ground. The Ranger Telerobotic Flight Experiment (TFX) is scheduled to demonstrate telerobotic spacecraft servicing in Earth orbit in early 1997. The Ranger TFX vehicle is a free-flying spacecraft equipped with four manipulators, which serve various functions for dextrous manipulation, grappling, and video viewing (see Figure 1.7).

The Autonomous Extra-Vehicular Activity Robotic Camera (AERCam)

The Autonomous EVA Robotic Camera is an effort to design a free-flying electronic camera that can be maneuvered to on-orbit positions in the vicinity of large spacecraft (such as the Space Station) to provide live video images for operations support.

AERCam is a small (45 to 90 Kg) free-flying unmanned platform capable of teleoperated or autonomous flight in close proximity to the Space Station and Shuttle Orbiter. It will

be able to hold position relative to, or fly trajectories about its target. Video images will be transmitted to the Station or to the ground for live viewing of its subject. It will be controlled from either the ground or from the Space Station and be capable of long periods of autonomous operation. The Aerospace Robotics Laboratory has proposed to incorporate GPS sensing schemes similar to the ones developed in this thesis to the AERCam, and this is in Johnson Space Flight Center's current planning.

NASA's Advanced Space Missions

NASA is pursuing several advanced space missions such as the New Millennium Program. The New Millenium Program is aimed at establishing a "virtual human presence" in space that will extend throughout the solar system and beyond. This "virtual presence" will be established by large numbers of small spacecraft, typically flying in clusters and capable of collecting distributed science data. A GPS-based near-constellation positioning system, similar to the system used in this research, is one method being pursued for autonomously regulating the formation of multi-spacecraft clusters.

Terrestrial Applications

For more than three decades, exploration of space has been the source of invention for a wealth of uncommon technologies, many of which have had surprisingly diverse application to terrestrial problems. Likewise, the technology pursued in this thesis has been identified as having potential contribution to terrestrial arenas. In particular, near-constellation positioning systems can be be applied to a number of indoor situations for sensing objects in three-dimensions, six degrees of freedom.

Manufacturing Systems

A general problem for companies that build very large systems, such as aircraft, is sensing the placement of massive components as they are moved around the factory and as they are joined to the finally assembly. In some sense, this is similar to the problem of bringing together the large modules of the space station. By outfitting the factory with a near-constellation positioning system and placing GPS receivers on each subassembly, it would be possible to monitor the location of these components as they are moved around the factory. This would enable autonomous delivery of sub-assemblies around the factory and

autonomous collision avoidance between sub-assemblies and other structures. This type of system has been considered for use in aircraft manufacturing plants, such as the Boeing facility depicted in Figure 1.8

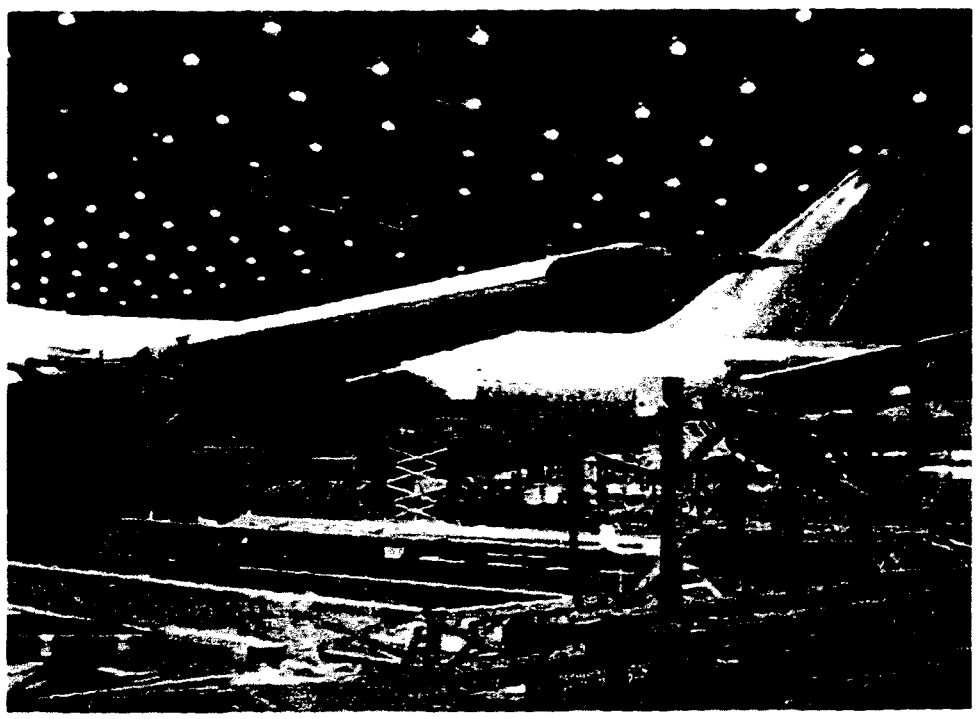

Figure 1.8: **Indoor GPS for Manufacturing**

Facilities such as Boeing's 747 plant are characterized by extensive high-bays and large system components that need to be transported over long distances throughout the construction process. An indoor GPS-based system could potentially be used to automate assembly processes in this type of manufacturing plant.

Indoor Robotic Systems

Indoor mobile robot systems are used extensively in research and are gaining increasing operational use in hospitals and warehouses for transporting items between different locations along designated routes. These systems currently use fixed tracks and/or acoustic sensors for navigation. Merging GPS with the existing sensors could increase the versatility and reliability of these systems.

Motion Picture Filming

A less apparent GPS application venue is in the filming industry. The indoor near-constellation positioning system could be used to monitor camera position and orientation during filming so that computer-generated special effects could quickly and easily be placed in the proper locations of the scene. Additionally, the autonomous helicopter work of Conway [12] could be applied to outdoor filming to obtain unprecedented camera view angles and pan trajectories.

Chapter 2

Experimental Apparatus

This chapter provides a description of the hardware system used to conduct the experiments reported in Chapter 4. The major components that are described include: the prototype free-flying space robot shown in Figure 2.2; the free-floating target vehicle; the GPS system, including the pseudolite constellation and the GPS receivers on-board the vehicles; the computer development environment; and the overhead vision system used to evaluate the performance of the GPS system. The interrelation of these system components is shown in Figure 2.1.

2.1 The Prototype Free-Flying Space Robot

The design and construction of the prototype free-flying space robot has been discussed in detail in past theses by Ullman [45], Koningstein [24], Dickson [15], and Jasper [20]. Portions of that system have been augmented for this thesis. The robot, depicted in Figure 2.2, is a self-contained autonomous vehicle, complete with on-board sensing, computing, communication, power, manipulation, and propulsion systems. On-board compressed air enables the robot to float just above the precisely-leveled granite surface plate (approximately 0.003 inch), providing a high-fidelity two-dimensional simulation of the drag-free, zero-gravity characteristics of space.

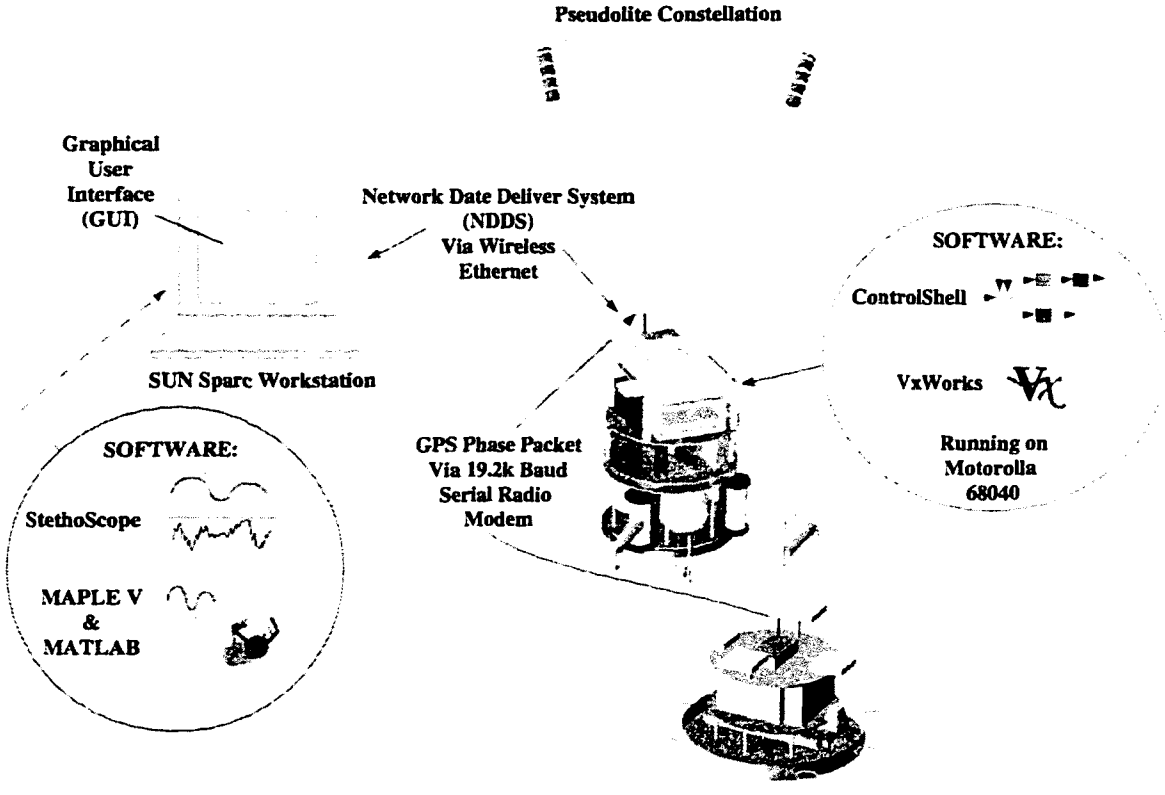

Figure 2.1: **Interrelation of the System Components**

2.1.1 Computer Architecture

The system architecture is based on a VME bus and utilizes a Motorola MVME 167-31A (68040) processor for all functions, including real-time control, communication with sensors and actuators, strategic planning, and communication with the operator interface. The control software is written in "C" and "C++" and was developed using $ControlShell^{TM}$ [38] and the $VxWorks^{TM}$ Operating System.

2.1.2 Communications

The robot's computer communicates with both GPS receivers (i.e. the one on the robot and the one on the target) through separate RS-232 serial ports at 19.2k baud. The serial link between the robot and the target is established by a Proxim 19.2k baud full-duplex

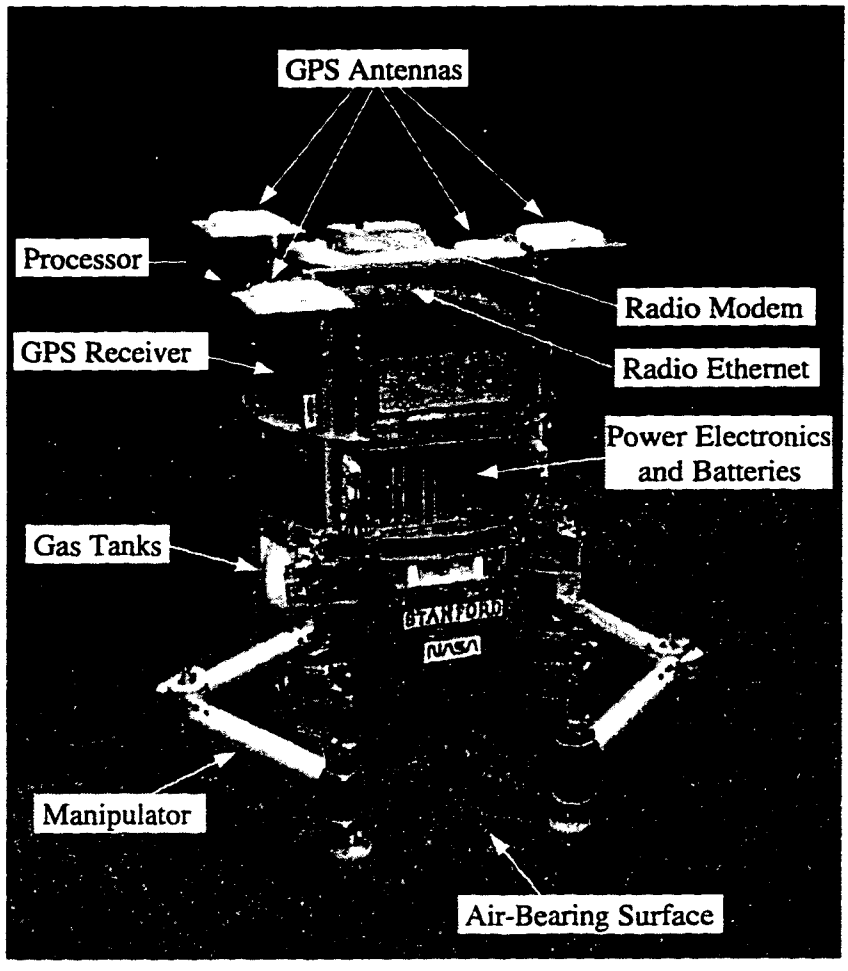

Figure 2.2: **ARL Free-Flying Space Robot**

radio modem. The data that is communicated across this link is listed in Table 2.1. Additionally, the robot is equipped with a Motorolla Altair radio Ethernet. This link is used for communication with the user interface during system operation and for downloading programs onto the robot during development[1]. Standard VME-bus A/D, D/A, and digital

[1]The radio Ethernet could have been used for the link between the robot and the target's GPS receiver, but at significant expense. Equipping the target with a radio Ethernet would have required the purchase of a new Ethernet unit and an upgrade of the units currently in place, at a cost of $7000. Additionally, the target would have required an interface computer between the GPS receiver and the radio Ethernet and additional power to support the computer, increasing the total cost to nearly $10,000. The alternative cost for the 19.2k baud modems totaled $200, though the communication delay incurred by these modems does restrict overall system performance.

I/O boards are used for communication to other system devices such as thruster solenoids, gripper pneumatics, arm motor drivers and RVDT angle sensors.

2.1.3 GPS Receiver

The robot and target vehicles are each equipped with a six-channel GPS receiver that is capable of multiplexing between four antennas. Each receiver can provide a total of 24 carrier phase measurements every sample. A constraint of the multiplexed antenna system is that all four antennas on a given receiver channel must track the same pseudolite signal. The receivers are commercial TANS Quadrex receivers from Trimble Navigation, with customized internal software.

The Trimble TANS Quadrex was modified as described below in order to meet the needs of this thesis research:

- Modified data packet protocol – The data packet protocol was optimized to minimize the transmission times between the full-duplex radio modems used to communicate information from the target vehicle to the robot. Simplex modems might have offered less data transmission delay since they can send packets byte-for-byte rather than as a quantized unit. However, such modems were not available at comparable baud rate and price.

- Changed contents of data packet – The TANS receiver is capable of transmitting one type of data packet at fixed time intervals, making it suitable for real-time control applications. The data nominally available in this packet was modified because the nominal information was not sufficient for the requirements of this system. The information transmitted by the GPS receivers is described in the next section below.

- Simplified the satellite search algorithm – The set of satellites that the receiver searches was fixed constant. This exploits the fact that the same satellites are always in view, and all antennas view the same satellites within the indoor pseudolite-based system. This modification alleviated this research project from issues studied by other researchers [25].

The receiver communicates via an RS-232 serial port at a rate of 19.2k baud. The information transmitted by each of the GPS receivers to the robot's computer is summarized in table 2.1. The table lists the information that is transmitted in one packet each sample

period (0.10 second). All quantities are listed in bytes. The nature of the information items is as follows:

1. The *Time Tag* data byte is an integer value that indicates the millisecond count (beyond the last whole second) at which the information in the data packet was sampled.

2. The *Carrier Phase of the Master Antenna* is a set of measurements of the raw carrier phases of each pseudolite signal, as measured at the master antenna. This information is used primarily to determine the relative positions of the two vehicles.

3. The *Differential Phases* measured by each of the slave antennas is the difference between the carrier phases measured at the master antenna and each of the slave antennas.

4. The *Signal to Noise Ratios* indicate how well each of the signals is being received, and are used as weighting factors in the computation of the vehicle state from the measured phases. There are a total of $N_{ant} \times N_{chan} = 24$ SNR values at each sample. Since these values do not change very rapidly, they are multiplexed in six sets of four to reduce the quantity of information in each packet, i.e. the SNR values for all four antennas for a single channel are updated every sixth sample.

5. The *Code Phase of the Master Pseudolite* is a quantity that is used to extrapolate the phase measurements of each receiver so that they can synchronize to the Master Pseudolite.

6. The *Phase Valid and Cycle Slip Flags* are indications of the receivers confidence in individual phase measurements. Only six bits of each of these bytes are used, one bit per receiver channel.

7. The additional *Packet Overhead* includes a single byte for the packet ID and a single byte that indicates the end of the packet.

Data	Quantity	Size Each [bytes]	Total Size [bytes]
Time Tag	1	2	2
Carrier Phase (master ant)	$N_{chan} = 6$	4	24
Differential Phase (slave ant)	$(N_{ant} - 1)$ x $N_{chan} = 18$	2	36
Signal to Noise Ratio	$N_{ant} = 4$ see note in text	1	4
Code Phase of Master Pseudolite	1	2	2
Phase Valid Flag	1	1	1
Cycle Slip Flag	1	1	1
Packet Overhead	2	1	2
Total			72

Table 2.1: GPS Receiver Data Packet Information

Packet Transmission Time Delay

The packet transmission time delay is greatest along the path from the target vehicle's GPS receiver to the robot's on-board computer. Since the radio modems are full-duplex, the data must be transmitted in serial in three stages: From the GPS receiver to the modem on the target vehicle, from the modem on the target vehicle to the modem on the robot, and from the modem on the robot to the on-board computer. The minimum packet transmission time delay can be calculated from the equation:

$$(10 \text{ bits/byte} \times N_{bytes\_per\_packet} \times N_{comm\_stages})/BAUD\_RATE$$

The modem baud rate used in this project was 19.2k baud. From table 2.1 there are 72 bytes/packet, and there are three communication stages. This results in a communication delay of 112.5 milliseconds, or just greater than one sample delay.

2.1.4 Propulsion

The robot can translate and rotate using a set of eight cold-gas thrusters that can produce approximately 1 Newton of force each. The thrusters are arranged in a square around the midsection of the robot as shown in Figure 2.3. Thrust is generated by momentarily

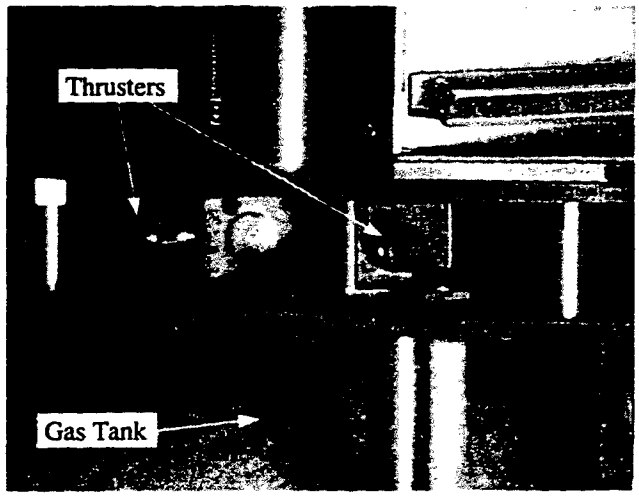

Figure 2.3: **Discrete Thruster Actuator**

opening a solenoid spool valve, releasing 100psi air through a nozzle to ambient for one sample period (0.10 second). Conventional control methods can be applied to these highly non-linear actuators through the use of astute techniques for mapping the continuous desired control forces and torques to the limited set available from the discrete actuators (see Ullman [45] and Wilson [47]).

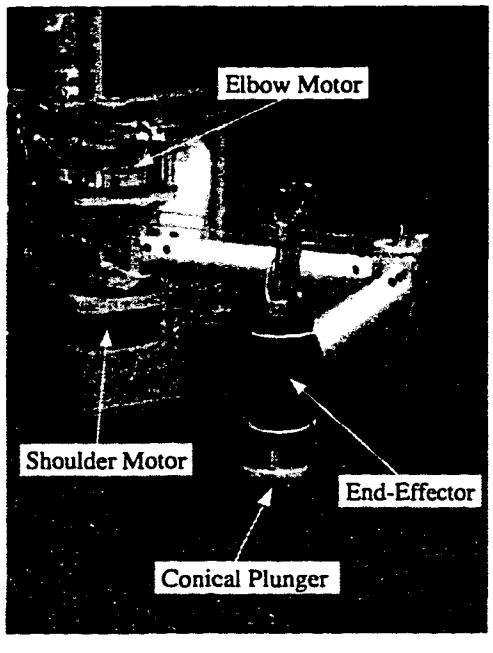

Figure 2.4: **Two Degree-of-Freedom Manipulator**

2.1.5 Manipulators

Each of the robot arms is a two degree-of-freedom SCARA-configuration (Selectively Compliant Assembly Robot Arm) manipulator that operates parallel to the air-bearing surface, as shown in Figure 2.4. Each degree of freedom of the manipulator is actuated by a limited-angle DC brushless motor mounted at the manipulator shoulder. Joint-angle information is supplied by two RVDT sensors mounted in line with the shoulder and elbow motor shafts. Position information is differentiated and filtered in analog to obtain clean joint-rate information.

The robot can grasp the target with its grippers by driving a conical-shaped plunger into the target gripper port. The plunger is driven up or down on a linear bearing by a pneumatic piston and cylinder. The clearance on each target gripper port is 5 cm, and the action of the gripper is displayed in Figure 2.5.

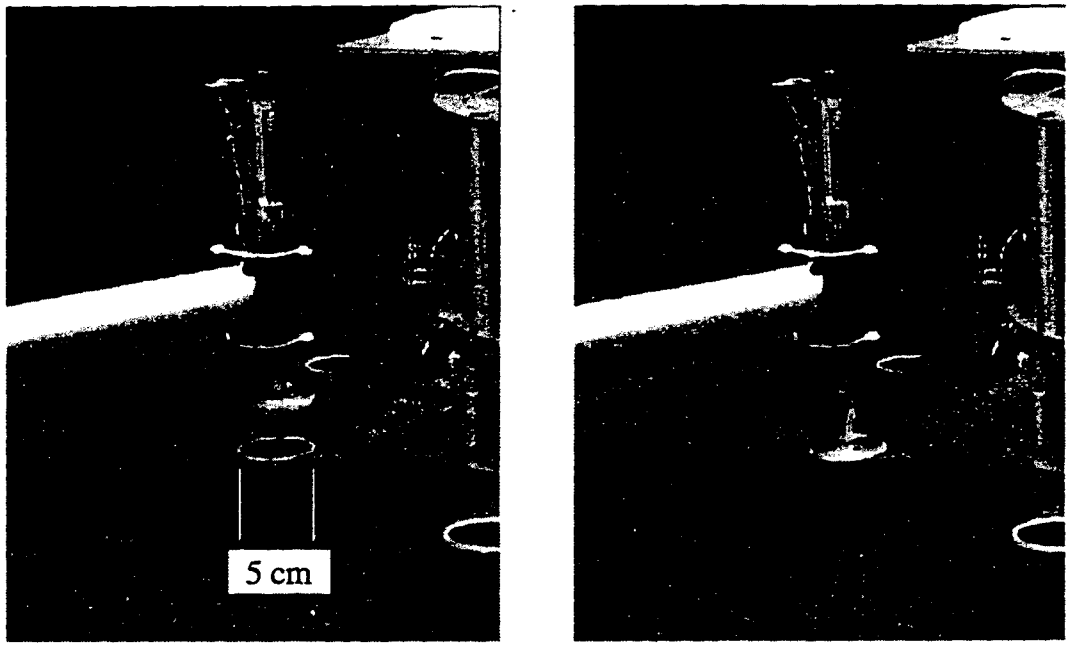

Figure 2.5: **Manipulator and Gripper**

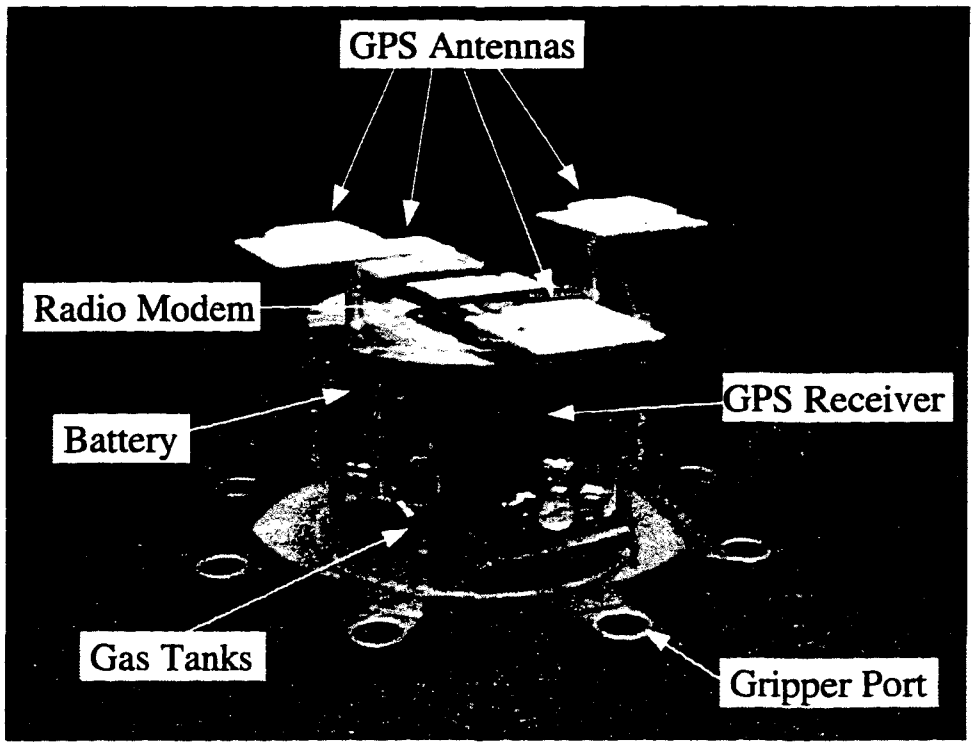

Figure 2.6: **Free-Floating Target Vehicle**

2.2 The Free-Floating Target Vehicle

The free-floating target vehicle, shown in Figure 2.6 is representative of a small satellite equipped with a GPS receiver. The target is a passive vehicle in the sense that it is not equipped with actuators nor processor. The target's only function is to take GPS phase measurements at each of its antennas and broadcast these measurements out through the radio modem. As with the GPS receiver on the robot, the data packets are sent every 0.10 second, and the information contained in each packet is listed in Table 2.1. The target is also equipped with on-board compressed air that enables it to float 0.003 inch above the granite surface plate. There are eight gripper ports distributed around the circumference of the target vehicle, each with a 5 cm diameter opening that the robot can latch with its grippers.

2.3 The Pseudolite-based Positioning System

2.3.1 Discussion on Positioning Systems

As discussed in Chapter 1, the method of using GPS in this thesis differed from conventional methods, and further unconventional methods are proposed in Chapter 7. Additionally, the growing use of GPS pseudolites and GPS simulators has made it possible to design testbeds, prototype systems, and even operational systems that are completely independent of the NAVSTAR GPS. It is therefore necessary to formalize some of the differences to clarify further discussions. The first distinction is between far- and near-constellation positioning systems. A simple conceptual distinction is that a system may need to be considered near-constellation when the baselines between receiver antennas measuring differential phases are comparable in magnitude to the distances between receiver antennas and transmitters. A formal definition is provided below.

Distinction between Far- and Near-Constellation Positioning Systems

A constellation of GPS-signal transmitters is deemed a far-constellation *if the wavefront of the signal is "sufficiently planar" throughout the entire workspace to be treated as a plane in all mathematical formulations.* Otherwise, the set of transmitters must be treated as a near-constellation. The condition for being "sufficiently planar" can be determined by an application-specific tolerance. Of course, a fundamental limit for the tolerance can be related to the receiver phase resolution. This limit is the point at which the receiver phase resolution equals the maximum error introduced by the planar wavefront approximation. At this point the receiver cannot discern the error introduced by the approximation.

A criterion for determining the maximum error introduced by the planar wavefront approximation is shown in Figure 2.7 and is described as follows:

> For any two points i and j in the workspace, the error between the actual differential phase that is measured, $\Delta\phi_{actual}$ and that which is supposed by the planar approximation $\Delta\phi_{approx}$ must be less than the tolerated error ϵ_{tol} for the approximation to be valid.

The analysis below provides the relations between the actual phase and the measured phase. The actual phase measured is simply the magnitude of the difference of the vectors

from each receiver to the satellite:

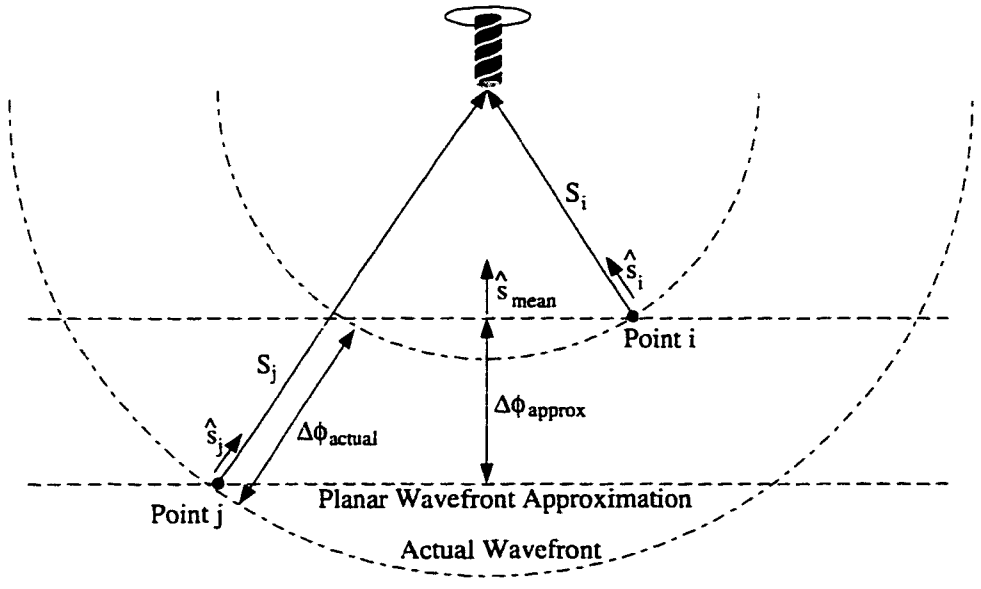

Figure 2.7: **Criterion For Validity of the Planar Wavefront Approximation**

$$\Delta\phi_{actual} = |S_i - S_j| \tag{2.1}$$

Where S_i is the vector from receiver i to a given satellite. For the planar approximation, a direction needs to be designated from which the waves are assumed to be advancing. A useful direction to assume is the mean of the two line-of-sight vectors from each of the points i and j, denoted as $\hat{s}_{mean}$. The phase difference approximation becomes:

$$\Delta\phi_{approx} = \hat{s}^T_{mean}(S_i - S_j) \tag{2.2}$$

The requirement for the planar wavefront approximation to hold is then:

$$|S_i - S_j| - \hat{s}^T_{mean}(S_i - S_j) < \epsilon_{tol}. \tag{2.3}$$

Distinction Between Synchronized and Unsynchronized Positioning Systems

The second distinction is between synchronized and unsynchronized positioning systems. A synchronized positioning system is one in which all of the transmitters are synchronized, such as the NAVSTAR GPS, while transmitters in an unsynchronized system are not rigorously maintained to a constant frequency or time base. The NAVSTAR GPS achieves synchronization through highly accurate atomic clocks on board each satellite which are maintained by the GPS Master Control facility located at Falcon Air Force Base in Colorado. An unsynchronized positioning system *cannot be used to derive pseudo-range*, but can supply carrier phase measurements. Had it been necessary, the pseudolites used for this project could have been synchronized by using a common oscillator to generate the L1 carrier for every transmitter. This could have been done by connecting all of the pseudolites to one single oscillator, but would have required considerable effort to account for and maintain exact transmission line delays between the oscillator and each transmitter.

Distinction Between Pseudolite Systems and Simulators

Finally, a discussion is provided here to explain the difference between pseudolite-based systems and simulators. The conceptual difference is primarily in the intended application of each, although they do have a high degree of functional equivalence. Pseudolites are generally used to supplement the NAVSTAR GPS constellation to provide improved geometric observability for carrier phase measurements by broadcasting a signal throughout a limited portion of the workspace volume. Simulators, on the other hand, are typically used for receiver development and algorithm testing via direct connection to the receiver. As such, they can mimic many aspects of the NAVSTAR constellation, including satellite Doppler, ephemeris, and availability.

The basic pseudolites used in this thesis provided a subset of the functionality of a GPS simulator, but at a fraction of the cost and volume[2]. Advanced pseudolites, discussed in detail by Cobb [10], have features not present in simulators, including:

- A pulsing capability which essentially eliminates the near-far problem, a common characteristic of applications that use pseudolites.

[2]Pseudolites cost on the order of a thousand dollars and fit into a package $200cm^3$, compared to several *hundred* thousand for a simulator that occupies a space of $65,000cm^3$.

- The ability to broadcast custom data messages at higher rates than the 50 bits/sec NAVSTAR-ICD200 specification [29].
- A self-surveying feature, enabled by combining the pseudolite with a GPS receiver.

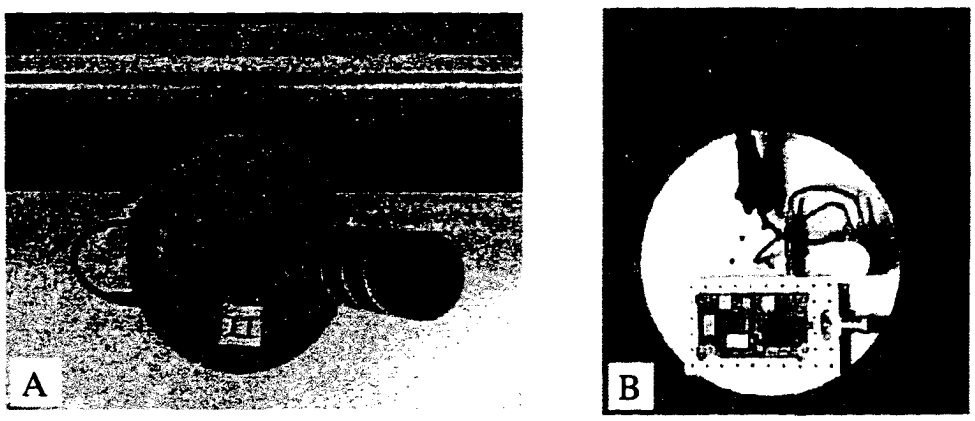

Figure 2.8: **Pseudolite Transmitter**

As both of these two distinct technologies mature, their functionality will likely continue to diverge due to the differences in their intended use.

2.3.2 The Pseudolite Constellation

A near-constellation, unsynchronized positioning system was used for this research. The constellation consists of six independent pseudolites. Each pseudolite produces an L1 (1.575 GHz) carrier phase signal modulated by its own unique C/A code. One pseudolite, designated as the "Master Pseudolite", serves as a time reference for synchronizing *the receivers.* The "Master Pseudolite" differs from the other pseudolites in that it broadcasts an additional signal component, the 50 bit/sec GPS data message (see Figure 1.3). Note that *the pseudolite transmitters themselves are not synchronized* – only the receivers are synchronized. Receiver synchronization is accomplished by aligning to the bit transition edges of the 50 bits/sec data message of the Master Pseudolite.

Figure 2.8(A) shows a mounted pseudolite (broadcasting as PRN 11). The pseudolite is completely self-contained, and can be mounted anywhere around the room on a standard track-lighting fixture which supplies power at 12V. Figure 2.8(B) shows the circuitry of a

GPS pseudolite transmitter box as it is mounted on the back of the helical antenna. For size reference, the ground plate of the antenna is 8.5 inches in diameter. The transmitter electronics board was designed by Cobb of the Stanford GPS Laboratory for use on the Integrity Beacon Landing System for aircraft [8]. The antenna is designed to broadcast L1 in the normal mode, and is characterized by a conical beam pattern.

2.3.3 The Helical Transmitter Antennas

It was important to minimize the effects of multipath at the outset of this research. Patch antennas with hemispherical beam patterns were tested in early experiments and were shown to produce excessive amounts of multipath (signal reflections) from walls and objects. This was evidenced by frequent cycle slips in the receiver carrier phase tracking and large variations in the signal-to-noise ratios as the receiver antenna was moved around. Large signal-to-noise variations for small displacements (a couple of wavelengths) are often an indication of multipath, as the line-of-sight and reflected signals interfere in constructive and destructive manners. Helical antennas were chosen as a practical alternative to patch antennas. Some of the compelling reasons for using helical antennas are listed below:

- Helical antennas are easy to construct and are robust to variations in dimensions. This minimized construction costs, which was important since at least six antennas were needed.
- The beam pattern of helical antennas can easily be adjusted. Control of an antenna's radiated beam pattern enables some control over multipath. For a helical antenna, the beam width can readily be adjusted merely by changing the length of the helix.
- The signal characteristics of helical antennas are well known. The phase measured by the receiver antenna is a function of the phase characteristics of both the transmitter antenna and the receiver antenna. Since the phase characteristics of a helical antenna are well known, the impact of certain effects such as phase polarization can be analyzed. Likewise, knowledge of the beam power characteristics can be incorporated into integer resolution algorithms. The large variation in signal power that causes severe near-far problems can actually be used advantageously in integer resolution algorithms.

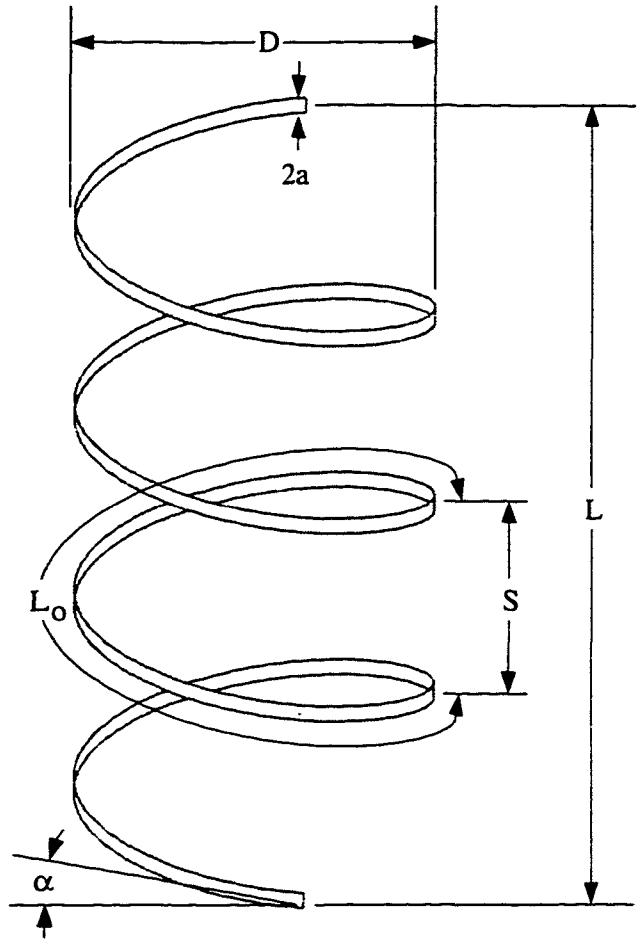

Figure 2.9: **Helical Antenna Parameter Definitions**

The helical antennas were custom built from inexpensive, readily available materials, including ABS plastic tubing (typically used for drainage pipes) and aluminum tape. The antennas were designed to broadcast the GPS L1 frequency in the *axial* or *endfire mode*, as described in Balanis [2]. Figure 2.9 shows the parameter definitions for this type of antenna. Design parameters for the helical antennas used in these experiments are listed in Table 2.2.

The lengths of the antennas were chosen through an empirical, iterative process. The antennas were originally designed with a rather narrow beam width (30°) to insure reduced multipath, and then they were repeatedly shortened, widening the beam width until each pseudolite could be received over the majority of the workspace. A means for theoretically

Parameter	Symbol/Relationship	Value
Antenna Length	$L = NS$	13.50 cm, 20.25 cm
Conductor Length per Turn	$L_0 = \sqrt{S^2 + C^2}$	19.50 cm
Signal Wavelength	λ	19.03 cm
Diameter	D	6.05 cm
Circumference	$C = \pi D$	19.01 cm
Number of Turns	N	3.08, 4.62
Spacing	S	4.38 cm
Pitch Angle	$\alpha = \arctan \frac{S}{C}$	13^o
Conductor Diameter	$2a$	0.6 cm
Half Power Beam Width (degrees)	$HPBW \simeq \frac{52\lambda^{3/2}}{C\sqrt{NS}}$	$61.8^o, 50.5^o$
First Null Beam Width (degrees)	$FNBW \simeq \frac{115\lambda^{3/2}}{C\sqrt{NS}}$	$137^o, 112^o$
Input Impedance	$R \simeq 140(\frac{C}{\lambda})$	140Ω
Axial Ratio	$AR = \frac{2N+1}{2N}$	1.16, 1.11
Directivity	$D_0 \simeq 15N\frac{C^2S}{\lambda^3}$	10.6, 15.9

Table 2.2: Helical Antenna Parameters

determining the optimum antenna length and direction could be derived through consideration of the far-field pattern in conjunction with the workspace volume. In such an analysis, one would attempt to maximize the workspace volume that has a signal strength within the dynamic range of the receiver.

The empirically selected value for the half-power beam width (HPBW) was 61.8^o for the Master Pseudolite mounted directly over the workspace, and 50.5^o degrees for the other five pseudolites around the periphery. These values correspond to antenna lengths of 13.50 cm and 20.25 cm, respectively.

2.4 The Development Environment

Although the least visible component, the development environment is perhaps the most important aspect of the experimental system, as it is the conduit through which the engineer makes the magic happen.

At the highest level, this system was developed using *ControlShell*^{TM}, a Computer Aided Software Engineering (CASE) platform invented by Schneider at the ARL and developed by Real-Time Innovations, Inc. [37] [33]. *ControlShell* was used to diagrammatically build the

dynamic and strategic control software. Code generated by ControlShell operates within the context of the *VxWorks*^{TM} real-time operating system. All of the real-time code was developed in C and C++ on Sun workstations and then cross-compiled for execution on the MVME167-33MHz (Motorolla 68040) processor on-board the robot.

Algorithms for deducing the vehicle-state from GPS phase measurements (discussed in Chapter 3) were derived automatically with *Maple V*, an interactive symbolic algebra system by Waterloo Maple Software. Another powerful feature of *Maple V* that was employed was its ability to directly convert the derived symbolic equations into efficient C code. The auto-generated C code was then inserted directly into the component module code generated by *ControlShell*. This same code was incorporated into MathWorks *MATLAB*^{TM} for simulation and testing independent of the robot hardware.

Communication between the Sun workstation and the free-flying space robot was established through the *Network Data Delivery Service*^{TM} (*NDDS*), created by Real-Time Innovations, Inc. The information routed via *NDDS* included robot commands sent from the operator interface to the robot (such as *move to position* (x, y)), and vehicle state information sent from the robot to the operator interface. *NDDS* is a subscription-based communications package developed for Ethernet communication between distributed, heterogeneous machines in a real-time environment [34] [31].

The vehicle state information was displayed on the workstation through a graphical, 3D operator interface that was designed using *DevGuide*^{TM} by Sun Microsystems and *Graphigs*, a Phigs-based graphics library developed at ARL[3].

StethoScope^{TM} [32], another product from Real-Time Innovations, Inc., enabled real-time viewing of system signals and data as the experiments were running. This invaluable capability reduced to a minimum the time required for debugging, data collection, and data analysis.

2.5 The Overhead Vision System

Complete evaluation of the performance of any sensor requires some independent "truth" measurement for comparison. For this research, an overhead vision system capable of tracking the robot and target vehicles in two-dimensions was used as a truth measurement. The

[3]Snapshots of the user interface Graphigs models were directly used to create figures for this document. See Figures 1.2 and 2.1.

vision system can track the vehicles at 60 Hz, with an absolute accuracy estimated at better than 2 cm over the entire workspace and static noise of less than 1 mm [6] [45].

Chapter 3

GPS For Real-Time Control

An important set of contributions of this thesis are comprised in the original techniques developed for integrating GPS sensor measurements with real-time control systems. As indicated in the research issues discussed in Chapter 1, the Global Positioning System was not nominally designed for tight real-time feedback control. Knowledge of the dynamics of the system can be used to integrate the controller with the sensor to improve the robustness of the overall system. Others have demonstrated real-time control with GPS [12] [27] [9]. This research reported here is new and different in that it:

- Required a new theoretical formulation to handle attitude and relative position of two vehicles with no fixed reference.
- Dealt with a fundamentally different ensemble of measurements characterized by spherical wavefront and no direct pseudo-range measurement.
- Required a new way for synchronizing independent receivers, since the low-cost transmitters are not themselves synchronized.
- Had to handle signal loss and corruption in new ways due to the greater extent of multipath and higher occurrence of occlusion.

It is these issues that are explored in this chapter.

3.1 The Control System Software

The primary software components of the control system are depicted in Figure 3.1, which provides a high-level schematic of the control structure along with a magnified view of the GPS Sensors and signal processing software. The state vector x in the upper control diagram is the physical state of the system, which includes the position, orientation, velocity, and angular rates of both vehicles. $\hat{x}$, x_{com}, and x_{err} are the estimated state, the commanded state, and the state error of the system respectively. The controller is a simple Proportional plus Derivative (PD) control algorithm, from which the control forces and torques, u, for the robot base and manipulators are generated.

The GPS sensor software is divided into several major components, each of which will be discussed throughout this chapter. These components are comparable to the *ControlShell* components in the actual implementation. The *implicit* input to the GPS Sensor component is the physical state of the system, which can be considered to be transformed by the GPS receivers into carrier phase measurements ϕ_0 and ϕ_1.

The GPS Receiver Components

The *GPS Receiver Components* are device-driver software modules that interface to the physical GPS receiver hardware through two independent serial ports on the real-time computer. In addition to the carrier phases, the *GPS Receiver Components* produce several measurements that are used in further signal processing steps. The measurement time-tags, τ, are used to align measurements from each receiver for computation of phase differences. The master pseudolite code phases, r, are used to compute time biases of each receiver which in turn are used to improve the phase differences. Finally, the signal-to-noise ratios (not explicitly shown in the diagram) are used to determine weighting values for each of phase measurements during the process of estimating the vehicle states from the phases.

The Phase Difference Component

The *Phase Difference Component* computes phase differences and time bias corrections from the time-tagged carrier phase measurements, and code phases. There are two types of phase differences computed: those between antennas on the *same* vehicle, and those between antennas of *different* vehicles. These are referred to as *intra-vehicle phase differences* and *inter-vehicle phase differences*, respectively. The intra-vehicle phase differences $\Delta\phi$ are

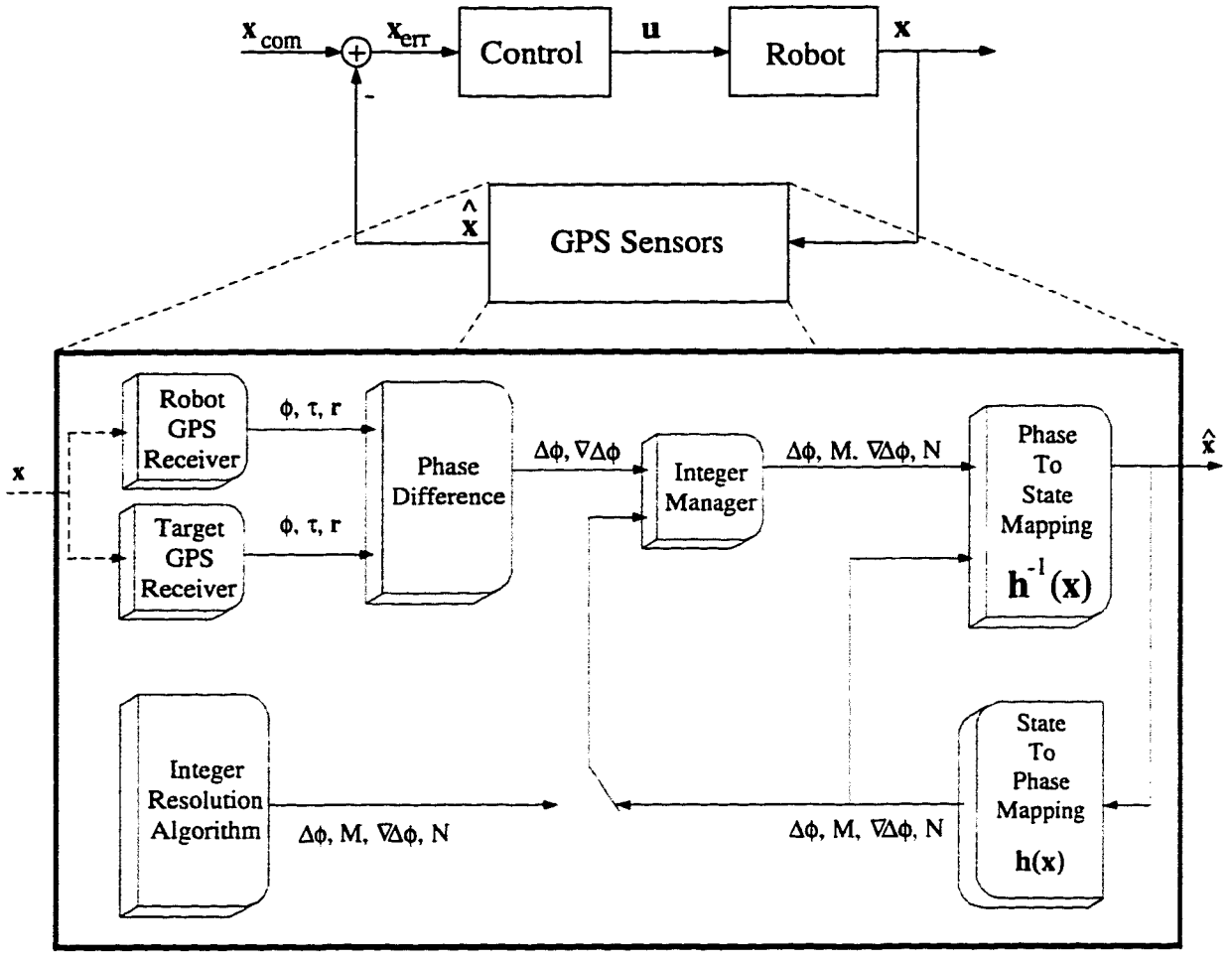

Figure 3.1: **GPS Signal Flow Diagram**

The flow of information through the GPS sensor software algorithms is shown in this diagram. Each block represents a software component or module in the object-oriented programming sense. The "switch" on the State-to-Phase Mapping Component *signal indicates that this module is active during normal operation, while the* Integer Resolution Component *is active at startup to initialize the integer cycle ambiguities.*

derived from a single difference between two carrier phase measurements, while the inter-vehicle phase differences $\nabla\Delta\phi$ are derived from four carrier phase measurements through a method known as double differencing [46].

The scheme for managing different configurations of tracked pseudolites also takes place within the *Phase Difference Component.* It is possible for the receivers to lose track of

individual pseudolites as the vehicle traverses the workspace. This affects which carrier phase signals ϕ are used in the computation of the phase differences $\Delta\phi$ and $\nabla\Delta\phi$, and it also changes the values of the inter-vehicle integers, since the phase differences are computed from different sets of pseudolite signals. The configuration management scheme primarily affects the order and sizes of the vectors displayed as signal lines on the signal flow diagram.

The Integer Manager Component

The differential phase measurements relate only the *fractional* component of the distance between any two antennas (as was indicated in Figure 1.3). The *Integer Manager Component* converts the *phase measurement* to a *range measurement* by adding and maintaining the whole integer cycles of the signal. As with the phase measurements, there are two types of integer cycles: those between antennas on the *same* vehicle, and those between antennas of *different* vehicles. Likewise, these are referred to as *intra-vehicle integers* and *inter-vehicle integers*, respectively.

The Phase-to-State Mapping Component

Once the fractional phases and the integer cycles are known, the *full phases* are mapped to the *state variables* by the *Phase-to-State Mapping Component*. This component computes the mapping $h^{-1}(x)$, (which is the inverse of the nonlinear *State-to-Phase* mapping, $h(x)$) through a recursive least squares algorithm. The mapping from state variables to phases, $h(x)$, is characterized by several nonlinearities which are discussed further in Section 3.2. The *State-to-Phase Component* computes the predicted phases from the current state for feedback to the recursive least squares *Phase-to-State Component* and for consistency checking within the *Integer Manager Component*.

The Integer Resolution Component

The last major component of the system is the *Integer Resolution Component*. This component is only active during initialization. Once the integers M and N are known, feedback through the *State-to-Phase Mapping* is used to maintain these numbers. A motion-based method for resolving the integers was developed and demonstrated in simulation. This algorithm is discussed in Chapter 5. In the experimental implementation, the system was initialized using the overhead vision system, which provided immediate measurements of

both vehicles positions and orientations, from which the corresponding initial integers and phases were derived.

The following sections delve into more detailed explanations of the major components of the system. The detailed explanations are presented in order of component sophistication rather than in order of data flow, as they were heretofore presented.

3.2 The Phase-to-State Mapping Component

The *Phase to State Mapping Component* estimates the state of the system based on the phase measurements. There are many different ways that this can be done, and the most complete approach is to apply a full-dynamic model-based extended Kalman filter to the non-linear phase measurements to derive the state. Limited computing resources, in conjunction with diminishing returns on performance verses complexity, entail a certain amount of simplification to this approach. The most complete model for the system studied in this thesis, *maintaining full generality in three dimensions*, involves 20 states for the robot (ten degrees of freedom including the arms), and 12 states for the target (six DOF). This is more than necessary to accurately estimate the system state, and places exorbitant requirements on the computer resources. It was therefore necessary to simplify the means by which the state was computed from the phases, while maintaining reasonable performance. Diagram 3.2 shows the deduction of simpler models, the process of which is described below.

3.2.1 Model Simplifications

Neglecting Manipulator Dynamics

The first simplification assumes that the robot is a rigid body, i.e. the arms do not appreciably affect the dynamics of the base (model A). It has been shown that the dynamic coupling of the arms to the base is noticeable, and can be incorporated into a full system controller for better system performance [35] [24] [45], but the improvement in performance has been traded off to afford simpler equations of motion for this work. With this assumption, the system requires twelve states for the robot and twelve states for the target. Additionally, the system dynamic equations will be non-linear, due to the three-dimensional rotational equations of motion for each of the vehicles ("Euler Equations").

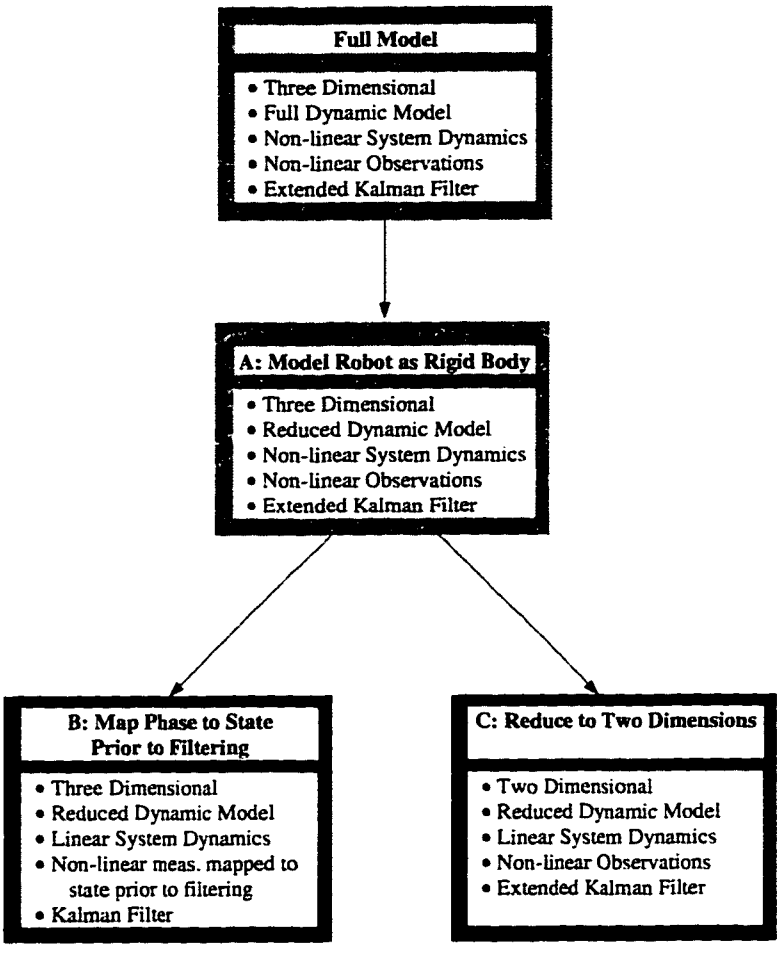

Figure 3.2: **Model Simplifications**

This progression of dynamic model simplification shows the characteristics of the two configurations that were implemented on the experimental system. Only models B and C were computationally feasible.

Performing non-linear mapping prior to filtering

By *statically* performing the non-linear mapping prior to filtering, it is possible to use a linear (rather than an extended) Kalman filter to derive the state estimate (model B). Although not as effective in suppressing measurement noise, this simplification enables computation of the state in three dimensions without excessive processing requirements.

Reduction to Two Dimensions

A disjoint simplification from the previous method is the reduction of the system state to two-dimensions (model C), keeping only the degrees of freedom that the robot can actuate. With this reduction, the extended Kalman filter is still used, albeit for fewer dimensions. The obvious drawback of this simplification is the loss of generality to three-dimensions, which was a requirement that motivated the use of GPS for sensing in the first place. Still, this is a useful configuration to pursue as a measure of the potential performance of the full model and the model A reduction.

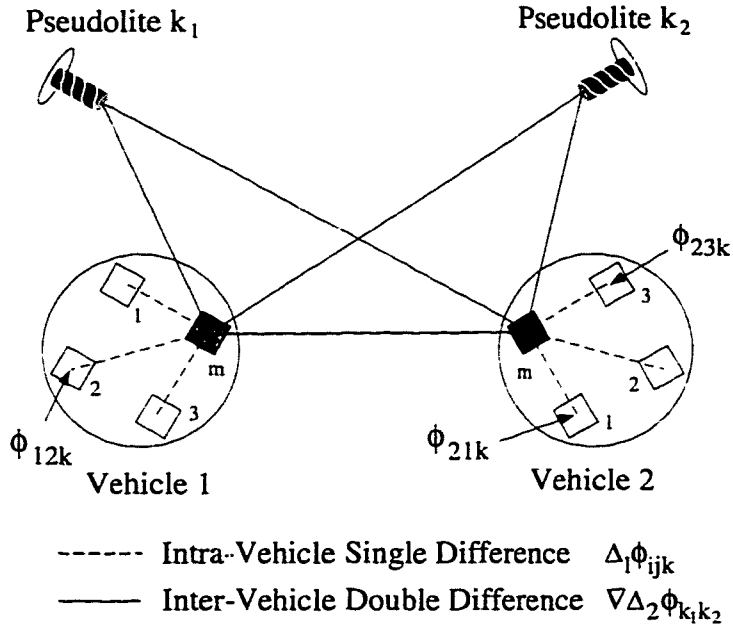

Figure 3.3: **Phase Difference Method**

3.2.2 Non-linear Observation Equations

Regardless of the model reduction employed, the derivation of the equations for mapping the phase measurements to the state variables is the same. The derivation of the relationship between the phase measurements and the state variables is provided below. Figure 3.3 shows the method by which the phases are differenced, and Figure 3.4 shows the definitions of the variables. The intra-vehicle phase differences, represented by dotted lines

in Figure 3.3, are single-difference measurements, while the inter-vehicle phase differences, represented by solid lines in Figure 3.3 are double-difference measurements. The reason for the single- and double-difference calculations is to cancel out the dominant time-bias terms in the measurements. The following assumptions and conventions are made in the derivation:

Assumptions and Conventions

- The initial position of each vehicle is known. This means that as long as the receivers maintain lock on the pseudolite signals, the integer cycles can be assumed known.
- The phase measurements are sampled at the exact same time on each receiver. In practice this is not true, and a method for compensating for the discrepancy is described in Section 3.3.1.
- Pseudo-range is unavailable. The pseudolites are not synchronized and cannot be used tc perform pseudo-range measurements.
- The positions of the pseudolite transmitters are known and fixed.
- There is one fixed *master pseudolite* in the constellation, and the receivers synchronize to its clock.
- Each vehicle has one fixed *master antenna.*
- Subscript i is always a *vehicle* index, j is an *antenna* index, and k is a *pseudolite* index; Subscript $j = m$ refers to the *master antenna* of a vehicle and $k = m$ refers to the *master pseudolite.*
- Δ_1 refers to an intra-vehicle difference measurement between the master antenna and a slave antenna of the *same* vehicle, while Δ_2 refers to an inter-vehicle single-difference *between the master antennas of two different vehicles.*

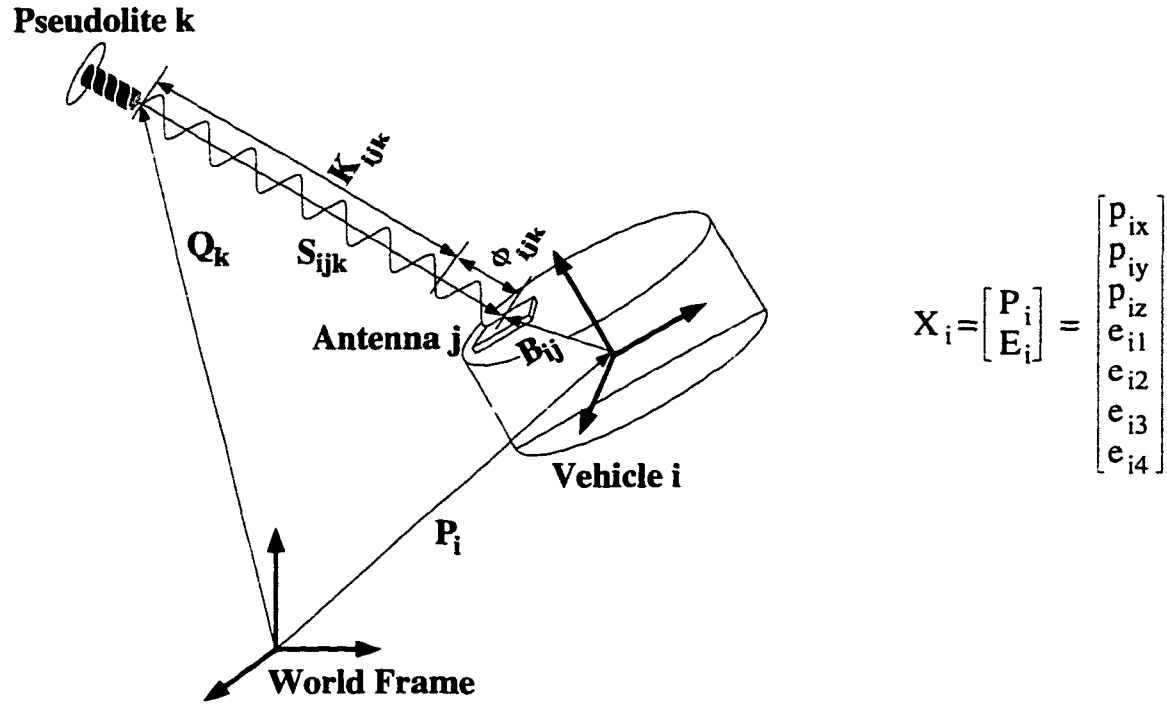

Figure 3.4: **Variable Definitions**

This diagram shows the relationships between the measurements, the known parameters, and the unknown state. The orientation of the vehicle, which is not explicitly shown in the diagram, is represented as a quaternion in the state vector.

P_i Position of vehicle i, in world frame

R_i Attitude of vehicle i, in world frame (as rotation matrix)

B_{ij} Baseline from vehicle center to antenna position, in vehicle frame

Q_k Position of pseudolite k, in world frame

S_{ijk} Line of sight vector from antenna (i, j) to pseudolite k

c Speed of light

τ_{vi} Receiver clock drift for vehicle i

τ_{pk} Transmitter clock drift for pseudolite k

λ GPS L1 carrier wavelength

K_{ijk} Integer ambiguity between antenna (i, j) and pseudolite k

The Unknown State

The unknown state of each vehicle is the 7x1 vector $X_i = (p_{ix}, p_{iy}, p_{iz}, \epsilon_{i1}, \epsilon_{i2}, \epsilon_{i3}, \epsilon_{i4})$. Figure 3.4 shows the relationships between the measurements, the known parameters, and the unknown state. The orientation of the vehicle (in the world frame) is alternatively represented in the equations as a direction cosines matrix R_i, which can be related to the quaternion representation (see [13]). The fourth quaternion ϵ_{i4} is constrained by the equation:

$$h_c(X_i) = \epsilon_{i1}^2 + \epsilon_{i2}^2 + \epsilon_{i3}^2 + \epsilon_{i4}^2 - 1 = 0 \tag{3.1}$$

Measurement Equations

The measured carrier phase at antenna j of vehicle i from pseudolite k is:

$$\phi_{ijk} = |S_{ijk}| + c\tau_{vi} + c\tau_{pk} + \lambda K_{ijk}$$

where the vector S_{ijk} is simply related to the position and orientation of the vehicle and the position of the pseudolite by:

$$S_{ijk} = (P_i + R_i B_{ij}) - Q_k$$

This results in the measurement equation:

$$\phi_{ijk} = |(P_i + R_i B_{ij}) - Q_k| + c\tau_{vi} + c\tau_{pk} + \lambda K_{ijk} \tag{3.2}$$

By relating the measurement equation (3.2) to Figure 3.4, the relevance of each member of this equation should be apparent. The terms $c\tau_{vi}$ and $c\tau_{pi}$ represent the portion of the phase incurred by clock differences between the transmitter and the receiver, and are the dominating terms in the measurement equations. It is necessary to eliminate these terms through differencing of multiple measurements.

Intra-Vehicle Single Differences (for each vehicle):

The intra-vehicle single differences contribute primarily to determination of the attitude of each vehicle. These equations are derived by taking the differences between the master

antenna ($j = m$) and each of the slave antennas j of vehicle i for measurement from pseudolite k:

$$\Delta_1\phi_{ijk} = |(P_i + R_iB_{im}) - Q_k| - |(P_i + R_iB_{ij}) - Q_k| + \lambda M_{ijk} \tag{3.3}$$

where the intra-vehicle integers $M_{ijk} = K_{imk} - K_{ijk}$, and j in $\Delta_1\phi_{ijk}$ reflects the slave antenna index.

Inter-Vehicle Double Differences (between vehicles):

The inter-vehicle double differences contribute primarily to the determination of the relative positions between each vehicle. Starting with single differences between master antennas of each vehicle:

$$\begin{aligned} \Delta_2\phi_k &= \phi_{1mk} - \phi_{2kk} \\ &= |(P_1 + R_1B_{1m}) - Q_k| - |(P_2 + R_2B_{2m}) - Q_k| + \\ &\quad c(\tau_{v1} - \tau_{v2}) + \lambda(K_{1mk} - K_{2mk}) \end{aligned} \tag{3.4}$$

Given N pseudolites, there are $N - 1$ unique double differences between pseudolite k_1 and k_2 ($k_1 \neq k_2$). These differences are calculated in order to eliminate the remaining effects due to clock differences $c(\tau_{v1} - \tau_{v2})$

$$\begin{aligned} \nabla\Delta_2\phi_{k_1k_2} &= \Delta_2\phi_{k_1} - \Delta_2\phi_{k_2} \\ &= |(P_1 + R_1B_{1m}) - Q_{k_1}| - |(P_2 + R_2B_{2m}) - Q_{k_1}| - \\ &\quad |(P_1 + R_1B_{1m}) - Q_{k_2}| + |(P_2 + R_2B_{2m}) - Q_{k_2}| + \lambda N_{k_1k_2} \end{aligned} \tag{3.5}$$

where the inter-vehicle integers are $N_{k_1k_2} = (K_{1mk_1} - K_{1mk_2}) - (K_{2mk_1} + K_{2mk_2})$.

Combining the Measurements

All of the measurements are coupled to the states of both vehicles, so all of the measurements must be combined to resolve these states. From equations (3.3), (3.6), and constraints (3.1)

the complete set of measurements can be related to the vehicle states:

$$\begin{bmatrix} \Delta_1\phi_{1jk} \\ 0 \\ \Delta_1\phi_{2jk} \\ 0 \\ \nabla\Delta_2\phi_{k_1k_2} \end{bmatrix} = \begin{bmatrix} h_1(X_1) \\ h_c(X_1) \\ h_2(X_2) \\ h_c(X_2) \\ h_{12}(X_1, X_2) \end{bmatrix} \tag{3.6}$$

where h_1 is a set of nonlinear functions of X_1, h_2 is a set of nonlinear functions of X_2, and h_{12} is a set of nonlinear functions of both X_1 and X_2. $h_c(X_i)$ is the quaternion constraint function (3.1). Given the phase measurements, the optimal estimate of X_1 and X_2 can be solved *statically* using a recursive least squares algorithm, or *dynamically* using an extended Kalman filter [18][1].

The maximum dimensions of the system are illustrated by the case in which all of the pseudolites are in view by all antennas of both vehicles. In this situation the dimensions of h_1 and h_2 are 18×1, and the dimension of h_{12} is 5×1. Adding the two constraints, there are a total of 43 measurements. This is far more than necessary (43 - 14 = 29 extra) to resolve the 14 state variables. The fewest number of pseudolites that can be in view and yet still resolve the states is three, so long as all three are in common between both vehicles, albeit such instances typically exhibit very poor observability in multiple dimensions. Since time is synchronized by a single master pseudolite, a fourth pseudolite is not needed to solve for time.

3.2.3 Measurement Weighting Matrix

The Signal-to-Noise Ratio (SNR) provides a measure of how well each signal is tracked and was therefore incorporated into the control signal processing for improved performance. Low SNR values are likely to occur when the pseudolite is far away or at a low angle with respect to the receiver antenna, or during occlusion of an antenna. The SNR can be related to the stochastic noise level of the carrier phase measurement through an empirically determined mapping. Incorporating this knowledge into the state-to-phase estimation algorithm can significantly improve the results. In the extended Kalman filter, the SNR values are

[1]The term "optimal" connotates some optimality criterion, which for a linear system is (generally) the minimization of the mean square estimation error. Since this is a nonlinear system, the term is used in the sense of the optimal estimate for the system linearized about the current operating point (see Gelb [18], pg. 105)

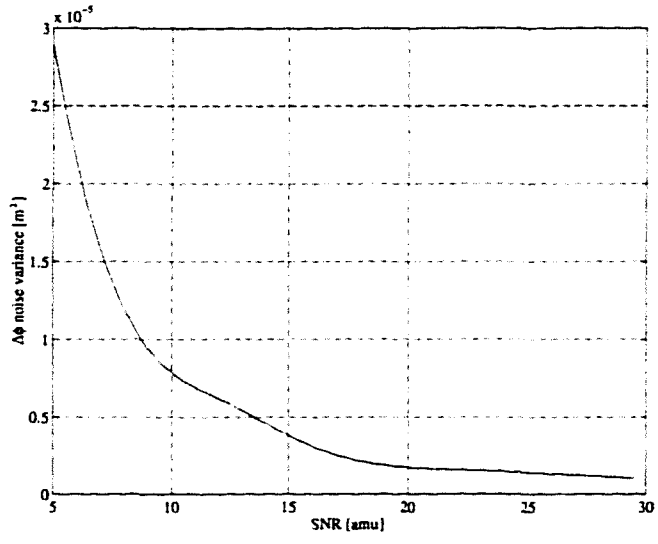

Figure 3.5: **Variance vs. Signal to Noise Ratio**
The SNR reported by the receiver used this mapping table to determine the corresponding variance of the signal (in square meters). The SNR values are reported in "amplitude measurement units" - a loosely defined unit that is approximately linear with the power of the signal and which is based on how well the received signal correlated with the internally generated signal.

used to derive the measurement weighting matrix, W, for the Kalman filter. Assuming that the carrier phase signals are uncorrelated Gaussian random variables, W is a diagonal matrix, with the diagonal elements equal to the variances of the corresponding differential carrier phase measurements. Since each of the differential carrier phase measurements is derived from either two (single difference) or four (double difference) independent signals, the variance elements of W must be derived from the variances of the independent carrier phase measurements. Due to communication bandwidth limitations between the GPS receiver and the control computer, the SNR value for each antenna/pseudolite pair is sent every sixth sample (1.67 Hz).

Since the differential phase measurements used to compute the state are derived from two individual phases (in the case of single differences) or four individual phases (in the case of double differences), it is necessary to compute the derived variances of each of these signals. By modeling the measured phases as independent Gaussian Random Processes, the variances for the differential carrier phases can be derived from the variances of the carrier phases merely by adding the carrier phase variances. For example, given the single

differential phase $\Delta_1\phi = \phi_1 - \phi_2$, the variance is $\sigma^2_{\Delta_1\phi} = \sigma^2_{\phi_1} + \sigma^2_{\phi_2}$. For the double difference phase $\nabla\Delta_1\phi = (\phi_1 - \phi_2) - (\phi_3 - \phi_4)$, the variance is $\sigma^2_{\nabla\Delta_2\phi} = \sigma^2_{\phi_1} + \sigma^2_{\phi_2} + \sigma^2_{\phi_3} + \sigma^2_{\phi_4}$. Note that by doing this, any carrier phase measurement with a low SNR (i.e. high variance) will reduce the weighting of *all* differential carrier phases derived from it.

The form for W is then:

$$W = diag(\sigma^2_{\Delta_1\phi_{1jk}}, w_c, \sigma^2_{\Delta\phi_{2jk}}, w_c, \sigma^2_{\nabla\Delta_2\phi k_1 k_2}) \tag{3.7}$$

Where $\sigma^2_{\Delta_1\phi_{1jk}}$ is the vector of single-difference phase variances for vehicle 1, $\sigma^2_{\Delta_1\phi_{2jk}}$ is the vector of single-difference phase variances for vehicle 2, and $\sigma^2_{\nabla\Delta_2\phi k_1 k_2}$ is the vector of double-difference phase variances. The weighting values for the constraint equations $w_c = 1$.

The SNR values reported by the GPS receivers were related to the stochastic noise level of the carrier phase measurement through an empirically derived mapping table. The data for the mapping table was obtained through an experiment in which a GPS pseudolite was directly connected to the master antenna input of a receiver. The pseudolite's signal strength was adjusted incrementally over the full dynamic range of the receiver while phase data was collected. The variances of the measured signals were calculated, and a spline fit was matched to the data so that it could be used as a lookup table (Figure 3.5), mapping SNR values to signal variances.

3.3 The Phase Difference Component

The primary function of the *Phase Difference* component, as noted in the *Control Structure* overview, is to compute phase differences and time-bias corrections from the time-tagged carrier phase measurements and code phases. Section 3.2 examined the differencing of phase measurements that were sampled simultaneously. In practice, the phases are not sampled at the exact same time; but by rationally assuming the phase-rate constant over the sample period they can be linearly extrapolated through time to improve the measurement. This section explains the phase extrapolation technique and also discusses methods for differencing phases when each vehicle is tracking different configurations (or sets) of pseudolite signals.

3.3.1 Time Bias Corrections

The equations derived thus far assume that the phase measurements $\phi_{ijk}(t)$ are sampled at the same instant on both vehicles. The receivers are synchronized only to within one millisecond of each other by the data message that is broadcast by the master pseudolite [51][2]. The phase differencing operations remove the first-order time differences. The small variation in sample times, or time bias, introduces a second-order effect which only impacts the inter-vehicle double differences. The intra-vehicle differential phases are sampled simultaneously, and therefore do not exhibit this effect. The error can be as large as the maximum observed carrier phase rate (up to 1 kHz, due to transmitter and receiver clock stability) times the receiver time bias (maximum 1 ms) times the wavelength (0.19 m); thus the error can be several centimeters. It is therefore necessary to remove this effect by estimating the measurement at time t, given only measurements at times t_i.

The measurement equation (3.2) must be modified to account for the difference in sample times between vehicles. The phase measurement at the supposed sample time t can be written in terms of the phase measurement made by vehicle i at time t_i as:

$$\phi_{ijk}(t) = \phi_{ijk}(t_i) + \int_{t_i}^{t} \dot{\phi}_{ijk}(t)dt \tag{3.8}$$

The term $\int_{t_i}^{t} \dot{\phi}_{ijk}(t)dt$ models the additional phase introduced by the time bias $t - t_k$. Re-evaluating the double-difference equation (3.6) with the time bias term included, the new form for $\nabla\Delta_2\phi_{k_1k_2}(t)$ in terms of the original form $\nabla\Delta_2\phi_{k_1k_2}(t_1, t_2)$ is:

$$\begin{aligned} \nabla\Delta_2\phi_{k_1k_2}(t) = {} & \nabla\Delta_2\phi_{k_1k_2}(t_1, t_2) \\ & + \int_{t_1}^{t} (\dot{\phi}_{1mk_1}(t) - \dot{\phi}_{1mk_2}(t))dt \\ & - \int_{t_2}^{t} (\dot{\phi}_{2mk_1}(t) - \dot{\phi}_{2mk_2}(t))dt \end{aligned} \tag{3.9}$$

[2]The phase measurements are sampled on the receiver's internal clock interrupt, which can be up to a half of a millisecond ahead of or behind the epoch interrupt from the master pseudolite (deemed "true time"). This means that phase measurements can be sampled up to a millisecond apart.

It is desirable to find a means for estimating the additional phase due to time bias, $\int_{t_i}^{t} \dot{\phi}_{ijk}(t)dt$, to improve the double-difference measurement. For conventional GPS measurements, the time bias is a natural by-product of the pseudo-range computation. Equivalent information for the present system can be obtained from the code phase of the master pseudolite. First, making the rational assumption that the phase rate $\dot{\phi}(t)$ is constant over the sample period (0.1 s), the time bias term can be approximated with a simple first-order expansion:

$$\int_{t_i}^{t} \dot{\phi}_{ijk}(t)dt \approx \frac{\phi_{ijk}(t_i) - \phi_{ijk}(t_i - t_i')}{t_i - t_i'}(t - t_i)$$

where t_i' is the time of the previous sample, as indicated by the receiver's clock. Considering the master pseudolite's clock to be "true time" and assuming negligible time-of-flight between the master pseudolite and each of the vehicles (an assumption implicitly made when pseudo-range accuracy was deemed inadequate for the scale of this experiment), then *the receiver's measurement of the master-pseudolite code phase, r_{imm}, is directly proportional to the time bias, $t - t_i$.* Incorporating this notion and multiplying by a proportionality constant C_r to convert the units of the code phase measurement to the units of time, the time bias correction becomes:

$$\int_{t_i}^{t} \dot{\phi}_{ijk}(t)dt \approx \frac{\phi_{ijk}(t_i) - \phi_{ijk}(t_i - t_i')}{t_i - t_i'} C_r r_{imm}(t_i) \tag{3.10}$$

This correction factor is applied to equation (3.10) to improve the accuracy of the inter-vehicle double-differenced phases.

3.3.2 Configuration Management

Another function of the *Phase Difference* component is to manage the combinations of phase signals that are differenced. If all pseudolites are in view by all antennas, then the arrangement of the phase differences is relatively straight-forward. When this is not the case, some criteria must be used to determine the selection of which of the valid signals are differenced. Each arrangement of phase differences is referred to as a "configuration", and so whenever a pseudolite signal is gained or lost, a "configuration change" takes place. The process of a configuration change involves re-calculation of the cycle ambiguities for each of

the phase differences affected by the particular signal loss or acquisition. This re-calculation of cycle ambiguities is referred to as an "integer cycle hand-off" since the knowledge from the sample prior to the loss or acquisition is used to compute the new unknowns.

For the intra-vehicle phase differences, it is assumed that if the master antenna of a vehicle is locked on to a pseudolite signal, then all of the slave antennas are also locked on to that signal. This assumption can clearly be invalid in a situation in which another vehicle occludes a pseudolite from a slave antenna but not the master. However, in such situations the low SNR of the occluded antenna will produce a very low (possibly zero) weighting factor for that measurement, rendering it ineffectual to all ensuing computations. Therefore, the set of intra-vehicle phase differences is always of dimension $N_{slave\_ant} \times N_{valid\_pseudolites}$.

The configurations or sets of signals used to compute the inter-vehicle phase differences were more complex to manage, since each inter-vehicle double-difference phase is derived from four independent carrier phase measurements. Figure 3.6 shows all of the raw carrier phase signals from which the phase differences can be derived. Any two pairs of signals from independent pseudolites can constitute a double difference phase measurement, and therefore some criteria must be used to determine which pairs are differenced.

For this project, a very simple rule was employed, and that was to always take differences between sequentially valid pseudolites. More sophisticated methods could be employed to achieve higher-quality results. For instance, one could take into account which signals have the best SNR values and double-difference those, so that no single weak signal would cause a low weighting factor to corrupt three good signals.

In matrix form the differencing scheme can be represented:

$$\nabla\Delta_2\Phi = \begin{bmatrix} 1 & -1 & 0 & 0 & 0 & 0 \\ 0 & 1 & -1 & 0 & 0 & 0 \\ 0 & 0 & 1 & -1 & 0 & 0 \\ 0 & 0 & 0 & 1 & -1 & 0 \\ 0 & 0 & 0 & 0 & 1 & -1 \end{bmatrix} \begin{bmatrix} I_6 & -I_6 \end{bmatrix} \begin{bmatrix} \Phi_{1k} \\ \Phi_{2k} \end{bmatrix} \tag{3.11}$$

where Φ_1 and Φ_2 are the 6×1 vectors of raw carrier measurements at the master antennas of each vehicle and I_6 is a 6×6 identity matrix. Whenever a satellite is lost by either vehicle, the corresponding row and column of ∇ is removed and the dimensions of the rest of the equation are reduced.

It should be noted that Lightsey [25] has studied roving master antennas, which would change much of this implementation and could improve the performance of these techniques.

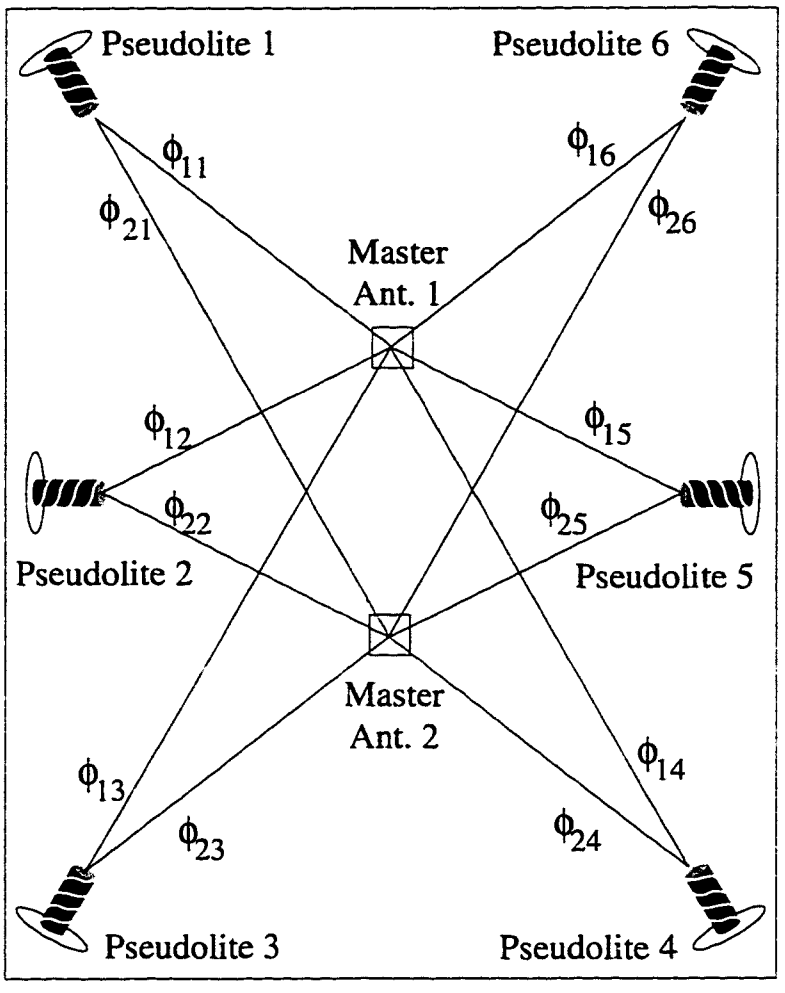

Figure 3.6: **Raw Carrier Phases Used to Compute Inter-Vehicle Double Differences**

This diagram is designed to show conceptually all of the possible raw carrier phase signals from which double-differenced phase measurements can be derived. The six pseudolites are displayed and labeled around the perimeter, and the master antennas of each of the two vehicles are shown in the interior workspace. Any two pairs of signals from independent pseudolites can constitute a double-differenced phase measurement, and therefore some criterion must be used to determine which pairs are differenced. Note that the antenna indices are dropped for simplicity, since all phases are with respect to the master antenna.

3.4 The Integer Manager Component

The *Integer Manager Component* converts the fractional phase measurements to range measurements by adding and maintaining the whole-integer cycles of the signal. In Figure 3.4 this means that the Integer Manager Component adds and maintains K_{ijk} to ϕ_{ijk} in order to establish $|S_{ijk}|$. The initial value for K_{ijk} is established by the *Integer Resolution Component*. The number of integer cycles should remain known once a signal has been locked; however a weak signal may experience cycle jumps in the measured phase, and so K_{ijk} must be incremented or decremented to account for this. Also, if there is a loss and then re-acquisition of a pseudolite, then the corresponding integers for that pseudolite need to be re-calculated.

The carrier-phase method requires that the signal remain in lock, or else a discontinuity in the measured position will occur. If the signal is lost, there needs to be a way to hand off integer cycle to the new configuration. If the system is well calibrated, and there are no bias errors, then a pseudolite signal configuration change will have no effect on the estimated measurement. In practice, this is not the case. Loss of a pseudolite signal introduces a discontinuity in the estimated position and attitude of the vehicle due to the fact that a different set of measurements is being used to compute the state. The challenge is to maintain this discontinuity such that its impact is less than an integer wavelength for all of the measurements involved in the solution. If it is greater than a wavelength, there is no way for the system to distinguish the loss of the pseudolite signal from a cycle slip[3].

Maintaining the discontinuity such that its impact is less than an integer wavelength is a difficult constraint, as it is the discontinuity in *absolute* position that must be maintained to less than an integer. Additionally, the constraint on the master pseudolite's signal is not a whole integer, but *one half an integer* for the double differenced phases, due to a half-cycle ambiguity caused by the 50 bit/sec data message.

3.4.1 Cycle Slip Management

The *Integer Manager Component* maintains the integers through a Nyquist comparison with the feed-forward estimates of the phase. It is assumed that the measured phase cannot be more than one-half of an integer cycle off from the predicted phase estimate $\hat{\phi}$. If it is, then the corresponding integer K_{ijk} is incremented or decremented accordingly by the number

[3]Cycle slip detection can be disabled for the single sample that the pseudolite signal is lost.

of integer cycles beyond the predicted phase. As noted in the previous section, for the case of the master pseudolite the 50 bit/sec data message imposes a half-cycle ambiguity on the carrier phase from that pseudolite. This means the measured phases from the master pseudolite cannot be off by more than one-quarter cycle (4.76 cm) from the predicted phase estimates in order to detect integer cycle slips.

Better performance of this technique could be achieved by feeding forward the accelerations directly into the GPS receiver's phase-lock-loop controllers; however, this would require much greater bandwidth communication to the receiver, and an open-architecture receiver (see Chapter 7 for greater discussion).

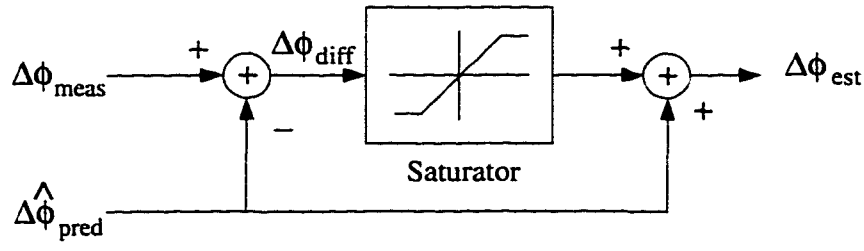

Figure 3.7: **Signal Diagram of Multipath Suppression Through Signal Bounding**

This diagram shows how the measured phase signal is tested and bound to a range about the predicted phase. If the measured phase is very close to the predicted phase, then nothing is done to the measured phase and it is used directly in the state estimation process. If the measured phase differs greatly from the predicted phase (presumably due to multipath), then the deviation is limited before use in the state estimation process. Choice of the bound limit of the saturater is critical to the effectiveness of this scheme. A very small value eliminates the measured signal and the system runs open loop. A very large value causes the scheme to have no effect. Subsequent experiments show a useful range of 0.47 cm (min) through 0.94 cm (max) for the saturator.

3.4.2 Multipath Suppression

Reflected signals occasionally interfere with the direct line-of-sight signal to corrupt the phase-to-state estimate. These reflected signals interfere with the direct line-of-sight signal in constructive and destructive manners and are therefore not necessarily weak signals that the SNR weighting will suppress. It is not uncommon for a multipath-corrupted signal to have a high SNR and therefore a high weighting value in the estimation process. A safeguard in addition to SNR weighting was inserted in the *Integer Manager Component* to suppress the effects of multipath. This safeguard works by *bounding the phase used in the*

estimation process to a fixed band around the predicted phase. This process does not affect measurements that differ only slightly from the predicted values, but will limit the effect of outliers.

A signal diagram is shown in Figure 3.7. From this diagram it can be seen that the choice of the bounding limit is critical to the effectiveness of this technique: A very small bound will eliminate multipath very effectively, but it will also eliminate the feedback signal. That is, as the bound limit decreases to zero, the system approaches open-loop. A very large bound will have no effect whatsoever toward limiting the multipath.

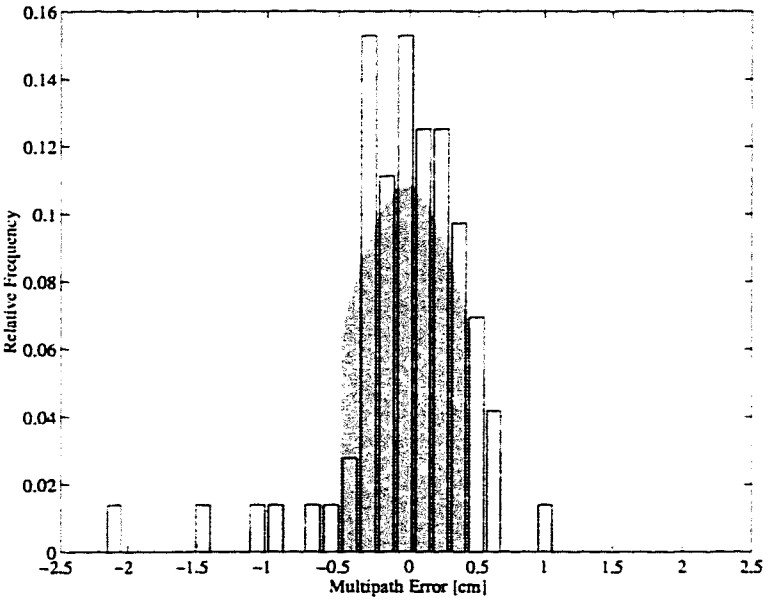

Figure 3.8: **Multipath Phase Error Likelihood**

This plot shows the relative likelihood of a multipath phase error of a given magnitude to occur. The standard deviation of these errors was found to be 0.47 cm. The 1-σ band of this probability mass function is delineated by the dark gray region.

The method for choosing the size of the phase bound limit and an analysis of the effectiveness of this technique follow. First, a statistical measure of the magnitude of the multipath was established. From this, the impact of multipath on the estimated position and orientation was determined. Finally, the impact of *bounded* multipath on the estimated position and orientation was established to demonstrate the effectiveness of the suppression scheme.

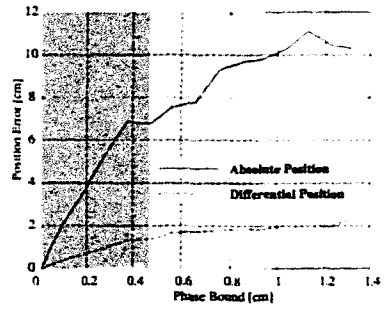

Figure 3.9: **Position Error Versus Multipath Error Bound**

The incurred position error can be reduced by bounding the measured phase about its predicted value. Conceptually, this can be thought of as "chopping" off the tails of the probability mass function shown in the previous diagram. As this bound becomes tighter, the position error due to multipath is reduced at the cost of eliminating increasing amounts of the feedback signal. The 1-σ band is shown in light gray, while the 2-σ band is shown in dark gray. The bound used in the experiments was set at 1-σ (0.47 cm). Bound values less than 1-σ eliminated too much of the feedback signal, while larger bounds were ineffectual against removing multipath effects.

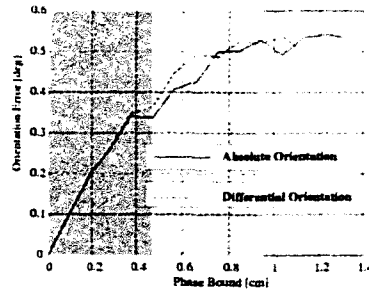

Figure 3.10: **Orientation Error Versus Multipath Error Bound**

This plot shows the correspondence between the multipath bounding value and the expected orientation error. As with the previous diagram, the 1-σ band is shown in light gray, while the 2-σ band is shown in dark gray. The bound used in the experiments was set at 1-σ (0.47 cm).

The experiment described in Section 4.3.4 was performed to generate a plot that exhibits the likelihood of a multipath error of a given magnitude to occur (Figure 3.8). This experiment showed the multipath to be approximately zero mean, with a standard deviation of 0.47 cm. Noise with these statistical characteristics was injected into the phase-to-state mapping algorithm in simulation to determine its effect on the estimated position and

orientation. These simulations were repeated for a range of bounds on the injected noise to determine the effectiveness of the phase-bounding scheme. The results are plotted in Figures 3.9 and 3.10. These two plots show the expected position and orientation errors for given bounds on the multipath error. As expected, tight bounds on the injected multipath result in decreased errors in the estimated position and orientation, while bounds greater than 2-σ (0.94 cm) have almost no noticeable effect. A bound of 1-σ (0.47 cm) results in about 20% decrease in the effect of multipath. It was found experimentally that bounds less than 0.47 cm removed too much of the feedback signal, resulting in a loss of control for typical slews (such as the ones shown in Sections 4.3.1 and 4.3.2).

3.5 Summary of GPS for Control

This chapter has presented a scheme for using GPS as a sensor for real-time control. The individual components of the system and their inter-connectedness is general and could potentially be applied to other applications, while the content of some of the components are particular to the problem at hand. For instance, the *GPS Receiver Component*, *Phase Difference Component*, and *Integer Manager Component* could be applied to a wide range of systems, while the algorithms of the *Phase-to-State Mapping Component* and *Integer Resolution Component* are specific to the current system. These components form basis from which new systems can be designed.

Chapter 4

Experimental Demonstrations

Several experiments were conducted to demonstrate the performance of the integrated GPS-controlled robot system. These experiments were designed to exhibit key qualities of the GPS sensor, including accuracy, bandwidth, noise and reliability. Results are presented from the highest level with discussions of the autonomous-rendezvous and formation-flying demonstrations and then in more detail with results of bandwidth and noise analyses.

4.1 Autonomous Rendezvous

The motivation for performing the autonomous-rendezvous and formation-flying experiments was to:

- Demonstrate a sophisticated task, commanded at a high level and thoroughly executed by an autonomous vehicle guided by GPS.
- Establish guidelines for developing operational GPS-based systems, including typical system parameters and achievable tolerances.
- Introduce new approaches to sensing using GPS, and to present newly-discovered issues that may lead to improved capabilities of this type of sensor.

The autonomous-rendezvous experiment was a comprehensive demonstration of the aggregate system, including the GPS sensors, the robot and target vehicle, the corresponding control algorithms, and the user interface.

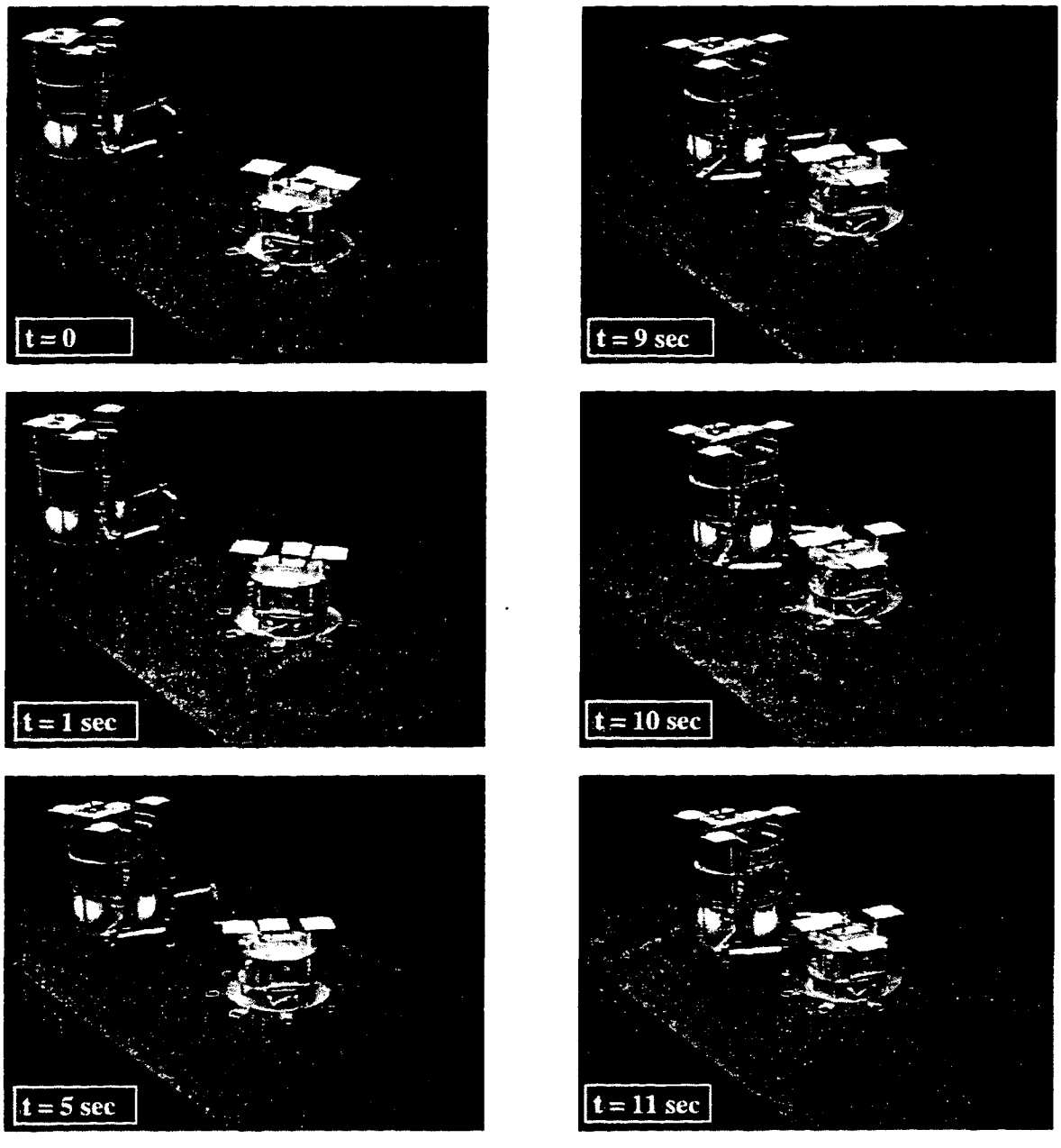

Figure 4.1: **Rendezvous Sequence Snapshot Images**

These video snapshots show the sequence of events in the rendezvous process: Initial State, $t = 0$ *sec;* Intercept Commanded By User, $t = 1$ *sec;* Traversing Intercept Trajectory, $t = 5$ *sec;* Target Within Grasp Range $t = 9$ *sec;* Tracking Target Ports $t = 10$ *sec;* Grasping Target $t = 11$ *sec.*

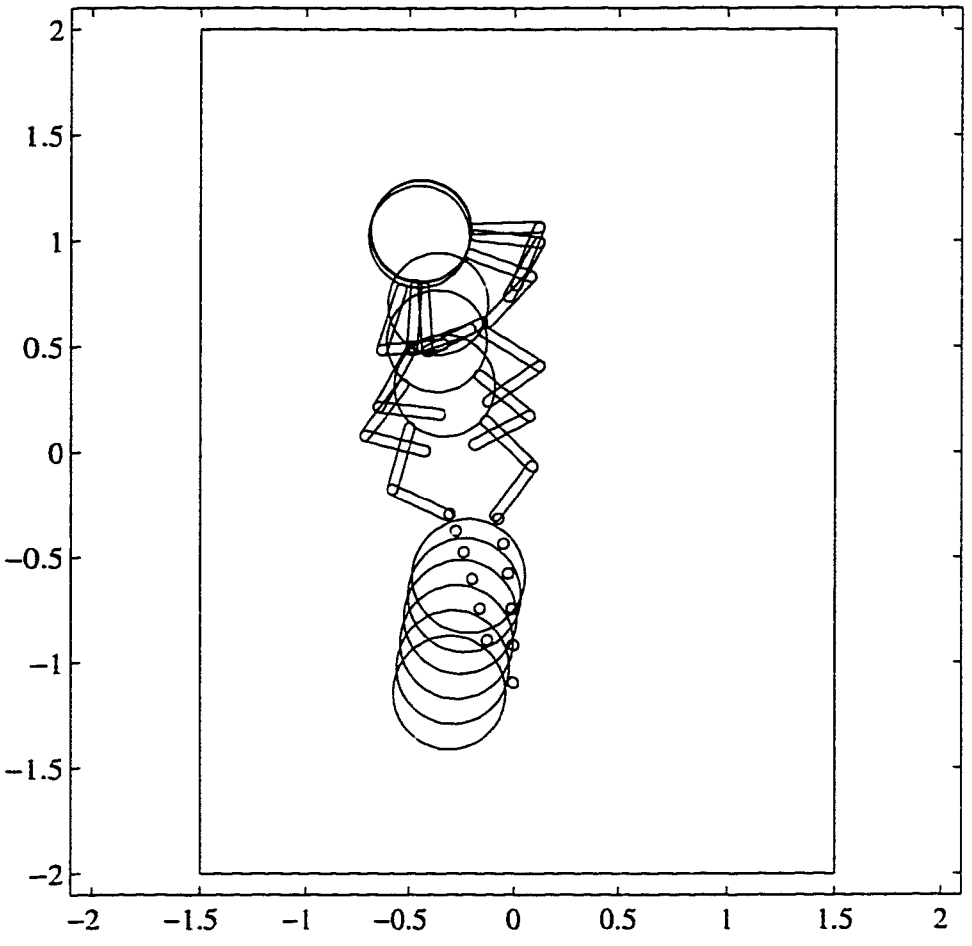

Figure 4.2: **Overhead Time-Lapse Sequence**

This figure provides a graphical representation of the experimental data from the rendezvous sequence shown in the previous figure. The images in this sequence were taken at 2 second intervals.

Snapshot images from a video of an autonomous-rendezvous are shown in Figure 4.1, and a time-lapse overhead view of the sequence is shown in Figure 4.2. Corresponding data plots of the relative positions of the vehicles are shown in Figure 4.5.

A summary of each step of the sequence is described herein, while more in-depth descriptions of particular segments are provided later. At the start of the sequence the target vehicle is tossed across the workspace with small translational and angular velocities while the robot is motionless (frame 1, $t = 0$). The robot is commanded by the user to intercept the target (frame 2, $t = 1sec$). In response to the user command, the robot generates

a differential-position trajectory to reach a fixed stand-off location relative to the target. The robot propels itself along the trajectory toward the target stand-off location (frame 3, $t = 5sec$). Once the target is within reach of the robot's manipulators, the arms are commanded to track the gripper ports on the target (frames 4 and 5, $t = 9sec$ to $t = 10sec$). Upon successful tracking, the grippers are closed on the target ports. (frame 6, $t = 11sec$). Once the target is grasped, it is manipulated into stowed position for transport until the user commands release.

The following descriptions provide more in-depth analyses of each step of the rendezvous process:

1. *Initial State:* All integer cycle ambiguities have been resolved prior to the initial state shown in the snapshot sequence. Integer resolution can be done through a motion-based algorithm as described in Chapter 5 and [21]. Under this scenario the cycle ambiguities are resolved by collecting phase-measurement data as the vehicles are manually moved around the table. The vehicles are then grounded while a batch process resolves the ambiguities from all of the collected data. This can be done without preliminary survey of the arena. A simpler, but less autonomous method for initializing the cycle ambiguities is to place the vehicles in known locations in the workspace, and then fix the integers. A more convenient means for resolving the ambiguities was also accomplished through the use of the overhead vision system. Here the ambiguities were resolved by merely backing out the integers from the initial position reading from the vision system.

2. *Intercept Command:* The intercept command is issued by a human operator at the task level through a graphical user interface, as shown in Figure 4.3. Only a high-level *task command* needs to be issued across the communications link. The *Network Data Delivery Service* handles these communications, all of which require minimum bandwidth and are unaffected by data delays. The user merely selects the *Intercept* mode of operation, and then commands the robot to do so by selecting the *Activate* button. The progress of the intercept process is monitored on the world-model screen display and can be viewed in three dimensions from any angle. After the target has been captured, the robot can be commanded to release it by means of the *Release* button. The user can also select what information to view.

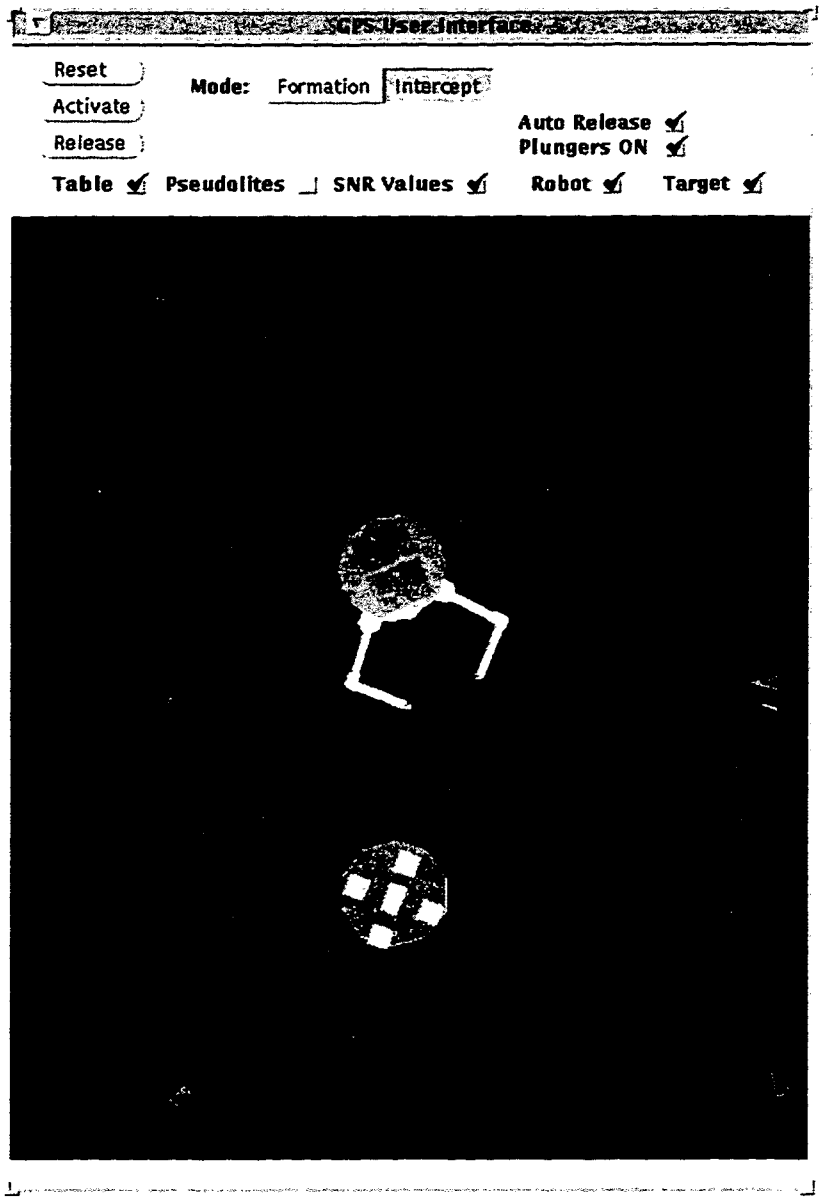

Figure 4.3: **Task-Level Command Graphical User Interface**

This screen snapshot shows the high-level interface through which the user commands the robot to perform tasks. The robot can be commanded either to intercept the target vehicle or to maintain a fixed station-keeping location with respect to the target to emulate formation-flying operations. The user can display whatever information is deemed relevant to a specific operation and can also change some system parameters. The cones around the perimeter of the workspace indicate the signal strength received by each of the vehicles from each pseudolite transmitter. For example, the right-most cone of the two cones in the lower left corner indicates that the target vehicle is receiving a much stronger signal from the pseudolite in that location, as expected since the target vehicle is closest to that peudolite.

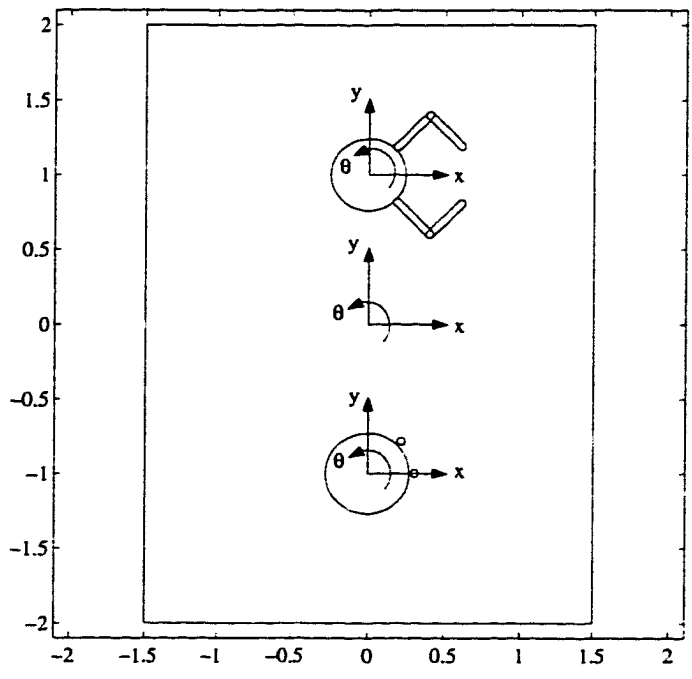

Figure 4.4: **Coordinate Frames of the Robot, Workspace, and Target Vehicle**

This diagram shows the coordinate definitions for each of the vehicles and the workspace. The scale indicates the world coordinate frame in dimensions of meters. The target vehicle is shown with two of its eight gripper ports.

The high-level task command is the means in which all robots in the Aerospace Robotics Lab are commanded. Others in ARL have studied more extensive task capabilities for the free-flying robots, including object transport and delivery [45], assembly of space structures using multiple robots [15] [35], and adaptation to unknown payloads [6]. The limited set of task commands demonstrated in this project were sufficient to show for the first time high-level capabilities enabled by the GPS sensor technology.

3. *Trajectory Traversal:* Upon issuance of the intercept command from the user, the robot generates an intercept trajectory based on the differential position and velocity of the two vehicles in order to reach a stand-off location relative to the target. The robot's trajectory is a bang-off-bang trajectory in the translational dimensions, based on the differential position between the vehicles in the world frame. The destination of the trajectory is a fixed differential distance from the target (0.75m). At this range,

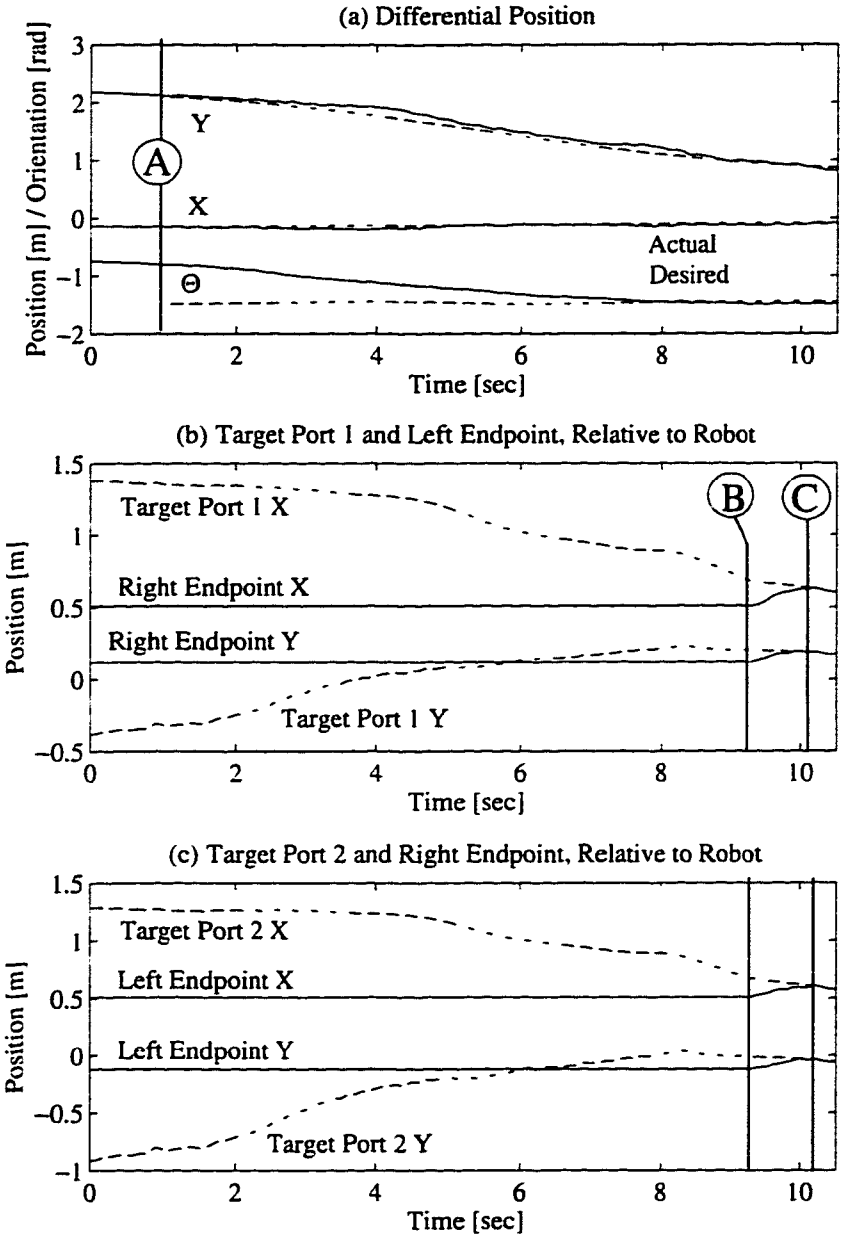

Figure 4.5: **Rendezvous Time-Lapse Sequence**

These plots show the vehicle and manipulator endpoint trajectories during the rendezvous sequence. Time (A) in the first plot indicates when the user issued the rendezvous command to the robot. Time (B) in the second and third plots indicates when the robot started reaching for the target, and time (C) indicates when the manipulators grasped the target.

the target gripper ports are well within reach of the robot's manipulators. Once this region is entered, the manipulators are commanded to reach for the nearest target ports. Figure 4.6 shows a typical bang-off-bang command trajectory. The maximum acceleration of the robot base determines the length of time required for the trajectory to be executed. Table 4.1 lists these acceleration limits. The robot's orientation is computed such that the robot always faces the target vehicle during the translational trajectory. This is done with a command orientation that is the angle subtended by the forward direction of the robot and the direction of the differential position vector, as shown in Figure 4.7.

4. *Reaching and Tracking Target Ports:* As the robot approaches the stand-off location from the target, the target enters within grasp range of the robot's manipulators. At this point a finite state machine is executed. The functional performance of this state machine is expressed by the pseudo-code below. The two states HOME_AND_TARGET_OUT_OF_RANGE and HOME_AND_TARGET_IN_RANGE provide hysteresis so that the robot does not attempt to grasp the target immediately after the user commands the target to be released.

```
IF state is HOME_AND_TARGET_OUT_OF_RANGE
   raise grippers
   move arms to home position
   IF target in range for > 0.2 sec
      select ports to grasp
      change state to REACHING
IF state is HOME_AND_TARGET_IN_RANGE
   raise grippers
   move arms to home position
   IF target not in range
      set state to HOME_AND_TARGET_OUT_OF_RANGE
IF state is REACHING
   IF target in range
      compute locations of selected ports
      move arms to selected port locations
```

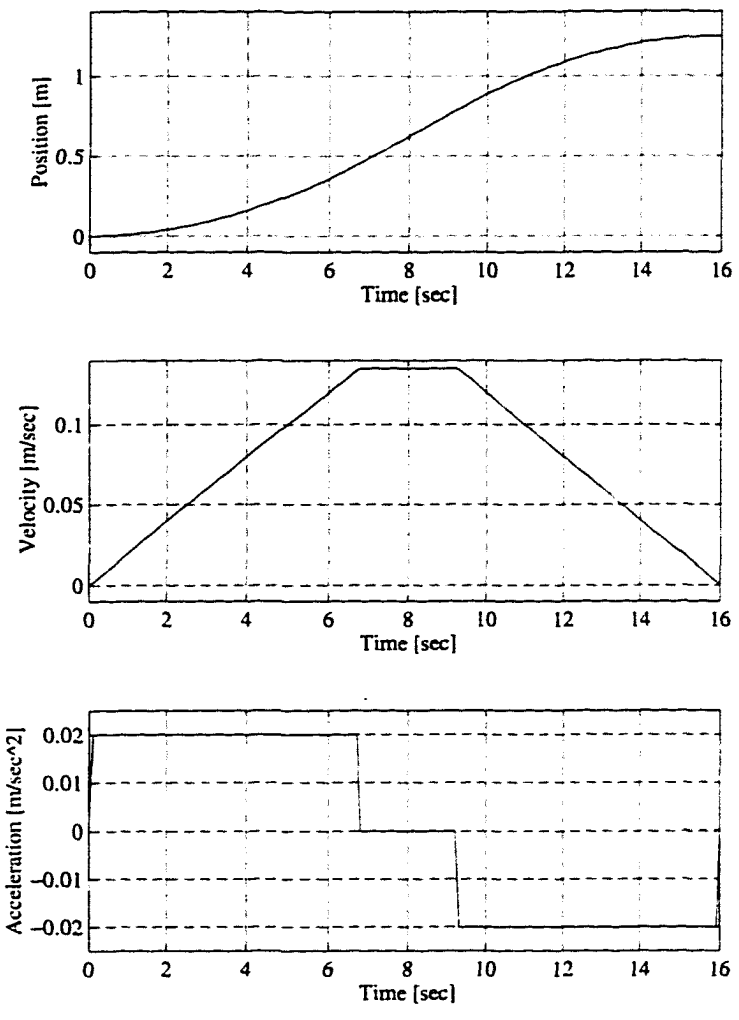

Figure 4.6: **Bang-Off-Bang Translational Trajectory**

These plots show a typical bang-off-bang trajectory commanded to the differential position during rendezvous. The maximum acceleration limits on the robot base determine the length of time over which the trajectory is executed.

```
      IF arms are at selected ports
         set state to GRASPING
   ELSE
      set state to HOME_AND_TARGET_OUT_OF_RANGE
IF state is GRASPING
   IF arms are at selected ports
```

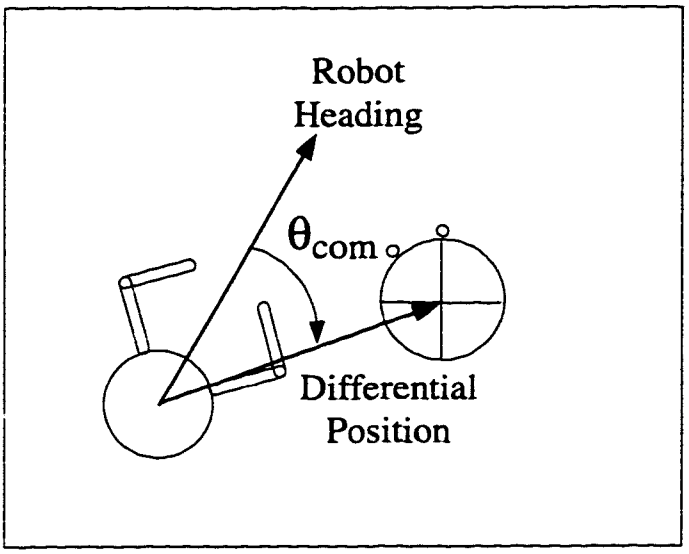

Figure 4.7: **Desired Orientation Command**

The commanded orientation is the angle subtended by the forward direction of the robot and the direction of the differential position vector. Using this simple method, the robot always faces the target vehicle during the translational trajectory.

```
      lower grippers
      set state to HOLDING
   ELSE
      set state to HOME_AND_TARGET_OUT_OF_RANGE
IF state is HOLDING
   IF user command to release
      set state to HOME_AND_TARGET_IN_RANGE;
```

The positions of the manipulator endpoints relative to the target ports are sensed through GPS measurements of the vehicle positions and encoder-based measurements of the manipulator joint angles. The desired endpoint commands are achieved through inverse kinematics for the two-link SCARA configuration manipulators. The kinematic equations for the relative positions of the endpoints to the target, as well as the

inverse kinematic equations can be derived from those provided for SCARA configuration manipulators in Craig [13].

5. *Grasping:* In the final step of the rendezvous process the robot pneumatically lowers its grippers into the target's gripper ports. The robot successfully grasped the target's 5 cm diameter gripper ports over 60% of the time in 50 attempts in which all six pseudolites remained in lock for the entire rendezvous. The misses are attributed to the cumulative bias errors in the system, including multipath, antenna phase center variation, signal polarization effects, and calibration error. These are the most critical limitations of the overall system, and as such they are analyzed in detail in Section 4.3.4 and suggestions for reducing these error sources are provided. The estimated cumulative effect of the bias errors is summarized in Table 4.4. Figure 4.8 shows a histogram of the error between the robot's manipulator endpoints and the center of the target's gripper ports, as detected by the overhead vision system. The success rate was lower (30%) whenever a pseudolite signal was lost during the rendezvous process, an effect of position errors introduced by phase biases during integer cycle hand-off.

4.2 Autonomous Formation Flying

Precise regulation of a vehicle's position and attitude with respect to another vehicle enables multiple vehicles to fly in a controlled formation or cluster. This capability makes it possible to perform precision spatially-distributed science missions without the need for interconnected spacecraft. Autonomous spacecraft formations are likely to require positioning tolerances on the order of a few centimeters in location and a few tenths of a degree in attitude in order to then align higher-precision laser metrology instruments. The experiment performed here demonstrates how GPS may be used as an alignment system for a formation of spacecraft in low earth orbit, with positioning accuracies in the range of a few centimeters and attitude of a few degrees. Chapter 7 and [3] provide further discussions of how GPS may be used for a formation of spacecraft in deep space.

In the autonomous formation-flying experiment the robot was commanded to hold station at a fixed distance from the target and to follow the orientation of the target. The target vehicle was then manually perturbed in position and orientation, and the robot maintained

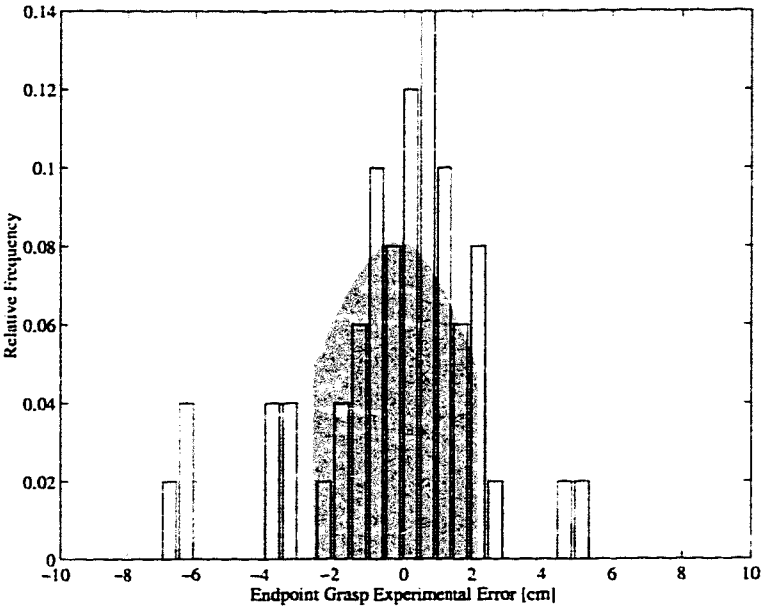

Figure 4.8: **Grasping Error**

a fixed relative station. Figure 4.9 shows video snapshots from the demonstration. After initialization, the target was rotated 90 deg counter-clockwise with a maximum angular acceleration of 0.1 rad/sec^2, which the robot tracked with a maximum angular error of 8 deg during the transient and 3 deg in steady-state. The target was then linearly translated with a maximum acceleration of 0.25m/sec^2, which the robot tracked with a maximum positional error of 12 cm during the transient and 1.5 cm in steady-state. These values were derived from the data in Figure 4.10 and 4.11. Finally, the target vehicle was freely tossed across the air-bearing surface while the robot maintained station. This provided a measure of the steady-state limit-cycle errors due to discrete thruster actuators, as shown in Figure 4.12. The target's linear velocity was 3 cm/sec and its angular velocity was 7 deg/sec. The maximum differential position error was 3 cm, while the maximum differential orientation error was 6 deg. A summary of acceleration disturbances from this demonstration is listed in Table 4.1.

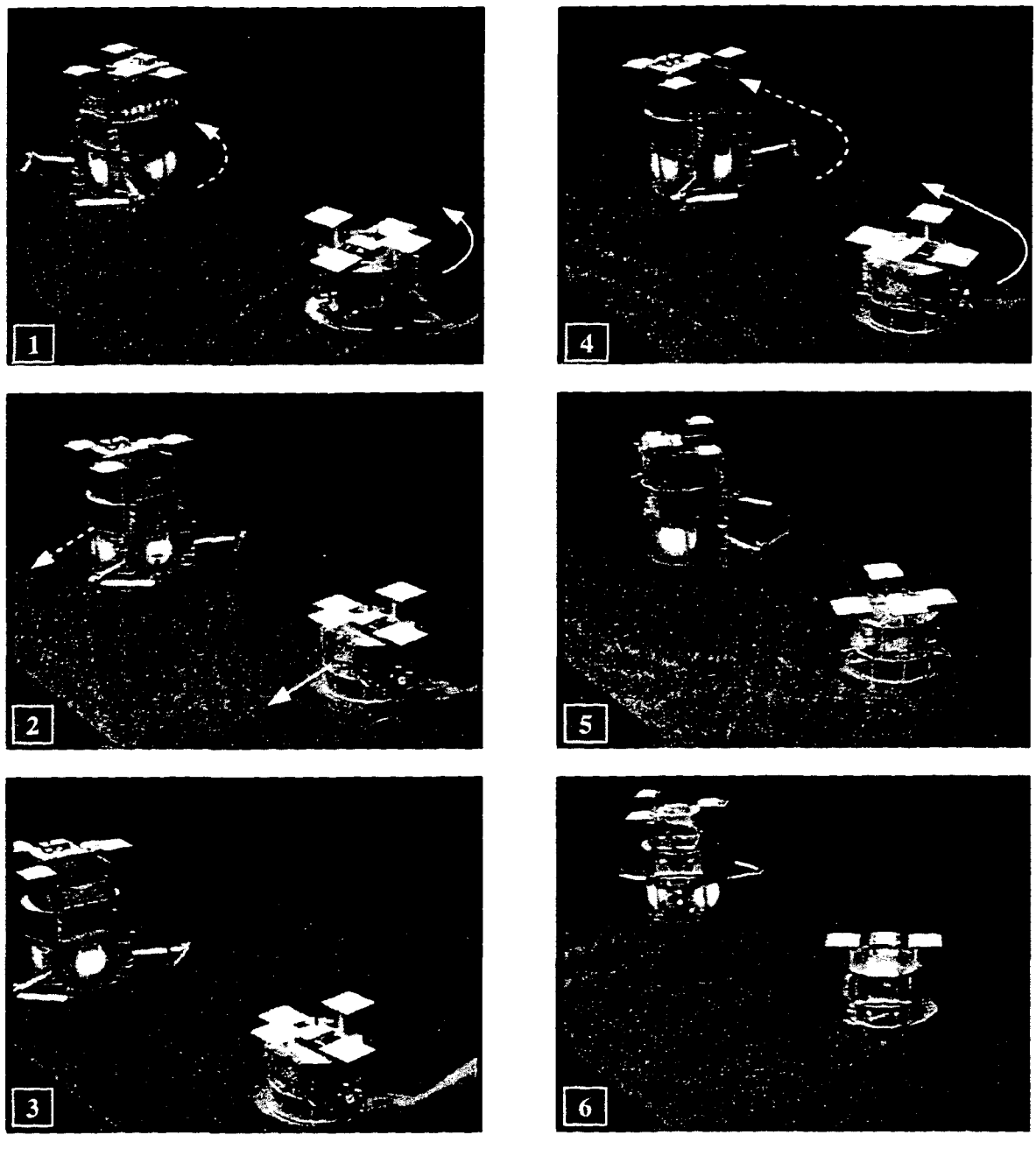

Figure 4.9: **Formation Flying Sequence Snapshot Images**

These video snapshots show the sequence of events in the formation-flying demonstration: Initial State (1), Rotational Response (1,2), Translational Response (2,3), Combined Rotation and Translation (4,5,6).

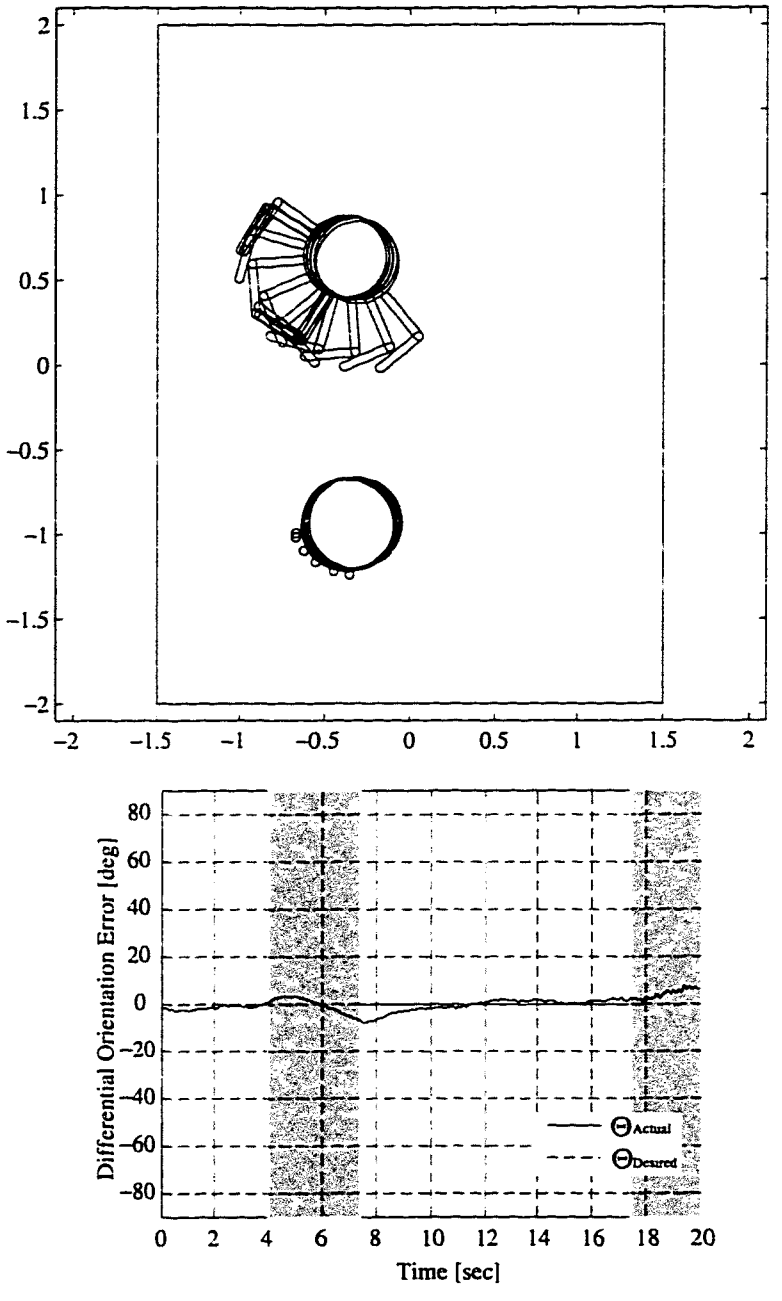

Figure 4.10: **Formation Time Lapse: Rotational Response**

This graph shows the differential orientation error between the robot and the target as the target was manually rotated 90 deg counter-clockwise. The gray band indicates the time during which the target was angularly accelerated and decelerated by hand.

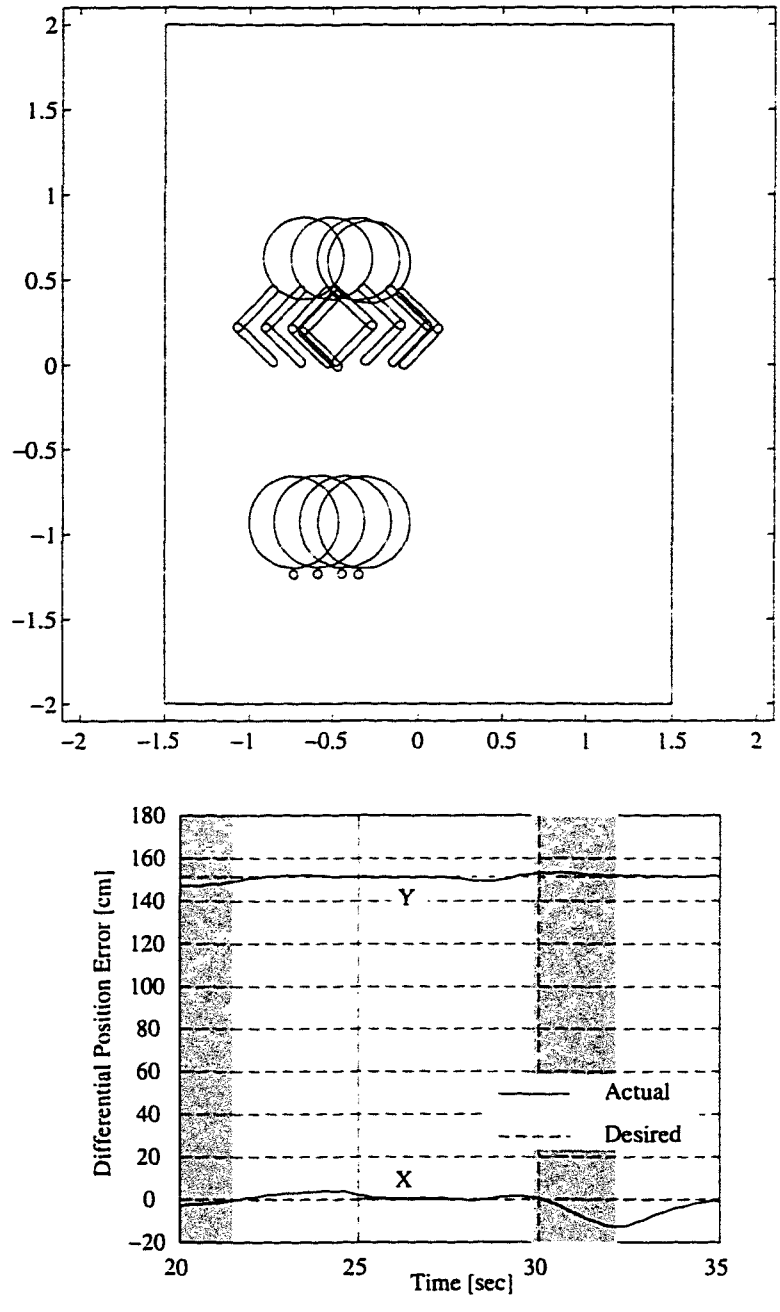

Figure 4.11: **Formation Time Lapse: Translational Response**

This graph shows the differential position error between the robot and the target as the target was manually translated 50 cm in the negative-x direction. The gray band indicates the time during which the target was accelerated and decelerated by hand.

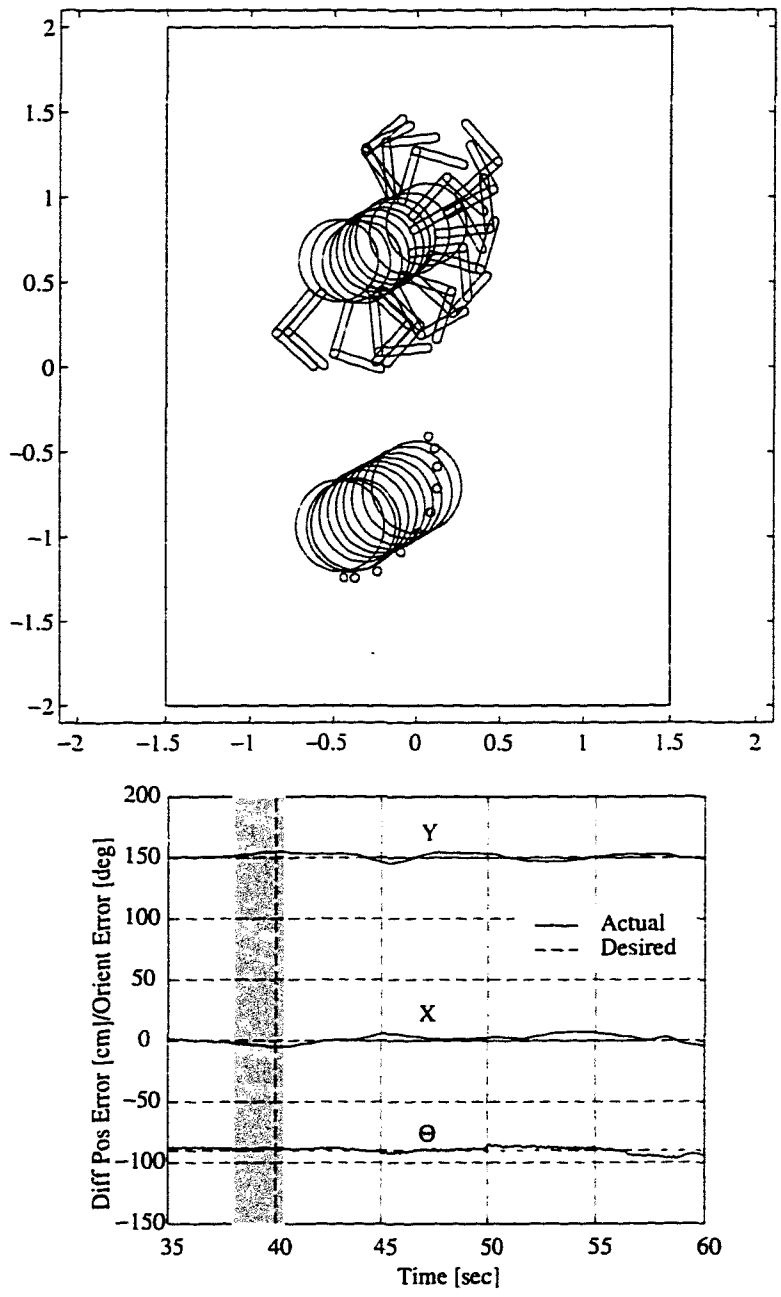

Figure 4.12: **Formation Time Lapse: Rotational and Translational Response**

This graph shows the differential position and orientation errors between the robot and the target as the target was tossed across the air-bearing surface. The gray band indicates the time during which the target was linearly and angularly accelerated. Steady-state limit cycling is particularly apparent in the differential orientation after 50 sec.

Parameter	Vehicle Accel Limit (dynamic)	Sensor Accel Limit (experimental)
Linear Accel Disturbance	0.002 m/sec^2	0.25 m/sec^2
Angular Accel Disturbance	0.04 rad/sec^2	0.1 rad/sec^2

Table 4.1: Acceleration Limits

4.3 System Performance

4.3.1 Step Response

In addition to the formation-flying experiment, step response experiments were performed to gain a more quantitative indication of the robot's ability to track the target. For these experiments the target vehicle remained stationary, while the commanded relative location and orientation inputs to the robot controller were changed manually. The collected data also included measurements from the overhead vision system for comparison with the GPS measurements. Figure 4.13 shows the position response to a 20 cm step in the commanded position. The graph evidences a time of 15 sec to complete the translational slew, and a maximum deviation of 2.5 cm from the position observed by the overhead vision system. Figure 4.14 shows the orientation response to a 45 deg step in the commanded orientation. This graph shows a time of 15 sec to complete the translational slew, and a maximum deviation of 3 deg from the orientation observed by the overhead vision system.

4.3.2 Bandwidth

The end-to-end bandwidth of the experimental apparatus is limited by the dynamics of the robot vehicle, and so to know the dynamics of the GPS sensor subsystem per se, it is desirable to measure the bandwidth of that subsystem independent of the dynamics of the vehicle. An experiment was therefore devised to establish the bandwidth of just the GPS receiver with the subsequent signal processing code. The test was performed by simulating the motions of the robot in software, thereby generating simulated GPS signals corresponding to these motions, and then feeding these into the original signal processing algorithms.

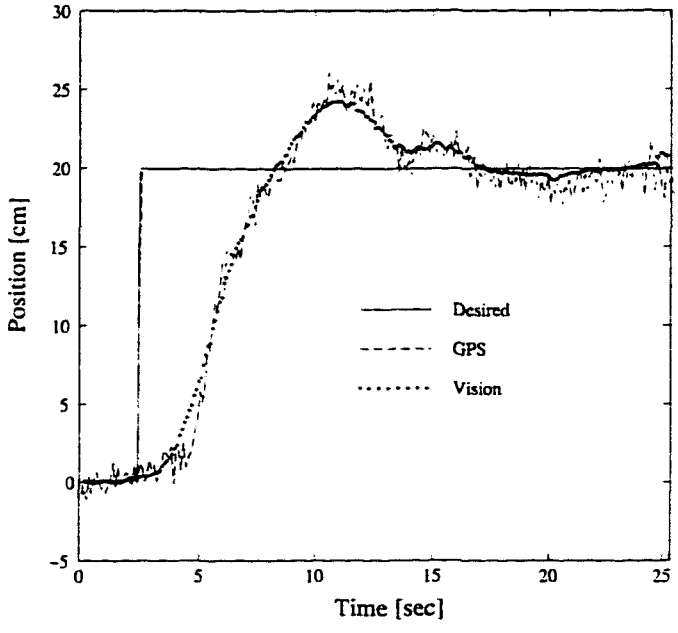

Figure 4.13: **Position Step Response**

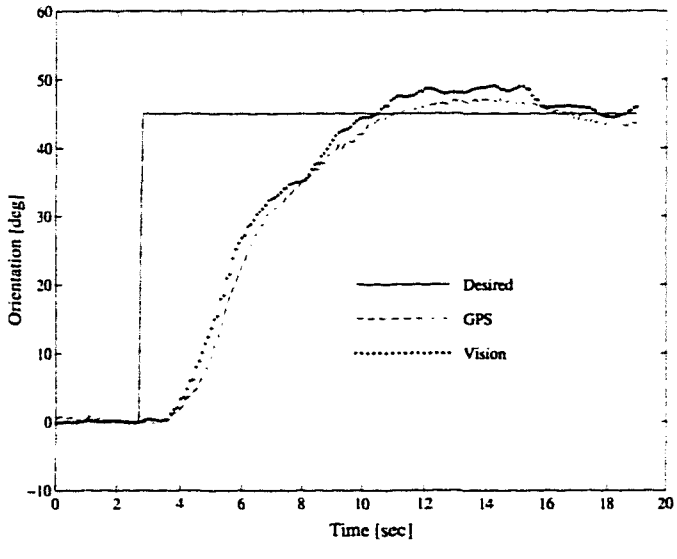

Figure 4.14: **Orientation Step Response**

	GPS Receiver Alone	GPS Sensor	Robot Base
Position	5 Hz	1.0 Hz	0.05 Hz
Orientation	5 Hz	1.5 Hz	0.2 Hz

Table 4.2: Bandwidth Parameters

Figure 4.15 shows how the original signal-flow diagram of 3.1 was modified to accomplish this. The Robot GPS Receiver was removed and its signals simulated using a *Signal Generator Component* and *State-to-Phase Component*. The *Signal Generator Component* simulates motions of higher frequency than are physically attainable with the thruster actuators, while the *State-to-Phase Component* merely maps these simulated position and orientation motions into corresponding phase measurements, which then feed into the nominal system. This serves as a smooth and repeatable means for generating a signal representative of actual motions of the robot.

The tests showed that the GPS sensor, which encompasses the receiver and the signal processing code, had an overall bandwidth of 1.0 Hz in position and 1.5 Hz in orientation. It is important to note that even though the function of the robot's GPS receiver was simulated for this test, the target's GPS receiver was producing live data, and thus realistic data delays existed.

Table 4.2 provides a summary of the bandwidths of different components in the system. The bandwidths for the robot base were measured by Russakow [35]. These are the most severe limitations (by a factor of 10 to 20) to the overall system performance. The parameter for the GPS receiver is based on the bandwidth of the phase filters internal to the receiver, while the bandwidths for the GPS sensor – the GPS receiver and subsequent signal processing – were measured as described above.

4.3.3 Stochastic Noise Characteristics

The stochastic noise levels of the GPS measurements affect the amount of filtering that needs to be performed before the measurements can be used for control. Figure 4.16 illustrates typical stochastic noise levels of the *unfiltered* position and orientation signals observed whenever both vehicles are immobile. Although the measurements are *not* stationary in a statistical sense (the standard deviations depend on where the vehicles are located in the workspace), the computed standard deviations provide a sense for typically observed

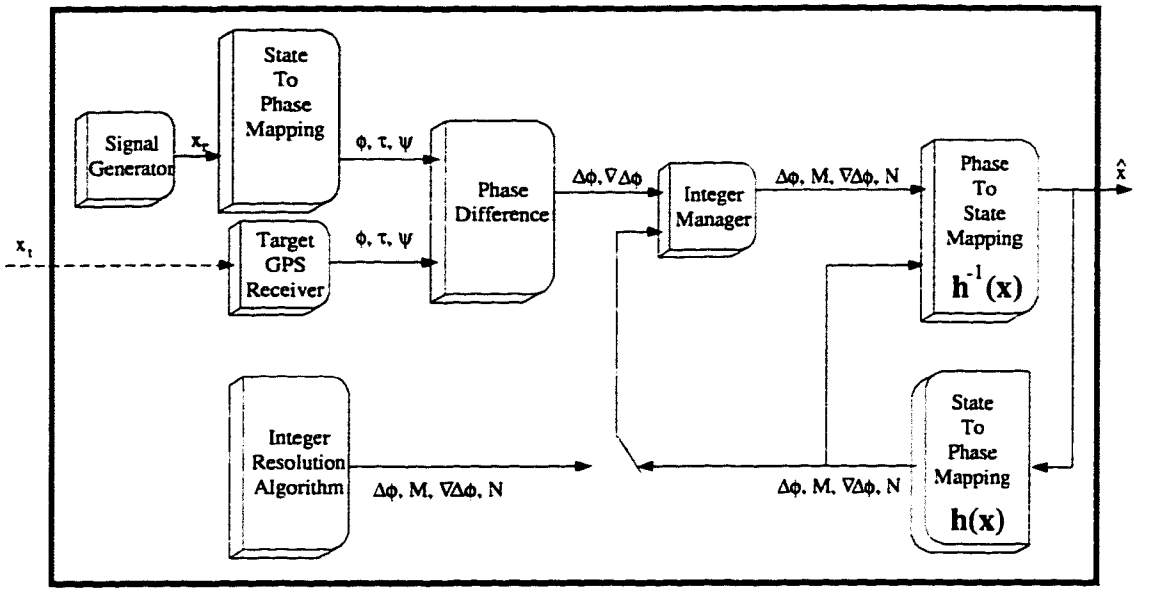

Figure 4.15: **Bandwidth Experiment Signal Flow Diagram**

The bandwidth of the GPS sensor was measured by simulating motion of the robot base and then feeding these motions into the real-time signal processing algorithms. The modifications to the nominal signal processing structure are shown in this diagram, emphasized in gray.

statistical characteristics. These values vary with location, because the received signal power also depends on location with respect to the transmitters. The relationship between the measured signal power and the variance of the phases is shown in Figure 3.5, and Table 4.3 summarizes the stochastic noise characteristics.

Although the stochastic noise levels affect the required amount of filtering that needs to be performed before the signals can be used for real-time control, they do not include the effects of the more serious *bias* error sources such as pseudolite and antenna baseline calibration errors, antenna phase-center stability, and multipath. The latter sources lead to direct errors in the vehicle position and attitude.

The comparison between the GPS and vision systems in the step response plot provides a sense of typical bias errors in the GPS measurements (e.g. the orientation error is approximately 3 deg around time $t = 15$ sec). The worst consequence of these errors is that when a pseudolite signal is acquired or lost, the recomputed integers for the new system configuration may be incorrect if the absolute position of either of the vehicles is off by

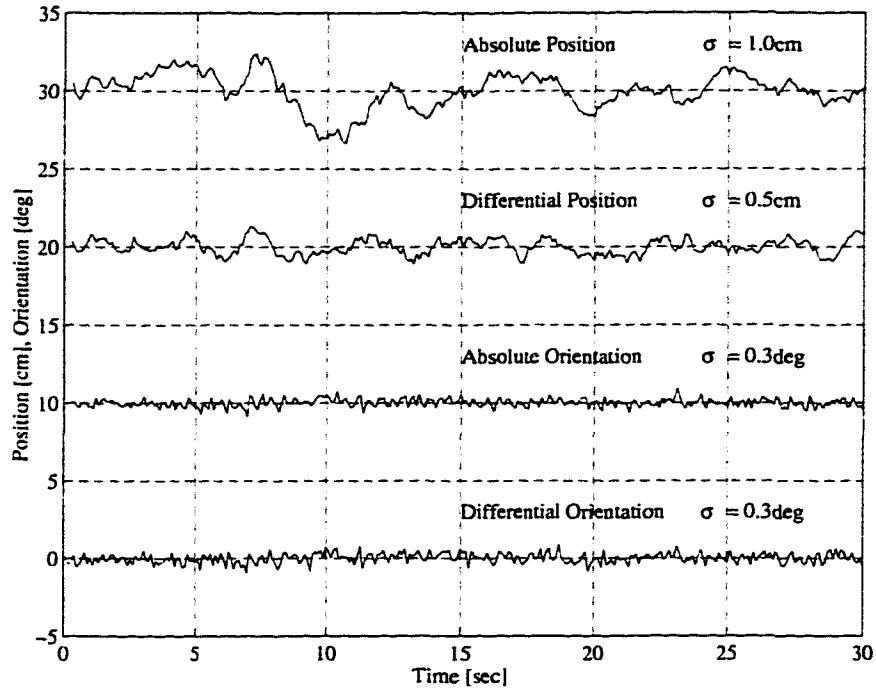

Figure 4.16: **Stochastic Noise Characteristics**

Parameter	Variance (3D kinematic)	Variance (2D EKF)
Differential Position	0.5 cm	0.3 cm
Absolute Position	1.0 cm	0.8 cm
Differential Orientation	0.3 deg	0.3 deg
Absolute Orientation	0.3 deg	0.3 deg

Table 4.3: Stochastic Noise Characteristics

more than half a wavelength (9.5 cm), and the system needs to be re-initialized using the vision system.

4.3.4 Bias Error Characteristics

Knowledge of the magnitudes and sources of bias errors in the phase measurements is critical to the reliability and accuracy of the GPS sensor. Bias errors not only contribute to steady-state errors in the solution of the system state, but also lead to discontinuities in

the solution when pseudolite signals are lost or gained. Since integer cycles are handed off whenever pseudolite signals are lost or gained, bias errors in *absolute* position can introduce random-walk drift in the position solution.

Significant effort was made to quantify the most likely sources of bias error in this system, which included multipath, antenna phase center variation, and circular polarization of the GPS signal. These sources produce errors that are dependent on the position and orientation of both vehicles. Monte Carlo simulations were performed to gain statistical measures of the impact of each of these biases on the estimated state. In simulation, the vehicles were placed in hundreds of random positions and orientations around the workspace while phase errors characteristic of each bias source were introduced. Finally, suggestions on how to better characterize and reduce such sources are provided.

Multipath

Multipath is a reflected signal that interferes with the the direct line-of-sight signal resulting in a phase measurement error. Two experiments were carried out to confirm the existence of multipath and to quantify it in the setting of this project.

Identification and Quantification of Multipath

The first experiment demonstrated the existence of multipath through the observation of signal-to-noise ratios. Periodicity in the signal-to-noise ratio with distance from the transmitting source is strong evidence of multipath, as the signal-to-noise ratio should otherwise be monotonically decreasing with distance. The periodicity occurs when multiple signals interfere constructively and destructively across a space of observation. Figure 4.17 shows SNR periodicity with distance and compares it with the theoretical SNR curve.

A second experiment was devised to establish statistical values for phase corruption due to multipath. A set of phase measurements was taken for a vehicle in the middle of the workspace with the workspace clear, and then three additional sets of measurements were taken with a large metal plate placed in various locations nearby. The average deviation between the phases measured with the plate and those without the plate were considered typical multipath values. Figure 4.18 shows the placement of the vehicle and the three locations of the 0.6 m x 1.0 m metal plate. The locations of the plate relative to the target in (x, y) coordinate pairs were (0.0 m, 1.0 m), (1.0 m, 0.0 m), and (0.0 m, -1.0 m). The

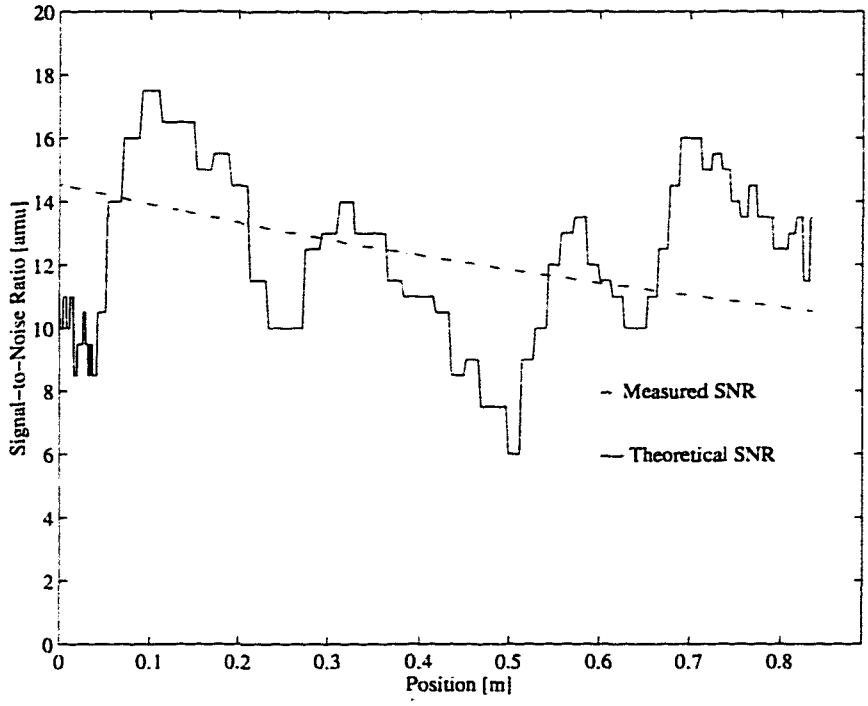

Figure 4.17: **Signal-to-Noise Ratio Periodicity**

Periodicity of the signal-to-noise ratio measurement with increasing distance from the transmitting source is evidence of interference between multiple signals. This plot shows the experimentally measured signal-to-noise ratio compared with the theoretical signal-to-noise ratio assuming no multipath signal. The frequency of the periodicity depends on the amplitude *of the reflected signal, which depends on the nature of the reflective environment.*

data collected in this experiment was used to generate a plot which exhibits the likelihood of a multipath error of a given magnitude to occur (Figure 3.8). Multipath was modeled as a random perturbation with these statistical characteristics and introduced into the phase-to-state algorithm in simulation in order to approximate the impact of multipath on the resolved state of the vehicle. The results of this simulation are shown in Figure 4.19. Table 4.4 is a summary of the standard deviations observed in these experiments. It is worth noting the likely cause and effect relationship between the differential position errors due to multipath and the autonomous intercept success rate (Section 4.1, Figure 4.8), as well as the relationship between the absolute position error due to multipath and the integer hand-off problem during configuration changes (discussed in Section 3.4).

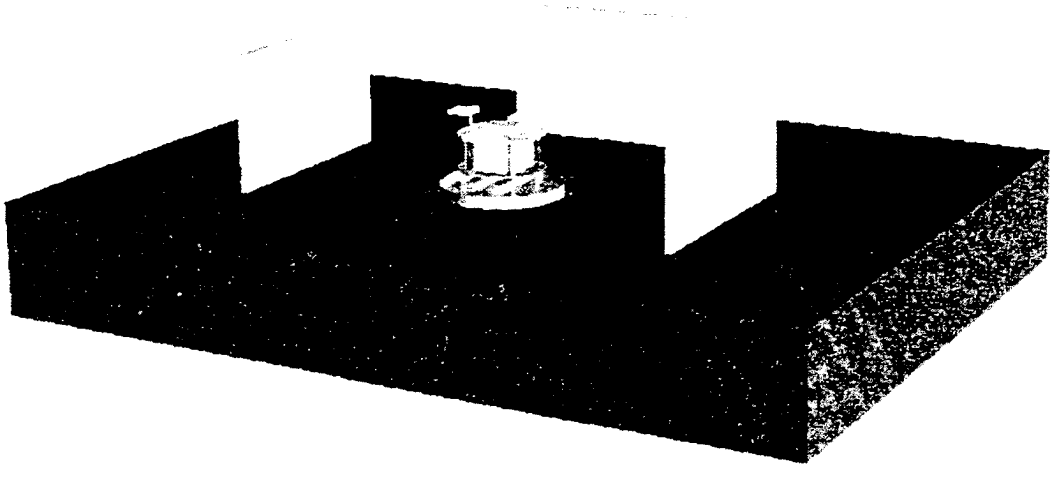

Figure 4.18: **Multipath Characterization Experiment**

In order to characterize the magnitude of multipath errors, phase measurements were taken with the target vehicle on a clear table and then with a metal plate placed in each of three different locations nearby. The differences in these measurements were collected to form a probability mass function which indicates the relative likelihood of a multipath error of a given magnitude to occur.

Suggestions for Reducing Multipath

This analysis indicates that multipath may be the single most dominating error source in the GPS sensor system. Other investigations, such as Lightsey [25], have shown similar results. The following suggestions are therefore provided as possible means for reducing multipath effects in future experiments:

- *Reduce the amount of reflected signals* - This concept is to reduce the problem at the source by decreasing the radio frequency (RF) reflectivity of the environment (at least the walls and vehicles, if not the air-bearing table). The laboratory could be outfitted with RF-absorbent material, such as carbon-impregnated foam rubber, in

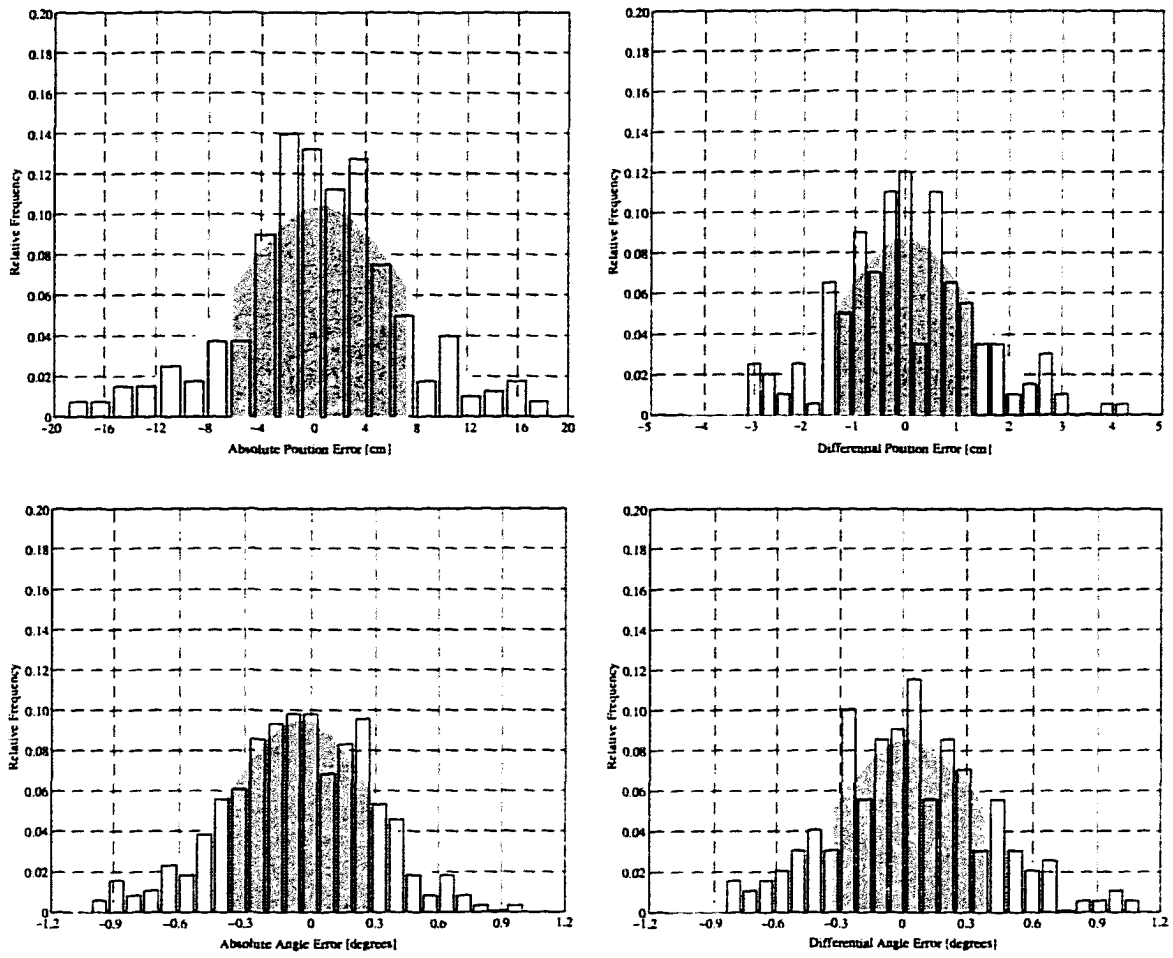

Figure 4.19: **Likelihood of Error Due to Multipath**

These plots show the relative likelihood of position and orientation errors of given magnitudes to occur due to multipath errors with empirically derived statistical characteristics (as shown in Figure 3.9). The standard deviations for these errors are summarized in Table 4.4. The one-σ band of each of these probability mass functions is delineated by the dark gray region.

the same manner that anechoic chambers are arranged[1]. A few simple experiments with such material would indicate the effectiveness of this concept. For instance, the reflective plate experiment discussed above could be performed again with the plate covered with RF absorbent material, and the phase deviations compared with the

[1]It has been offered that a qualitative measure of the effectiveness of a material can be gained by putting it in a microwave oven set at 60% power. The warmer the material gets, the more effective an absorber it will be [7].

above experimental results. In addition, the vehicles could be partially covered with this material and larger antenna ground planes could be added.

- *Transmit a narrower beam* - The helical antennas designed for this experiment transmit a conical beam that is about 50 deg wide. The limitation to making these narrower is the dynamic power range over which the receiver can lock on to the signal. A pulsed pseudolite similar to the one developed by Cobb [10] enables much greater dynamic power range. This could make it possible to use longer helical antennas with narrower beams, and hence reduce reflected signals. The pulsed pseudolite and its potential applications are discussed further in Chapter 7.

- *Model and cancel the multipath* - Techniques for modeling multipath in highly structured and predictable environments have been devised. Cohen [11] used spherical harmonics and Gomez, et. al. [41] used Uniform Geometrical Theory of Diffraction (GTD) to model multipath. To apply these techniques to an environment in which there are several *moving* reflective objects would be very difficult, but would be worth investigating.

- *Multipath suppression* - Section 3.4.2 discussed a means for limiting the effects of multipath by limiting phase measurements about those predicted by a dynamic model. For this experimental apparatus it was estimated that this technique effectively eliminated up to 20% of the multipath signal. Better knowledge of the system dynamics may enable greater effectiveness of this technique.

Antenna Phase Center Variation

Identification and Quantification of Phase Center Variation

An understanding of the entire signal propagation and data processing chain must be established in order to improve the resulting position determination. The effect due to phase center variation may be significant, so it is important to isolate and quantify the measurement contribution introduced by the phase characteristics of the antenna itself. An experimental setup for testing the phase center variation of an antenna is shown in Figure 4.20. In this experiment, the measured phase at the test antenna is compared with the signal generated by the pseudolite. The variation of this signal is then measured as the test

antenna is rotated on a gimbal about a fixed point. By rotating about the full useful range for the antenna, a map of the phase variation characteristics can be generated.

An experiment similar to the aforementioned setup was carried out by Clark [39] for several commercial antenna designs. Clark's study assumed that the variation was consistent from one antenna to another (deemed legitimate due to tight manufacturing tolerances on patch antennas), and independent of the azimuth angle. In general, the received phase is a function of both the azimuth and zenith angles, but for purposes of simplicity Clark's study defined the phase center of an antenna to be *the azimuth angle that provided the most symmetrical and smallest amplitude variation in phase over the range of the zenith angle.* The phase pattern measured for the Trimble 14532-00 patch antenna is shown in Figure 4.21. The plot evidences that the phase variation can be up to 0.8cm peak-to-peak. However, if the patterns are similar for two antennas and they are arranged coplanarly and in the same orientation, then the majority of the phase-center-variation error will cancel.

For the experimental apparatus used in this thesis, the intra-vehicle phase differences are virtually unaffected by phase center variations since the antennas on each vehicle are arranged coplanarly and in the same orientation. On the other hand, the inter-vehicle phase measurements can witness significant phase center variation effects, since the zenith and azimuth angles between master antennas of the two vehicles vary greatly with the relative position and orientation of the two vehicles.

In order to estimate the impact of phase center variation on the phase-to-state estimation process, the phase-to-state estimation procedure was run for 200 randomly distributed positions and orientations of the robot and target vehicle with simulated measurement errors based on phase center variations. Realistic phase-measurement errors were obtained by mapping the zenith angles between the receiver antennas and the transmitters to phase variations according to the data in Figure 4.21. The resulting statistical distributions from this study are shown in Figure 4.22. These plots show that the phase center variation effects on absolute and differential orientations are essentially insignificant ($\sigma = 0.02$ deg and 0.013 deg, respectively). This is not surprising, since the orientation is mostly dependent on the intra-vehicle phase differences, which are not appreciably affected by phase center variations. The absolute and differential positions were affected by the simulated phase center variation effects ($\sigma = 1.05$ cm and 0.18 cm, respectively), but not nearly as significantly as by the multipath effects.

Although the effects of phase center variation appear to be relatively small, it is worth noting that some issues have been simplified in this study. First, the phase patterns were simplified by ignoring the dependency on the azimuth angle. Second, the phase patterns of the transmitting antennas were ignored altogether. And finally, the phase patterns were assumed to be the same for all antennas. A more complete analysis would include individual phase patterns for all receiver and transmitter antennas, including azimuth dependencies. Also, the phase center patterns for all antennas should be measured with the ground plane in place, as this significantly affects the phase pattern.

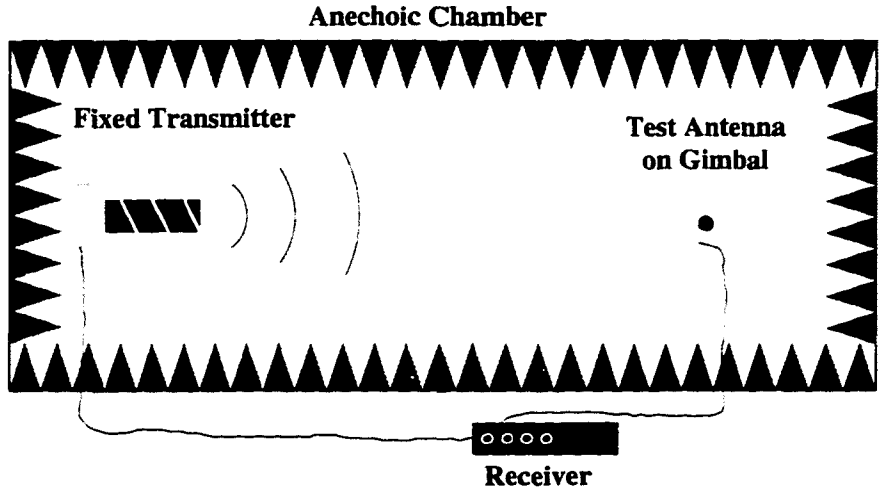

Figure 4.20: **Phase Center Measurement Experiment**

This experiment shows how the phase center variation of an antenna is measured in an anechoic chamber. The signal generated by the pseudolite is split and simultaneously broadcast through the transmitter antenna and sent directly to the receiver. The receiver antenna measurement is compared directly with the signal generated by the pseudolite as the receiver antenna is rotated on a gimbal about a fixed point. By rotating about the full useful range for the antenna, a map of the phase variation characteristics as a function of azimuth and zenith angles is generated.

Suggestions for Reducing Phase-Center-Variation Effects

There are two ways to eliminate phase-center-variation effects. The first is to eliminate the problem at the source. That is, reduce the size of the phase center characteristics

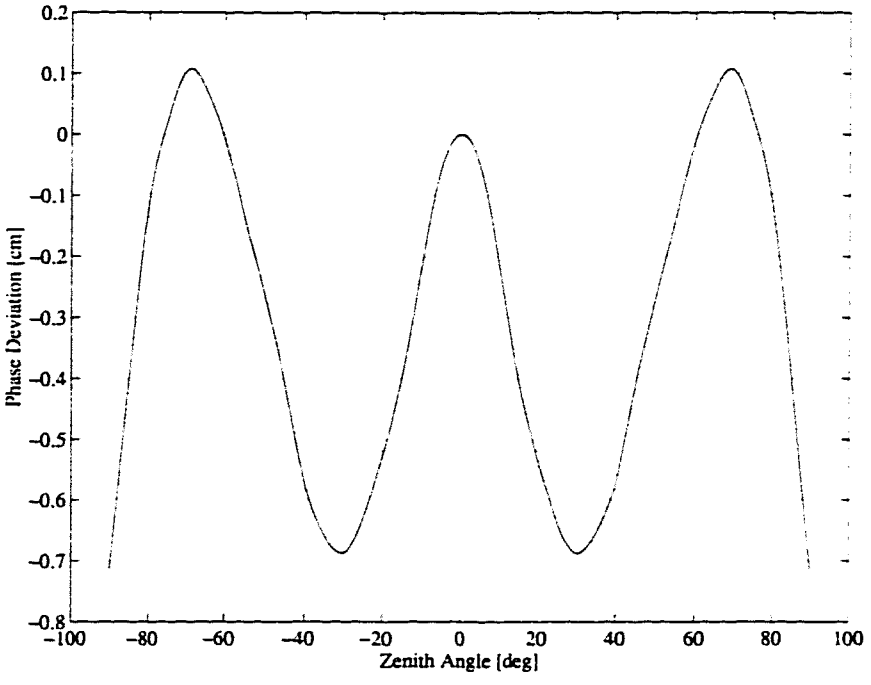

Figure 4.21: **Phase Center Map**

This plot is a replica of the phase pattern for the Trimble 14532-00 patch antenna as measured by Clark [39]. The pattern shown is the phase variation versus the zenith angle only. This pattern was measured at the azimuth angle that provided the most symmetrical and smallest amplitude variation in phase for the full range of the zenith angle.

of the antenna. Leisten and Ffoulkes-Jones have a concentrated effort to design a miniature dielectrically loaded volute antenna that has, among other desirable characteristics, minimum phase center variations [30]. The second way to eliminate phase-center-variation effects is to accurately model the antenna phase pattern and then directly remove it from the measurements. This can be done as follows. Including the phase center variation, the measurement equation (3.2) has an additional term γ_{ijk}. This term is a function of the phase characteristics of the transmitter and the receiver antenna, which in turn are functions of the position and orientation of the receiver antenna with respect to the transmitter antenna. Including this term in the measurement equation (3.2), the more accurate, yet more complex, measurement is:

$$\phi_{ijk} = |(P_i + R_i B_{ij}) - Q_k| + c\tau_{vi} + c\tau_{pk} + \lambda K_{ijk} + \gamma ijk \qquad (4.1)$$

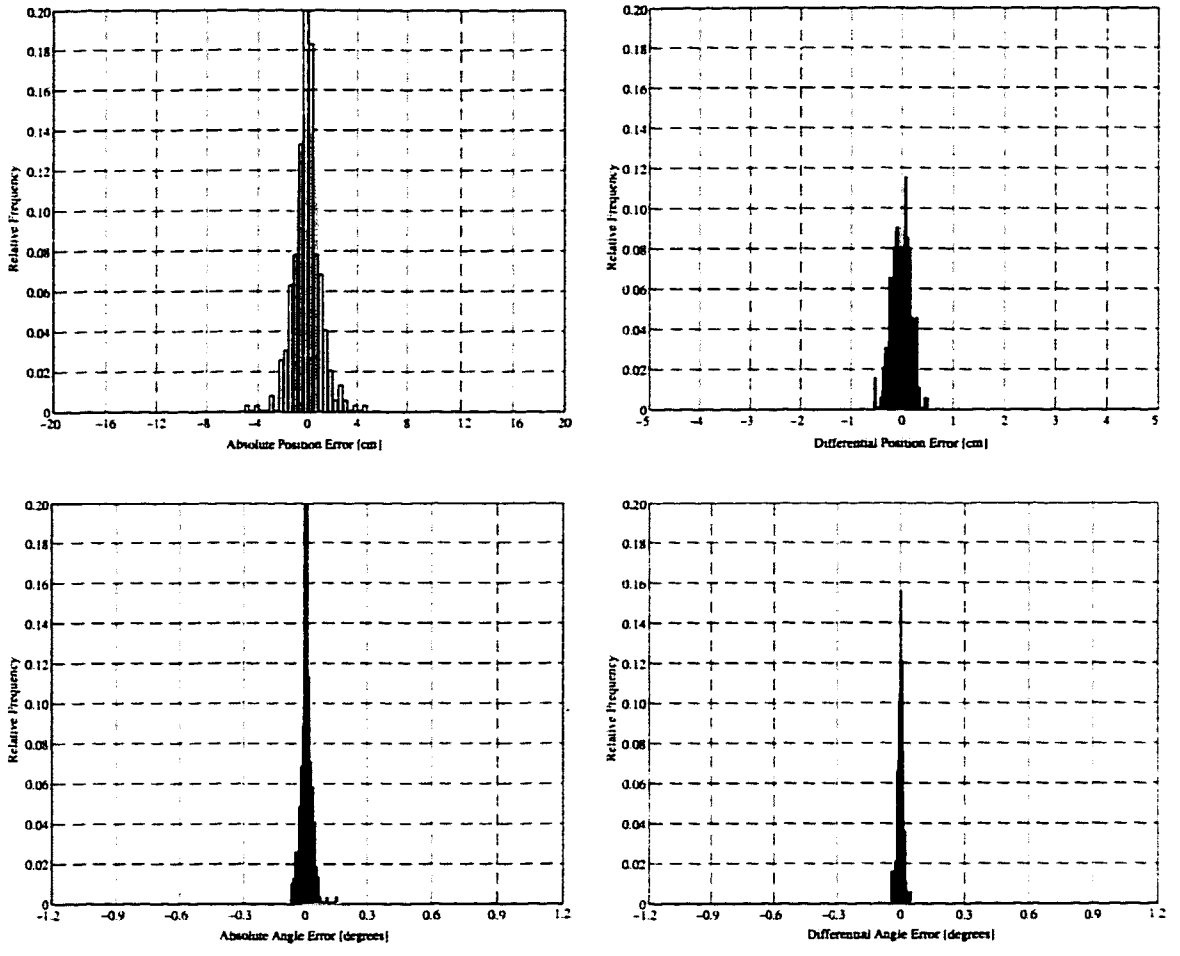

Figure 4.22: **Likelihood of Error Due to Phase Center Variation**

These plots show the relative likelihood of position and orientation errors of given magnitudes to occur due to phase center variations with empirically derived phase characteristics (as shown in Figure 4.21). The standard deviations for these errors are summarized in Table 4.4. The one-σ band of each of these probability mass functions is delineated by the dark gray region.

Since these equations are solved iteratively, the value for γijk would be obtained through a look-up table for the current estimate of the state, and then the estimation process would be repeated. However, the complexity added to remove this effect may not justify its incorporation. However, additional effects such as *phase polarization* can be removed in a similar manner. The contribution of phase polarization is discussed in the following section.

Phase Polarization

A characteristic of the NAVSTAR GPS signal is that it is Right-Hand Circularly Polarized (RHCP) over the majority of its exploited broadcast volume[2]. The effect of this characteristic is that the carrier phase measurement at any receiver antenna *depends not only on its position*, but also on its *orientation with respect to the transmitted field* as well as its *phase characteristics*. The effect can be ignored in situations in which the bore sites of the receiver antennas are aligned, since the differencing of the carrier phases between the antennas cancels the effect out. However, this effect must be taken into account in cases in which the antenna bore sites are not aligned, and in cases in which there is a significant variation in the polarization of the signal received by any two receiver antennas. This will occur if the transmitters are close to the receivers, as is the case for near-constellation systems.

Identification and Quantification of Phase Polarization

The goal of this analysis is to determine the extent of the polarization effect on the measured phase for a near-constellation system, with transmission though helical antennas and reception through patch antennas.

As with the inclusion of phase center variations, the inclusion of polarization effects causes the measurement equation (3.2) to have an additional term γ_{ijk} which is a function of the position and orientation of the receiver antenna with respect to the transmitter antenna (as well as the phase characteristics of the transmitter antenna and the receiver antenna). Including this term results again in the more complete measurement equation (4.1).

A study of the effects of polarization on the received signal was first published by Lawrence [14]. His analysis required the following assumptions:

- The line of sight to the transmitter antenna is the same for all receiver antennas.
- The bore site of the transmitter antenna is parallel to the line of sight to all of the receiver antennas.

This analysis generalizes the theory by *not* making these two assumptions, as they do not suit the near-constellation situation.

[2]The specification according to [29] is that the ellipticity for L1 is no worse than 1.2dB for the angular range of ± 14.3 deg.

A simple model for analyzing the phase of a helical antenna, ignoring the gain, is given in *radial coordinates* $< r, \theta, \phi >$ as:

$$E_{trans}(t) = \begin{bmatrix} 0 \\ A\cos(2\pi f_{L1}t) \\ \sin(2\pi f_{L1}t) \end{bmatrix}$$

where A is the axial ratio of the signal. An axial ratio of $A = 1$ represents a circularly polarized wave in all radial directions from the source. For a helical antenna, the polarization approaches circular as the antenna length increases. The axial ratios for the antennas used in this project are listed in Table 2.2.

The transmitted electric field must be converted to Cartesian coordinates, rotated into the receiver antenna's frame, and then projected onto the receiver antenna. Converting the transmitted electric field to Cartesian coordinates produces the equation:

$$E_{trans}(t) = \begin{bmatrix} \cos(t)\cos(\theta)\cos(\phi) - e\sin(t)\sin(\phi) \\ \cos(t)\cos(\arctan(\theta)\sin(\phi) + e\sin(t)\cos(\phi) \\ -\cos(t)\sin(\theta) \end{bmatrix}$$

where $\theta = \arctan(\frac{\sqrt{x^2+y^2}}{z})$ and $\phi = \arctan(\frac{y}{x})$, and x, y, and z are the coordinates of the location of the receiver antenna in the transmitter antenna frame. Rotating the signal from the transmitter frame to the receiver frame:

$$E_{rec}(t) = {}^{rec}R_{trans}E_{trans}(t) \tag{4.2}$$

where ${}^{rec}R_{trans}$ is the rotation matrix from the transmitter frame to the receiver frame. The output of a Right Hand Circularly Polarized patch antenna can be modeled as:

$$r(t) = \hat{i}_{rec} \cdot E_{rec}(t) + \hat{j}_{rec} \cdot E_{rec}(t - \frac{1}{4f_{L1}})$$

Inserting the electric field from (4.2), the received signal becomes:

$$r(t) = a\cos(2\pi f_{L1}t) + b\sin(2\pi f_{L1}t)$$

where

$$\begin{aligned} a &= R_{11}\cos(\theta)\cos(\phi) + R_{12}\cos(\theta)\sin(\phi) - R_{13}\sin(\theta) \\ &\quad + R_{21}e\sin(\phi) - R_{22}e\cos(\phi) \end{aligned} \tag{4.3}$$

and

$$\begin{aligned} b &= -R_{11}e\sin(\phi) + R_{12}e\cos(\phi) + R_{21}\cos(\theta)\cos(\phi) \\ &\quad + R_{22}\cos(\theta)\sin(\phi) - R_{23}\sin(\theta) \end{aligned} \tag{4.4}$$

This is equivalent to a received signal

$$r(t) = a\cos(2\pi f_{L1}t + \arctan(b/a))$$

where the phase shift due to polarization is

$$\arctan(b/a) \tag{4.5}$$

These formulas were used to simulate the phase variation incurred due to polarization. It is worth noting that in the limit, as the transmitter antennas are moved to locations far from the receiver antennas ($\theta \to 0$ and $\phi \to 0$), the result derived in (4.5) approaches the result derived by Lawrence [14]:

$$a = R_{11} - eR_{22}$$

and

$$b = eR_{12} + R_{21}$$

Simulation of the Polarization Effect

Two types of simulations were run to gain better insight into the polarization effect. The first simulation consisted of measuring the amount of phase variation introduced into the double-differenced phases $\nabla\Delta\phi$ when the target vehicle was fixed in the middle of the workspace and the robot was positioned at 0.1 m-spaced grid points distributed across the

entire workspace. The resulting variations of the double-differenced phases were then plotted against the robot's location on the table to form a three-dimensional surface illustrative of the phase distortion due to polarization. Figure 4.23 shows the polarization-effect surface for a single double-difference between the first two pseudolites and the robot and target vehicles. As anticipated, the greatest variations occur at the edges of the workspace where the robot was farthest from the target vehicle. These are the locations at which the bore-site vectors of each receiver antenna subtends the greatest angular difference between the line-of-sight vectors to the pseudolites. Almost no variation exists where the robot was collocated with the target in the middle of the workspace. Here the bore-site vectors of each receiver antenna subtends the same angle between the line-of-sight vectors to the pseudolites. The worst-case variation of the double-difference phase due to this effect can be seen to be up to 5 cm across the entire workspace.

Although the polarization effect is clearly dependent on the relative locations of the two vehicles, a statistical analysis using random locations across the workspace was performed in order to compare this bias error source with the two previous bias sources. Again, 200 randomly distributed positions and orientations of the robot and target vehicle were simulated with polarization bias errors introduced into the phase measurements. These phases were then run through the phase-to-state algorithm and the resulting position and orientation errors were compiled in histograms to show the likelihood of a polarization error of a given magnitude to occur. Figure 4.24 shows these distributions, while Table 4.4 is a summary of the standard deviations observed in these experiments and compares them with the results from the other bias error experiments.

Suggestions for Reducing Phase Polarization Effects

The most direct method for removing the effect of phase polarization is to include the effect in the measurement equations that are solved to derive the vehicle states. The means for doing this is straightforward, as shown by equation (4.1). The only penalty of this addition is the increased complexity and hence the greater computational burden.

The effects of these bias errors on the estimated state of the vehicles were compiled for comparison and are listed in Table 4.4. Also tabulated is the cumulative effect of these biases, assuming they are independent Gaussian random variables. The cumulative effect of

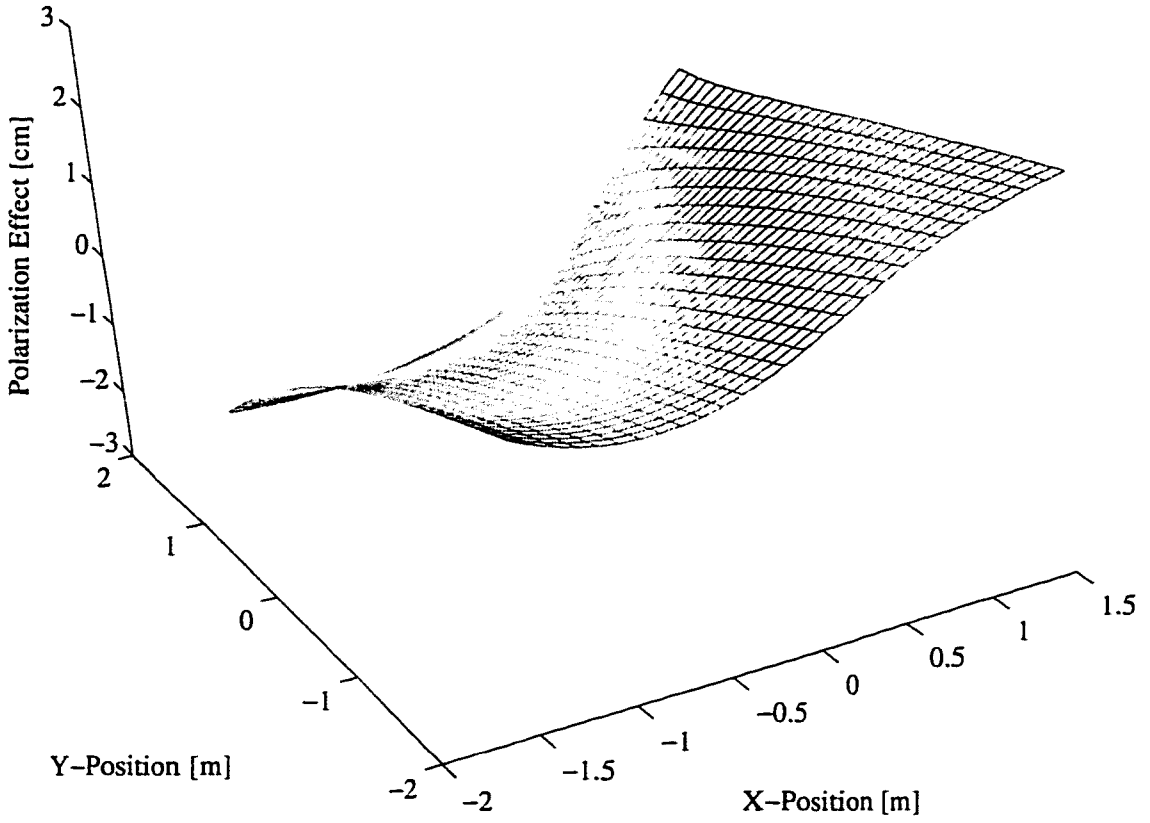

Figure 4.23: **Polarization Effect on Double-Differenced Measurement**

the bias errors on the differential position and orientation attribute to experimental system performance of Figure 4.8.

4.4 Summary of Experimental Results

This chapter has presented detailed discussions of the operation and performance of the pseudolite-based GPS prototype space robot system. The autonomous-rendezvous and formation-flying demonstrations have shown that GPS can serve as a real-time sensor to provide three-dimensional position and orientation, and thus provide the high degree of vehicle autonomy required to execute commands directed at the *task level* by the human

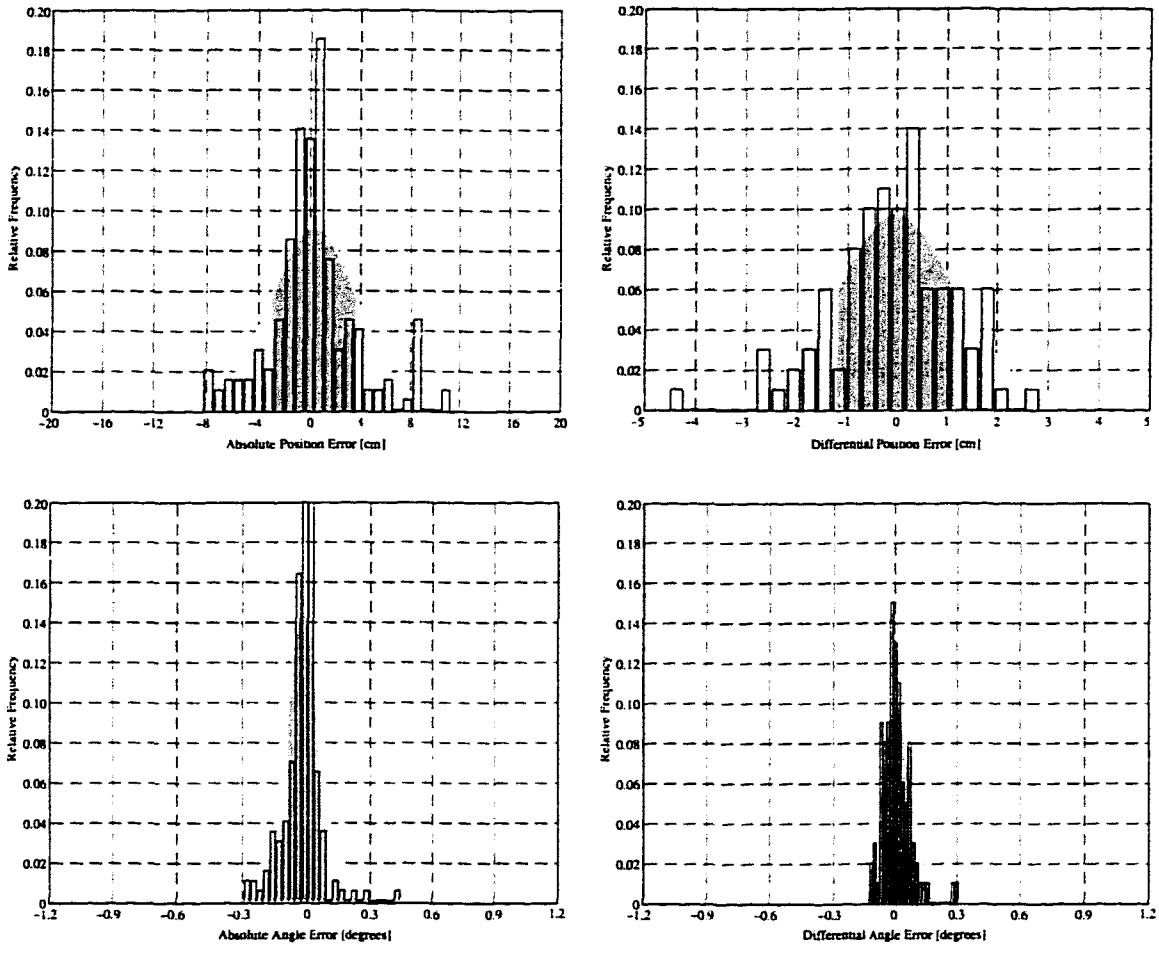

Figure 4.24: **Likelihood of Error Due to Phase Polarization Effects**

These plots show the relative likelihood of position and orientation errors of given magnitudes to occur due to phase polarization. The standard deviations for these errors are summarized in Table 4.4. The one-σ band of each of these probability mass functions is delineated by the dark gray region.

Parameter	Multipath	Phase Center	Polarization	Calibration	Cumulative
Absolute Position	10.2 cm	1.1 cm	3.4 cm	3.0 cm	11.2 cm
Differential Position	2.0 cm	0.2 cm	1.2 cm	1.1 cm	2.6 cm
Absolute Angle	0.49 deg	0.02 deg	0.08 deg	0.19 deg	0.53 deg
Differential Angle	0.53 deg	0.01 deg	0.07 deg	0.09 deg	0.54 deg

Table 4.4: Bias Error Standard Deviations

operator. Performance characteristics from these experiments, in addition to bandwidth and step-response experiments, provide useful guidelines for designing future operational GPS-based robotic systems. Finally, analyses and detailed suggestions for improving the overall performance of this original system were provided.

Chapter 5

Initialization

A fundamental challenge of Differential Carrier Phase GPS is that the number of integer cycles between any two receiver antennas must be deduced before differential *phase* measurements can be translated into differential *range* measurements. Many algorithms for resolving integer cycle ambiguity have been developed, however the unique characteristics of the near-constellation GPS preclude the direct application of any of these. Although previously demonstrated techniques cannot be directly applied, similar approaches can be taken. The technique pursued in this thesis uses vehicle motion to resolve the integers, and the new algorithms were implemented and tested in simulation.

5.1 Initialization Techniques

In practice there are potentially two sets of integers that need to be resolved: those between antennas on the same vehicle, and those between antennas of separate vehicles. As established in Chapter 3, these two sets of variables are referred to as *intra-vehicle integers* and *inter-vehicle integers*, respectively. Generally, the intra-vehicle integers are related to the attitude of the vehicle, and the inter-vehicle integers are related to the relative positions of the two vehicles.

The resolution of intra-vehicle integers is a well-studied problem and many techniques exist, including motion-based techniques [11] and exhaustive search algorithms [16]. This is not the case for inter-vehicle integer resolution, since resolution of these values typically is an application-specific problem. The IBLS aircraft landing system of [9] accomplishes the equivalent of inter-vehicle integer resolution through the use of fixed-reference ground-based

pseudolite beacons. Others, including Conway [12] and Montgomery [27], used surveyed starting locations to initialize the inter-vehicle integers, and relied on constant signal lock to maintain the integers. With regard to the last three references, the second "vehicle" is a fixed ground-based reference receiver.

The integer resolution algorithm developed in this thesis takes advantage of the increased geometric observability afforded by the close proximity of the transmitters. The increased geometric observability is in fact the motivation for the ground-based transmitters in the aforementioned work of [9]. In consideration of rendezvous between two vehicles in space, it will be necessary for at least one vehicle to be equipped with one or more transmitters to provide the same geometric observability. Such a scheme is discussed further at the end of this chapter. Also considered in this chapter is the use of integrated sensors, such as accelerometers, to provide additional information to aid the integer resolution process.

5.2 Integer Resolution for Near-Constellation GPS

5.2.1 Logistics

At the highest level, initialization via Near-Constellation is first a question of logistics and then a question of algorithmic development. In other words, how does one physically go about initializing the system? Several scenarios for the system studied in this thesis can be imagined:

1. *Manually induced motion, no system knowledge* - Under this scenario, the vehicles are moved around the workspace by hand in order to collect samples of changing phases to be used in the integer estimation process. Since no system knowledge is assumed, the vehicles can be moved around the workspace at random, both translationally and in orientation. Any algorithm designed to work under this scenario would be rather generic in that it need not incorporate specific system knowledge, but it would require a more accurate initial guess as well as require a longer time to converge than if some knowledge were incorporated.

2. *Manually induced motion, known system dynamics* - Under this scenario, the vehicles are freely tossed across the workspace at fixed translational and angular velocities as phase data is collected. Unimpeded two-dimensional free-body motion can be assumed, and this information can be incorporated into the integer resolution algorithm.

Knowing that the vehicle traveled in a straight line with constant translational and angular velocity should improve the robustness of the algorithm.

3. *Vehicle-induced motion, known system dynamics* - Rather than manually moving the vehicles around the workspace, the vehicles could propel themselves around the workspace, albeit in an open-loop manner. Accurate knowledge of thruster firings could be used to help predict the undergone motion via dead reckoning, and this information could then be added to the integer resolution algorithm (of course, accelerometers would greatly improve this procedure).

In addition to these initialization scenarios, there are several ways that information can be added to assist the initialization process. These include:

- *Use of signal-power measurements* - signal power obtained from the signal-to-noise ratio can be used to help establish a rough estimate of the vehicle position and orientation. This is an opportunity to take advantage of the extreme dynamic range characteristic of the Near-Constellation system.
- *Short-baseline antennas* - A set of antennas mounted less than one wavelength apart can be used to achieve an immediate rough estimate of vehicle orientation. After the rough estimate is established, the system can switch to the wide-baseline antennas for greater accuracy.
- *Supplemental sensors* - Sensors such as accelerometers and gyros could be added to assist the dead-reckoning process to further aid the integer resolution algorithm, as mentioned in the *Vehicle-induced motion scenario* above.

The method developed in this chapter assumes manually induced motion with no system knowledge, and does not take advantage of any additional sensors.

5.2.2 Approach

A characteristic of the near-constellation system is that the intra- and inter-vehicle integers are co-dependent. That is, the measured intra-vehicle differential phases will be different for a given orientation, depending on where the vehicle is located in the workspace. (This is *not* true for a far-constellation system.) Therefore, it is not possible to solve for the two sets of integers independently. Since the intra- and inter-vehicle measurements are

co-dependent, the absolute positions and orientations (and thus the integer ambiguities) can be established through multiple intra-vehicle phase measurements alone (for a single vehicle). The complete process for resolving integers for a near-constellation system is as follows:

- The user manually moves a single vehicle around the table in a random-walk manner, both in position and orientation.
- Measurements are automatically taken at points in which a significant change in the magnitude of the phase measurement vector has been detected, indicative of a significant change in the position of the vehicle from the previous sample point. Data samples taken relatively close together do not provide innovative information to the system.
- The vehicle is then grounded while the initialization algorithm is executed. The vehicle's computer iteratively estimates the time history of all of the states of the vehicle for every sample point, effectively resolving the integers.

5.2.3 Theoretical Derivation

The objective of the integer resolution process is to accumulate phase measurements for a single vehicle over several samples in the workspace and then resolve the state of the vehicle at every sample point in a single extensive non-linear least squares batch process. Of course, for each measurement taken, a new set of vehicle states is accumulated, so it is necessary to accumulate measurements faster than new states. Since there are 18 new measurements and only seven new vehicle states at each time step, the number of measurements do accrue faster than the number of unknowns.

The equations for the integer resolution algorithm can be derived from the basic phase measurement equation (3.2) as described below. Since there is no knowledge of the integer cycle ambiguities, M_{ijk}, they must be eliminated through phase differencing over time. Starting with the intra-vehicle phase difference from equation (3.3):

$$\Delta_1\phi_{ijk} = |(P_i + R_iB_{im}) - Q_k| - |(P_i + R_iB_{ij}) - Q_k| + \lambda M_{ijk} \tag{5.1}$$

The time difference results in:

$$\begin{aligned}\delta\Delta_1\phi_{ijk}(t_1,t_2) &= |(P_i(t_2)+R_i(t_2)B_{im})-Q_k|-|(P_i(t_2)+R_i(t_2)B_{ij})-Q_k|- \\ &\quad |(P_i(t_1)+R_i(t_1)B_{im})-Q_k|+|(P_i(t_1)+R_i(t_1)B_{ij})-Q_k| \\ &= h(X_i(t_1),X_i(t_2))\end{aligned} \tag{5.2}$$

In addition to the intra-vehicle phase differences, there are physical constraints that must be incorporated into the algorithm. The constraints derive from the condition that the *magnitudes* of the intra-vehicle baselines between master and slave antennas remain constant across sample times due to the fact that the antennas remain in fixed locations on the vehicle. Assuming y_{ij} to be the baseline vector between the master antenna and slave antenna j for vehicle i in the world frame, and Δy_{ij} to be the change in that vector from one time sample to the next, the constant-magnitude constraint, as shown by Cohen [11], Section 3.1.2 is:

$$\Delta y_{ij_1}^T y_{ij_2} + \Delta y_{ij_2}^T y_{ij_1} + \Delta y_{ij_1}^T \Delta y_{ij_2} = 0 \tag{5.3}$$

Where j_1 and j_2 may be different antenna indices to incorporate cross-correlation terms.

The baseline between the the master and slave antennas in the world frame can be related to the parameters defined in Figure 3.4 as follows. The position of each antenna is:

$$P_{ij} = P_i + R_i B_{ij}$$

The baseline between the slave antennas and the master is:

$$y_{ij} = P_{ij} - P_{im}$$

and the change of this vector across time samples:

$$\Delta y_{ij}(t_1,t_2) = y_{ij}(t_2) - y_{ij}(t_1)$$

All unique (j_1, j_2) pairs for equation (5.3) can be incorporated into a 6×1 constraint vector and represented as $h_c(X_i(t_1), X_i(t_2))$.

Stacking the measurements (5.3) and the constraints (5.3) over N sample points produces the complete set of equations to be solved in the non-linear least squares batch process:

$$\begin{bmatrix} \delta\Delta_1\phi_{ijk}(t_1,t_2) \\ 0 \\ \delta\Delta_1\phi_{ijk}(t_2,t_3) \\ 0 \\ \vdots \\ \delta\Delta_1\phi_{ijk}(t_{N-1},t_N) \\ 0 \end{bmatrix} = \begin{bmatrix} h(X_i(t_1,t_2)) \\ h_c(X_i(t_1,t_2)) \\ h(X_i(t_2,t_3)) \\ h_c(X_i(t_2,t_3)) \\ \vdots \\ h(X_i(t_{N-1},t_N)) \\ h_c(X_i(t_{N-1},t_N)) \end{bmatrix} \tag{5.4}$$

5.2.4 Simulation Results

The algorithm derived in the previous section was first implemented and demonstrated in simulation. Manually induced random-walk vehicle motion in six degrees of freedom was simulated, and the corresponding phase data were collected for eight sample points in the workspace. A batch least-squares process was performed on the data to demonstrate the convergence of the algorithm.

The convergence sequence is shown graphically in Figure 5.1 through several iterations. Two plots are shown for each iteration. The upper plot is a graphical representation of the translational path that the vehicle followed, while the lower plot shows the three rotational angles of the vehicle at each of the eight time samples. The sample points of the actual states are shown in black and designated by "o" while the estimated states are shown in gray and designated by "x". The initial estimates for the position were set according to a random-walk path contained within the useful workspace, while the initial rotational angles were arbitrarily set to a fixed orientation. In order to achieve convergence, the position path must be within the table workspace, and the rotational angles generally need to be within 45 degrees of actual. Section 5.2.1 discussed possible ways to add information to assist the initialization process.

This particular sequence shows the orientation convergence after only four iterations, while the position-path convergence required several more iterations. Once convergence is complete, it is a trivial step to back out the integers from the known states according to

the single difference equation (3.3). In fact, there are N redundant measurements of the integers which can be compared to establish a measure of confidence in the results.

5.2.5 Positioning Via Signal Power

It is conceivable to use the measured signal power to establish a rough estimate of the location of the vehicle to aid the integer resolution algorithm discussed in the previous section. The measured signal-to-noise ratios are approximately linear with signal power and could be collected simultaneously with the phase measurements during the initialization procedure. The measured signal-to-noise ratios could be mapped to positions in the workspace via the theoretical model or through the use of a large look-up table. The following development shows a comparison between the theoretical signal power and experimental data across a significant portion of the workspace.

Helical Antenna Gain Pattern

The received signal power is predominantly a function of the antenna gain pattern and the distance from the transmitting source. From Balanis [2], the far-field pattern can be described by:

$$E = \sin(\frac{\pi}{2N})\cos(\theta)\ \frac{\sin((N/2)\psi)}{sin(\psi/2)} \tag{5.5}$$

where

$$\psi = 2\pi(\frac{\lambda}{S}(1-\cos(\theta)) + \frac{1}{2N})$$

and the parameters N and S were defined in Section 2.3.3. The relative power can be derived from the square of equation (5.5) divided by the square of the distance from the transmitter (the singularity at $r = 0$ may be ignored since this analysis is for the far-field pattern in which r is 10 times the length of the antenna).

Experimental data were collected by placing an antenna at 0.2 m grid spacings over an area of 4.2 m of the workspace and measuring the signal-to-noise ratio of a pseudolite signal at each location. The pseudolite was located at coordinate (0.0, 3.93, 1.2) and oriented with its antenna bore-site pointing along the negative Y-axis of the workspace frame (as defined in Figure 4.4). The data-collection workspace grid covered a box defined

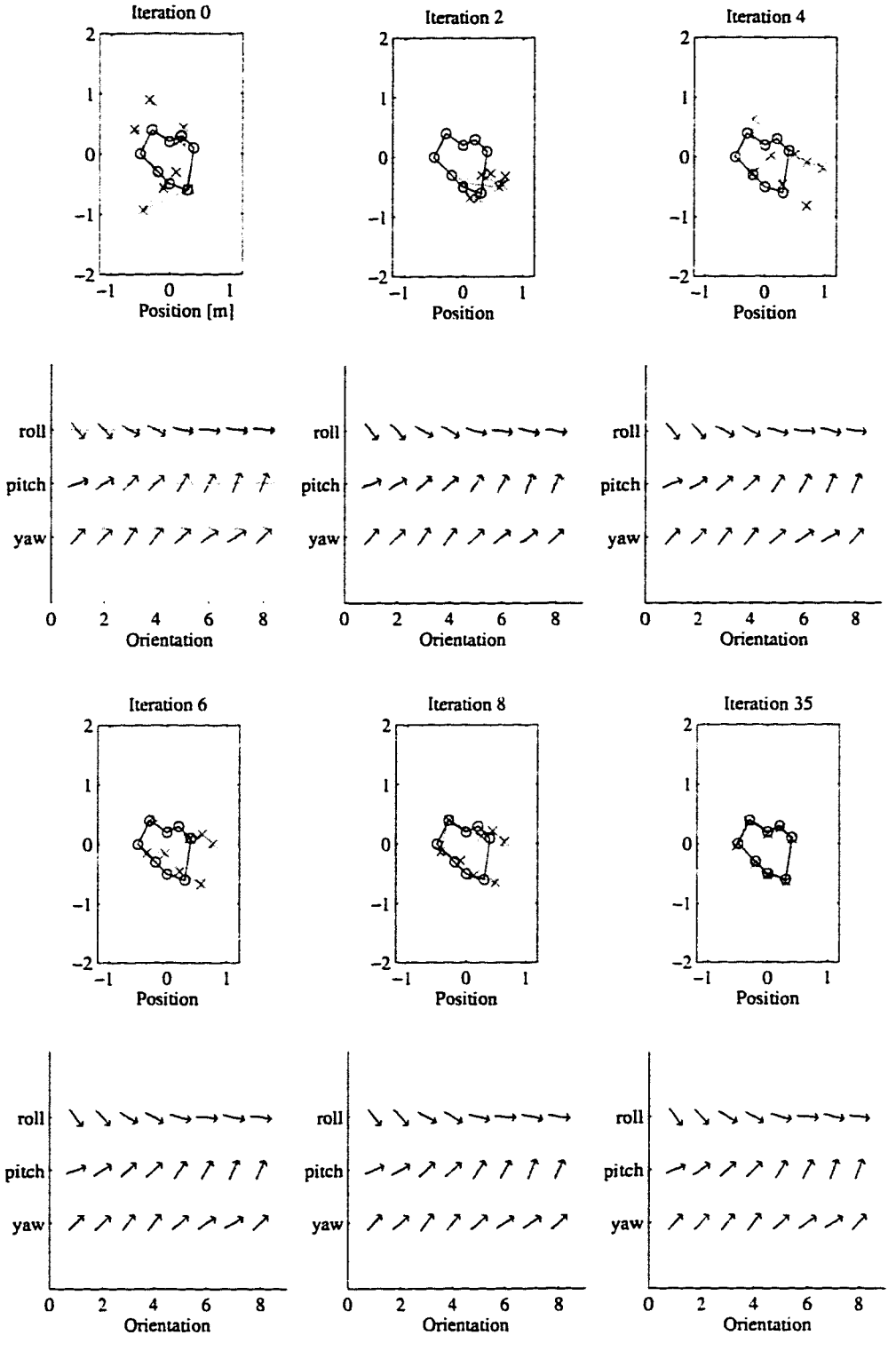

Figure 5.1: **Integer Resolution Convergence Sequence**

by $(-0.82 < x < 0.58, -1.17 < y < 1.83)$, and the receiver antenna bore site was fixed along the positive Y-axis, facing the pseudolite.

Figure 5.2 shows the theoretical relative power for the environment around the pseudolite transmitter. The region for which data was taken is shaded. Close-up, perpendicular views of the power surface are shown in Figures 5.3 and 5.5. These can be compared to the experimental data shown in Figures 5.4 and 5.6. The experimental data follows the general trend of the theoretical model, but is characterized by quite a bit of noise. This is consistent with the results of the analysis in Section 4.3.4, Figure 4.17. This crude measurement could provide enough information to identify the vehicle's location to within the correct quadrant of the workspace, which would be a useful starting point for the integer resolution algorithm developed in the previous section.

The greatest deviation between the theoretical model and the experimental data occurs along the X-axis boundaries closest to the transmitter. This may well be due to having neglected of the receiver antenna's gain pattern in the theoretical model. The points where the deviation is greatest are the points in which the receiver antenna experiences the largest zenith angle of the incoming signal (and hence a significantly lower gain).

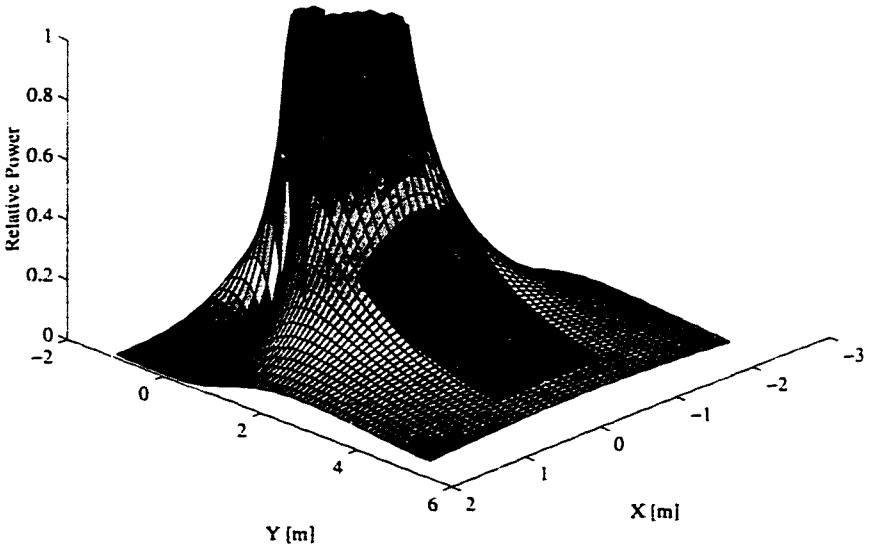

Figure 5.2: **Theoretical Signal Power Based on Antenna Pattern**

This plot shows the theoretical relative signal power of the broadcast signal based on the helical antenna gain pattern. The pseudolite antenna was located at the origin of this plot, broadcasting out along the y-axis. The dark patch shows the area of the workspace for which signal power data was taken and displayed in subsequent plots.

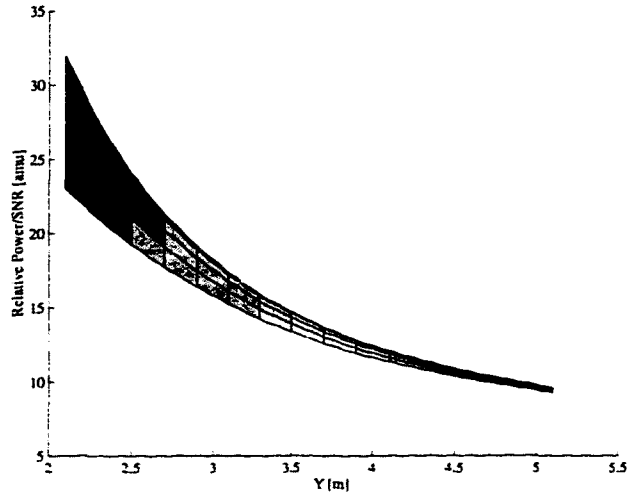

Figure 5.3: **Theoretical Signal Power – Side View**

This plot shows a side view of the portion of the signal power surface for which experimental data was taken. The relative power has been scaled to coincide with the signal-to-noise ratio measurements obtained from the receiver. The units "amu" (amplitude measurement units) represents a measure of how well the received signal correlated with the internally generated signal.

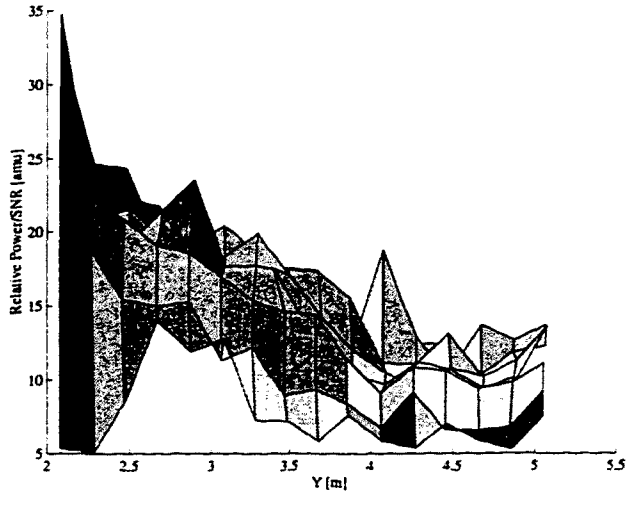

Figure 5.4: **Experimental Signal Power – Side View**

This plot shows the side view of the experimentally measured signal-power surface for which experimental data was taken.

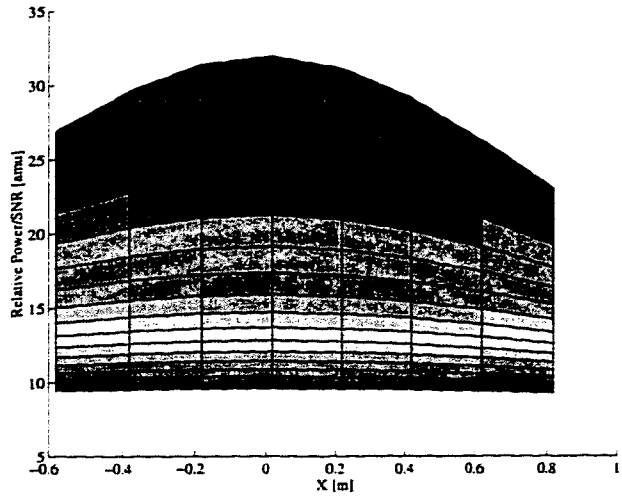

Figure 5.5: **Theoretical Signal Power – Front View**

This plot shows the front view of the portion of the signal-power surface for which experimental data was taken.

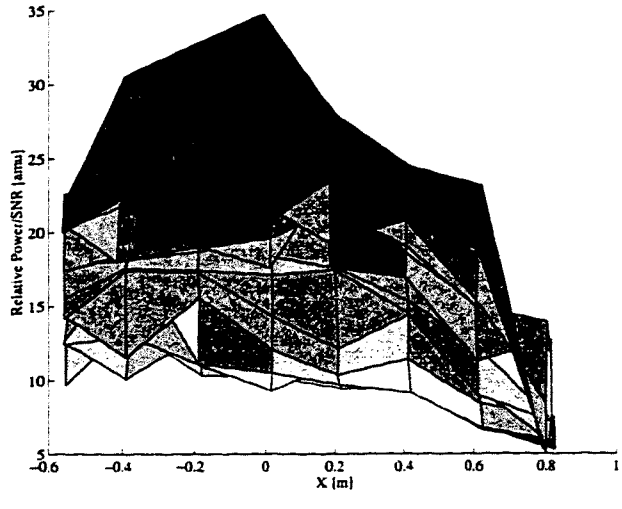

Figure 5.6: **Experimental Signal Power – Front View**

This plot shows the front view of the experimentally measured signal-power surface for which experimental data was taken.

5.3 Application to Space Systems

Although a space version of the system studied in this thesis would have different requirements for resolving integer cycle ambiguities some of the concepts from the above development could be applied. The intra-vehicle integer resolution could be accomplished through existing techniques. The difficulty, once again, lies in determining the inter-vehicle cycle ambiguities among multiple spacecraft. It is highly unlikely that there would be sufficient observability from the NAVSTAR GPS satellites alone to resolve these ambiguities. It would therefore be necessary to place local transmitters on board at least one of the spacecraft to achieve the necessary observability. In addition to improving the geometric observability of the measurements, the incorporation of local tranmitters can help overcome occlusion problems. This concept is discussed in more detail in Chapter 7, along with the concept of placing a set of transmitters on the Space Station to form a local Near-Constellation system that would aid nearby autonomous vehicles.

Chapter 6

Calibration

This chapter discusses the methods used to calibrate several parameters of the GPS sensors. Amongst these parameters are the pseudolite locations, the receiver antenna baselines, and the receiver antenna line biases [1]. It has been shown that calibration of the pseudolite locations is very sensitive to knowledge of the vehicle receiver antenna baselines, and vice-versa. The interdependence of these parameters in conjunction with unmodeled bias sources complicate the calibration process. Therefore, techniques to minimize the effect of this interdependence are discussed, and an analysis of bias error sources is provided.

6.1 Calibration Approaches

Three approaches were investigated for calibrating transmitter locations and receiver antenna baselines. The first two approaches proved to be very sensitive to the interdependence of the pseudolite positions and receiver antenna baselines, while the third approach was designed to be insensitive to this interdependence. The general approach was to collect phase measurements for known vehicle locations distributed throughout the entire workspace volume, and then perform a batch least-squares fit to determine the set of unknown parameters. The overhead vision system (discussed in Section 2.5) was used to provide vehicle location information. Nonlinear equations relating the unknown calibration parameters to the measured phases were derived through differencing of the phase measurement equation 3.2.

[1] More precisely, the parameters that are estimated are the phase center locations of the pseudolite transmitter antennas and the phase center locations of the receiver antennas on the vehicles

These equations were linearized about the antenna baselines, B_{ij}, and the pseudolite positions, Q_k, and then used in the batch recursive least-squares algorithm.

Sample Space Selection

The observability of the parameters estimated in all of the calibration approaches varies with the sample volume over which data is collected. The location of each pseudolite is essentially the center of a *sphere* of constant phase, so it is important to take calibration data over a three-dimensional volume. The limited area of the air-bearing workspace, along with the physical limitation of manually moving the vehicles around in only two dimensions restricted the sample space volume. In order to obtain measurements in three dimensions, all of the antennas of each vehicle were mounted on plates that could be raised above the main structure of the vehicles and rotated out of plane. Calibration of the parameters for each vehicle can be performed independently, and an example of a calibration data sample space is shown in Figure 6.1. The total number of phase measurements collected for parameter estimation is $N_{sample\_locations}$ x $N_{baselines}$ x $N_{pseudolites}$.

Approach 1: Assume pseudolite locations known, estimate receiver antenna baselines

The first calibration approach assumed the pseudolite locations were known reasonably well through rulered measurements, leaving only the receiver antenna baselines to be determined. The calibration measurement equation (6.1) was linearized about the vehicle baselines, B_{ij}, while the pseudolite positions, Q_k, were treated as fixed, known parameters. This approach was tested in simulation using 50 data-sample locations throughout the workspace (as shown in Figure 6.1), six pseudolites, and three baselines. It was demonstrated that this method will converge to the correct vehicle baseline locations when the pseudolite locations are exactly known. However, small errors in the supposed locations of the pseudolites can produce nearly proportional errors in the estimated baselines. The plot of Figure 6.2 illustrates this sensitivity. This plot was generated by running 200 simulated calibration procedures for each value of error in the assumed parameter. A simple example evidences why this approach is so sensitive to the known locations of the pseudolites. If the pseudolites are all x centimeters higher than the supposed height used in the estimation (i.e. the errors in the supposed locations are all in the same direction), then the baselines of the vehicle will be erroneously measured to be x centimeters higher than the actual baseline locations.

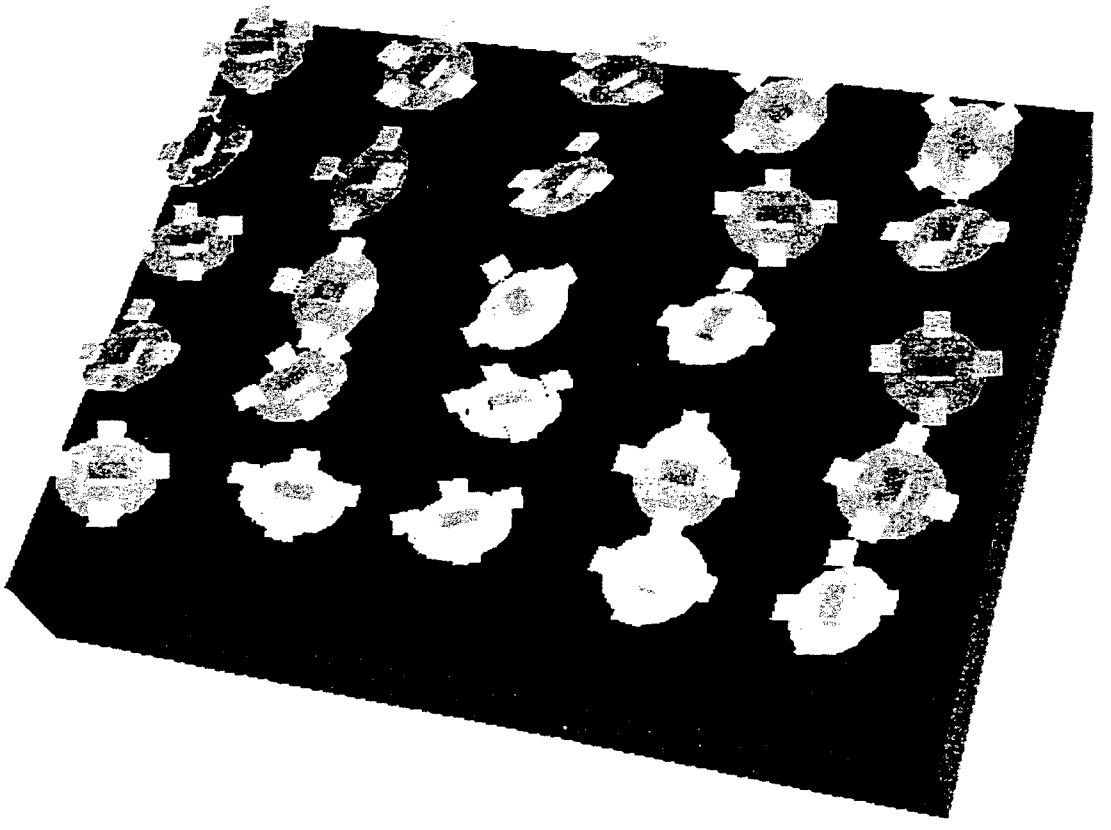

Figure 6.1: **Calibration Data Sample Space**

The calibration data sample space must span all six degrees of freedom in order to effectively calibrate the pseudolite position and baseline parameters. This three-dimensional model shows the sample locations and orientations of the target vehicle. Movement in six degrees of freedom was achieved by raising and tilting the top plate of the vehicle, upon which the receiver antennas were rigidly mounted.

Approach 2: Assume receiver antenna baselines, estimate pseudolite locations known

The second approach attempted to estimate the pseudolite locations by assuming that the antenna baselines were known reasonably well. This approach fares better against errors in the supposed antenna baseline values, as evidenced in the plot of Figure 6.2. In particular,

the maximum phase-center variation from the physical center of the antenna is likely to be less than 1 cm (see data from Figure 4.21), leading to a phase-center error of approximately 1 cm in the estimated pseudolite location. This method can still be improved upon, though, as is described in the next approach.

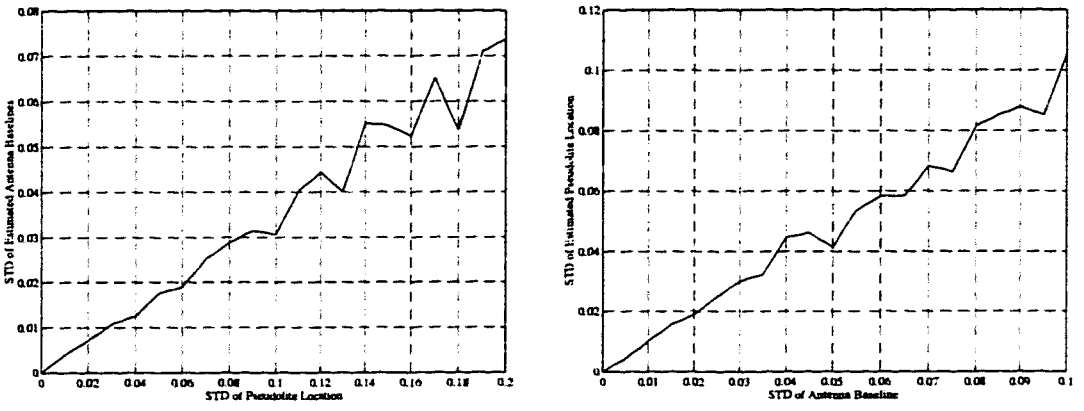

Figure 6.2: **Variation of Estimated Parameters versus Assumed Parameters**

These plots show the potential error accrued in the estimated parameters versus the assumed parameters in calibration approaches 1 and 2. Although the variation of the estimated parameters with the assumed parameters is nearly proportional for both methods, the repercussions are likely to be greater in method 1. since the error in assumed locations of the pseudolites is likely to be greater than assumed locations of the antenna baselines. Both methods are less robust to parameter variations than calibration approach 3.

Approach 3: Simultaneous estimation of receiver antenna baselines and pseudolite locations

The third approach eliminated the parameter sensitivities of the previous two approaches by simultaneously estimating the pseudolite locations and the antenna baselines. The only restriction was that more sample points needed to be taken throughout the workspace to resolve the larger number of unknowns.

Theoretical Derivation

The equations relating the unknown antenna baselines and pseudolite positions to the measured phases can be derived from the basic phase measurement equation as described below. It is assumed that there is no knowledge of B_{ij} and Q_k, and thus the integers *cannot* be backed out from the known vehicle state (P_i, R_i). Therefore, it is necessary to eliminate the integer cycle ambiguity through phase differencing over time. Starting with the intra-vehicle phase difference from equation (3.3):

$$\Delta_1\phi_{ijk} = |(P_i + R_iB_{im}) - Q_k| - |(P_i + R_iB_{ij}) - Q_k| + \lambda M_{ijk} \tag{6.1}$$

The time difference results in:

$$\begin{aligned}\delta\Delta_1\phi_{ijk}(t_1,t_2) &= |(P_i(t_2) + R_i(t_2)B_{im}) - Q_k| - |(P_i(t_2) + R_i(t_2)B_{ij}) - Q_k| - \\ &\quad |(P_i(t_1) + R_i(t_1)B_{im}) - Q_k| + |(P_i(t_1) + R_i(t_1)B_{ij}) - Q_k| \\ &= h(B_{ij}, Q_k, t_1, t_2)\end{aligned} \tag{6.2}$$

The time-intra-vehicle phase differences were then linearized about the unknown antenna baselines B_{ij} and pseudolite locations Q_k, while the vehicle position and orientation ($P_i(t)$ and $R_i(t)$) were known at every sample point. Linearization of (6.3) results in:

$$H(t_1,t_2) = \begin{bmatrix} \frac{\delta h_1()}{\delta B_{i1}} & \frac{\delta h_1()}{\delta B_{i2}} & \cdots & \frac{\delta h_1()}{\delta Q_6} \\ \frac{\delta h_2()}{\delta B_{i1}} & \ddots & & \vdots \\ \vdots & & & \\ \frac{\delta h_{30}()}{\delta B_{i1}} & \cdots & & \frac{\delta h_{30}()}{\delta Q_6} \end{bmatrix} \tag{6.3}$$

Where h_n is the n^{th} row of $h(B_{ij}, Q_k, t_1, t_2)$, the number of pseudolites was six and the number of antenna baselines was four. The linearized matrices (6.3) are stacked over time to form the observation matrix for the whole batch, while the measurements are likewise stacked over time to form the vector of all measurements for the batch:

$$H_{batch} = \begin{bmatrix} H(t_1,t_2) \\ H(t_2,t_3) \\ \vdots \\ H(t_{n-1},t_n) \end{bmatrix} \tag{6.4}$$

	nominal	rot $\pm x$	rot $\pm y$	raised z
Robot	0	9 deg	9 deg	7 cm
Target	0	9 deg	9 deg	7 cm

Table 6.1: Antenna Deflections for Three Dimensional Observability

$$Z_{batch} = \begin{bmatrix} h(B_{ij}, Q_k, t_1, t_2) \\ h(B_{ij}, Q_k, t_2, t_3) \\ \vdots \\ h(B_{ij}, Q_k, t_{n-1}, t_n) \end{bmatrix} \tag{6.5}$$

Application

This calibration scheme was employed to calibrate the system parameters for this project. A total of 192 samples were taken for each vehicle across distributed locations in the workspace and with the antennas situated in six different configurations to achieve observability in three dimensions (32 sample locations per configuration). The six antenna configurations are illustrated in Figures 6.3 and 6.3. The configurations consisted of one in-plane and five out-of-plane arrangements in which the *antennas remained fixed with respect to each other.* The amount of out-of-plane deflection for each of these configurations is summarized in Table 6.1.

It should be recognized that great care had to be taken during data sampling to ensure useful data was collected. First, the phase measurements were averaged over 30 seconds at each sample location. Then, to limit multipath effects, SNR weighting of the signals was incorporated. Finally, live data were compared with the theoretical values in real time during sampling to visually ensure that the measured data was close to the expected values. Instances in which there were gross strays (suggestive of multipath) were thrown away.

Results

The calibration results are summarized in Tables 6.2, 6.3, 6.4, and 6.5. Some measure of the accuracy of the calibration can be gained by comparing the two solutions for the pseudolite positions from the robot antenna baseline calibration and the target antenna

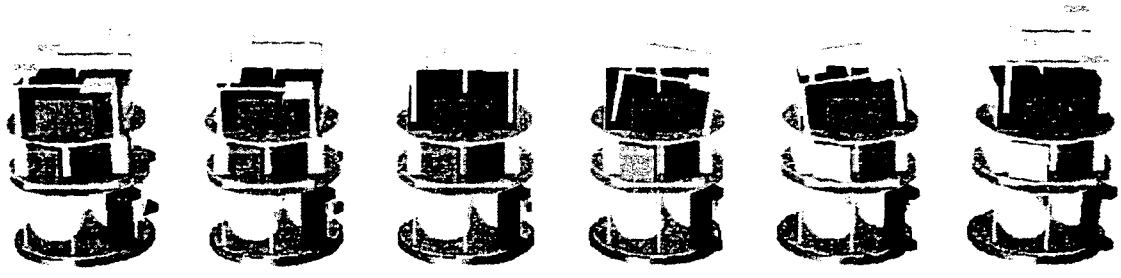

Figure 6.3: **Robot Antenna Deflections for Collecting Out-of-Plane Calibration Data**

The robot antenna frame was deflected in five out-of-plane configurations to achieve observability in three dimensions in order to solve for the baseline and pseudolite position parameters. Shown left to right are 1) nominal position, 2) positive rotation about the x-axis, 3) negative rotation about the x-axis, 4) positive rotation about the y-axis, 5) negative rotation about the y-axis, 6) raised along the z-axis. 32 samples were taken across the workspace for each configuration.

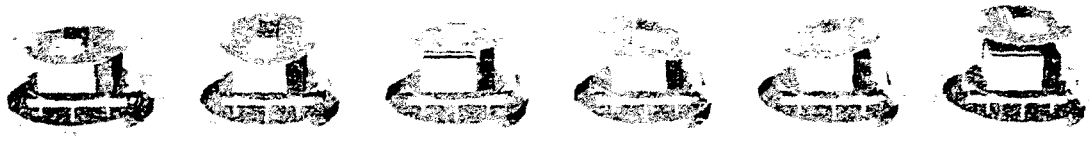

Figure 6.4: **Target Antenna Deflections for Collecting Out-of-Plane Calibration Data**

Similar to the robot, the target antenna frame was deflected in five out-of-plane configurations to achieve observability in three dimensions. Shown left to right are 1) nominal position, 2) positive rotation about the x-axis, 3) negative rotation about the x-axis, 4) positive rotation about the y-axis, 5) negative rotation about the y-axis, 6) raised along the z-axis. 32 samples were taken across the workspace for each configuration.

baseline calibration. The variance of the difference in magnitude of pseudolite position vectors from the two instances was 7.1 cm.

Possible sources of these errors (in order of suspected magnitude) are multipath, phase center variation, and phase polarization. Multipath is suspected to be the greatest contributor to calibration errors due to its dominating impact on the state estimation procedure (as noted in Chapter 4). Another indication was the visually observed behavior of the

	$B11$	$B12$	$B13$	$B14$
x	-0.131	0.149	0.138	-0.142
y	-0.206	-0.204	0.203	0.196
z	0.735	0.642	0.723	0.639

Table 6.2: Robot Antenna Baselines

	$B11$	$B12$	$B13$	$B14$
x	-0.007	0.191	0.020	-0.175
y	-0.176	0.006	0.186	-0.002
z	0.415	0.366	0.389	0.305

Table 6.3: Target Antenna Baselines

actual phase measurements compared to the predicted measurements as the vehicles were manually moved around to collect calibration data.

Phase center variation is a likely source of error for two reasons. First, the receiver antennas frequently witnessed extreme zenith angles to the pseudolites whenever the antenna set was rotated out of plane. Second, the phase-center variation of the helical transmitter antennas may be fairly significant due to their highly directional design.

Circular polarization of the GPS signal represents a small, unmodeled contribution to the phase measurement. Modeling this effect was discussed in Section 4.3.4. It was not

	$Q1$	$Q2$	$Q3$	$Q4$	$Q5$	$Q6$
x	1.16	-3.00	-0.10	-2.80	1.22	-2.84
y	3.73	3.18	-0.23	-3.85	-4.00	0.01
z	1.85	2.02	2.25	2.22	1.87	2.23

Table 6.4: Pseudolite Positions (Computed with Robot Antenna Baselines)

	$Q1$	$Q2$	$Q3$	$Q4$	$Q5$	$Q6$
x	1.20	-2.99	0.00	-2.84	1.16	-2.91
y	3.73	3.17	-0.28	-3.80	-4.09	-0.03
z	2.23	2.07	2.35	2.01	2.05	2.16

Table 6.5: Pseudolite Positions (Computed with Target Antenna Baselines)

included in this calibration scheme due to the added complexity versus the marginal gain in accuracy. As can be seen from Figure 4.23, the contribution of this effect is not very significant over the distance of the intra-vehicle phase difference.

The impact of the parametric error on the state estimation process was analyzed in the same manner as the bias error sources were in Section 4.3.4, that is, Monte-Carlo simulations were run for 200 cases with typical parametric error values. The results are shown histogramatically in Figure 6.5. The corresponding one-σ errors were 3.0 cm in absolute position, 1.1 cm in differential position, 0.19 deg in absolute orientation, and 0.09 deg in differential orientation.

Other Suggested Calibration Approaches

The calibration approach used in this project worked reasonably well, but could be improved. In particular, this approach was rather sensitive to bias errors due to the short baselines between antennas on each of the vehicles – a given bias error will be a larger percentage of the measurement for a short baseline versus a long one. Two ideas are presented as possible ways to calibrate with longer baselines between receiver antennas.

Long Baseline Using Two Vehicles

There are a couple ways in which two vehicles could be used simultaneously for calibration. The calibration scheme could be modified to include the double-difference inter-vehicle phases. The calibration process would then require simultaneous estimation of all the baselines for both vehicles along with the pseudolite positions.

Although this would provide longer baselines between antennas, this method has two disadvantages. First, it would require the double-differenced phases to be differenced once more over time as a triple difference. This is undesirable, as it would amplify bias errors. Second, the process of moving both vehicles around on the table would make the data collection process all the more tedious.

Another idea for achieving longer baselines without the above drawbacks is to use one vehicle as a fixed reference with a direct connection to the receiver of the vehicle being calibrated in order to circumvent the need for double differences between receivers. Using this method, the master antenna input on the receiver of one vehicle would be connected to the master antenna of the other vehicle via a long cable. Samples would be taken for

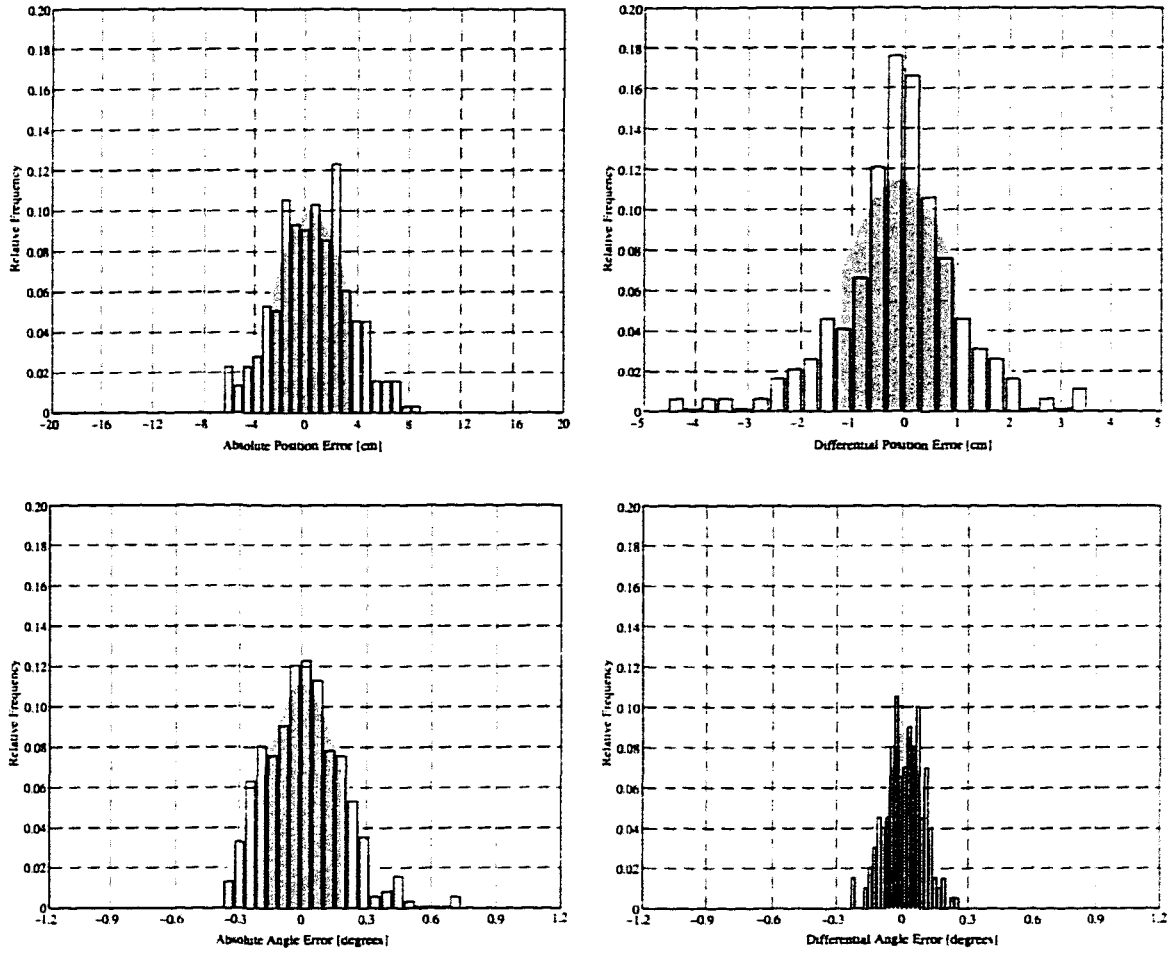

Figure 6.5: **Likelihood of Error Due to Calibration Error**

These plots show the relative likelihood of position and orientation errors of given magnitudes to occur due to calibration errors in the pseudolite positions and vehicle antenna baselines. The standard deviations for these errors are summarized in Table 4.4. The one-σ band of each of these probability mass functions is delineated by the dark gray region.

distributed locations and antenna deflections of the calibration vehicle.

X-Y Table

Accurate calibration of the pseudolite positions could be performed independent of the

vehicle baselines with an X-Y table as shown in Figure 6.6. This type of system would eliminate the sensitivities exhibited by calibration approach 2, since the measurements would take place over longer baselines. This type of mechanism could be equipped with actuators and encoders to automate the data taking process and eliminate the need for an overhead vision system to measure the location of the antennas in the workspace. Perhaps an even more useful application of this type of system would be to accurately map the phase pattern over the entire workspace volume.

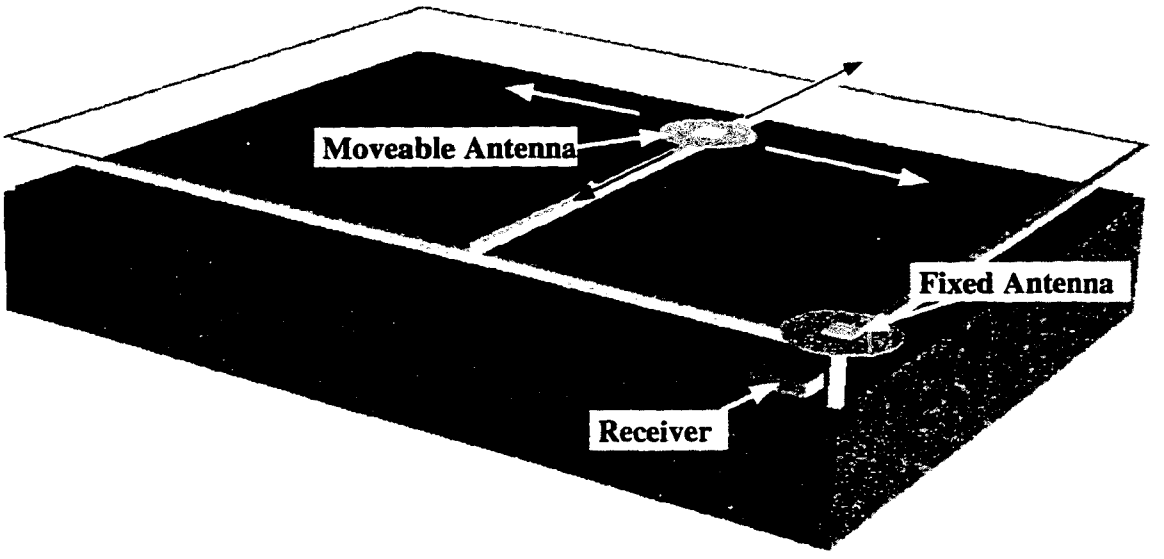

Figure 6.6: **X-Y Table Calibration Mechanism**

An X-Y table could help automate the data-taking process for calibration, as well as permit mapping of the phase patterns of each pseudolite over the entire workspace.

6.1.1 Line Bias Calibration

The line biases are differences in signal-path lengths from the antennas to the sampling point inside the receiver. By including line biases in the measurement equation (3.2), it can easily be shown that only the intra-vehicle phase differences (3.3) are affected by these biases. Additionally, only the difference in line biases between the master antenna and each of the slave antennas needs to be known.

With this in mind, a simple method for measuring the line bias differences was arranged as shown in Figure 6.7. In this scheme, the input of a signal splitter was connected directly to

a pseudolite. one splitter output was connected to the master antenna input of the receiver and the other was connect to one of the slave antenna cables. Single-difference phase measurements were collected for one minute. and then the a second set of measurements was taken with the splitter outputs switched. Switching the splitter outputs eliminated any path-length differences inside the splitter devices itself. Both sets of measurements were averaged to produce the line-bias difference between the master and slave antenna. This approach assumes that the path lengths within the receiver antennas themselves are the same, which is a reasonable assumption in comparison with other sources of bias error within the system. Calibration of line biases between vehicles is unnecessary, as the line-bias terms simply cancel out of the the inter-vehicle second-difference equations.

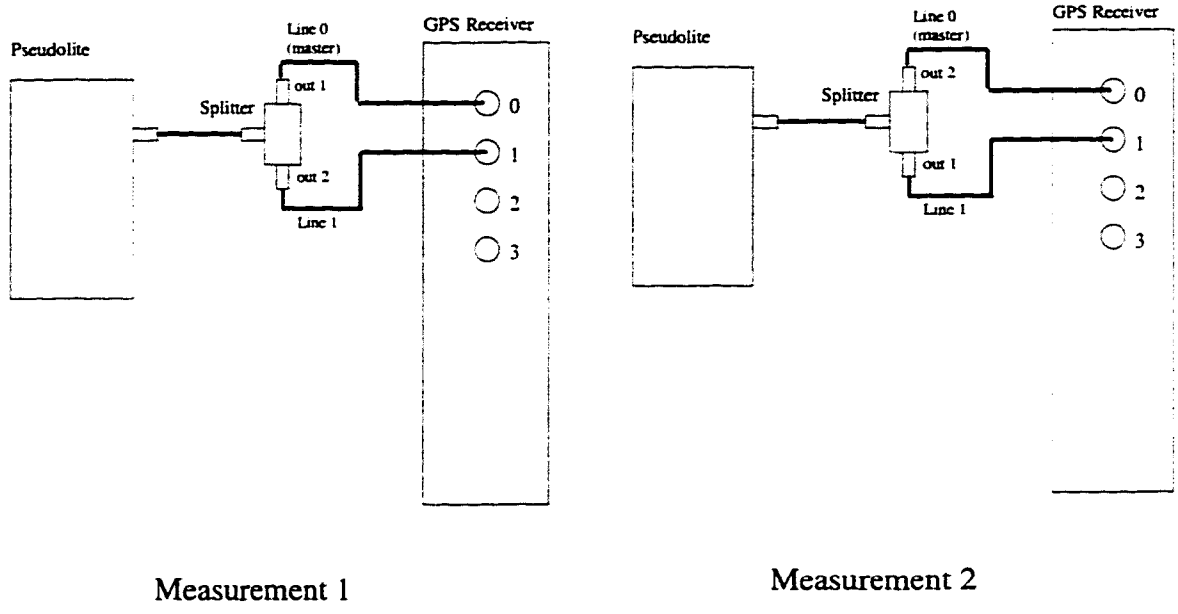

Measurement 1 Measurement 2

Figure 6.7: **Line Bias Calibration Scheme**

Chapter 7

Conclusions

This chapter presents a summary of the main achievements of this thesis and then extends these to ideas for future directions. Some practical issues are first addressed, including what needs to be done to bring this technology to operational systems and how system reliability and performance may be improved. Second, the author presents thoughts on applying the "Systems Engineering Design Philosophy," a strongly held tenet of the Stanford Aerospace Robotics Lab, to modular open-architecture GPS receivers. Finally, some musings on future GPS systems that may evolve from current technologies are presented.

7.1 Summary and Conclusions

The goal of this thesis was to develop a means for sensing robotic vehicles in three dimensions in space. The system requirements for operational space robot systems were presupposed to exist in exemplary tasks, including autonomous rendezvous and formation flying, carried out on a laboratory prototype system. These tasks were performed by using GPS in an entirely new way in a well-controlled indoor laboratory environment. This new approach to using GPS could serve as a basis for augmenting NAVSTAR GPS for operational space systems such as the International Space Station. This approach also introduces the possibility of using GPS in unprecedented application areas such as automated manufacturing.

The contributions of this thesis were discussed in Section 1.5. The contributions are summarized pictorially below. At the highest level, this thesis defined a new GPS-like positioning system designed to work indoors. Theoretical and technical distinctions between the two systems were made. Many of the differences were due to the differences in proximity

of the transmitters to the receivers, and thus the two systems were referred to as far- and near-constellation GPS. The near-constellation positioning system was employed to experimentally demonstrate autonomous rendezvous between two prototype space vehicles. The capabilities afforded by the near-constellation system indicate that pseudolite-augmentation of the NAVSTAR GPS could greatly benefit operational space vehicles, particularly in situatations in which multiple vehicles need to interact.

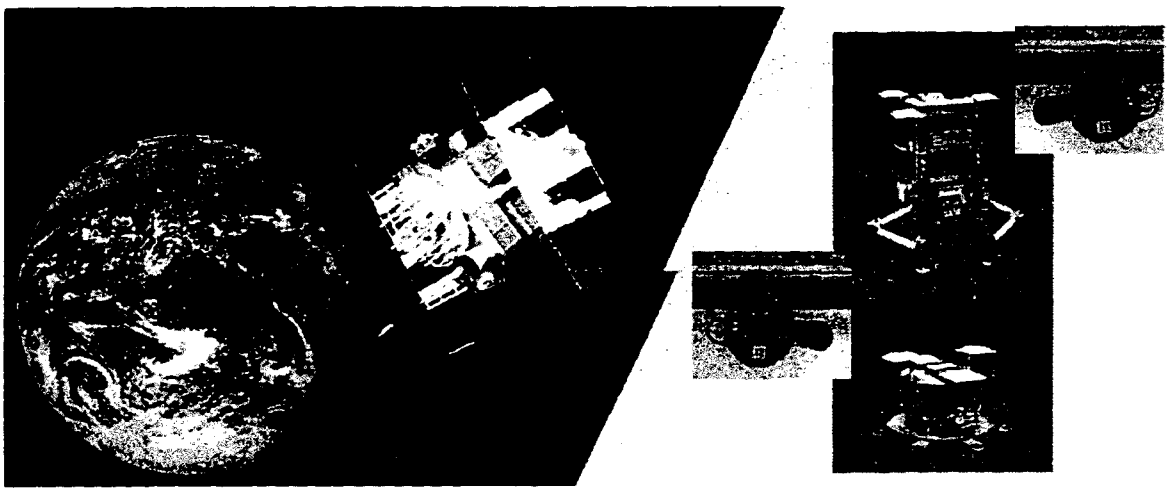

Figure 7.1: **Fundamental Understanding of Distinction Between Far- and Near-Constellation GPS**

The diagram of Figure 7.3 shows the connectivity between the research issues raised by the objectives of this thesis versus the specific contributions. These are summarized as follows:

Spherical Wavefront - The close proximity of the transmitters to the receivers nullified the planar wavefront assumption usually made for a far-constellation system. This was addressed by forming a new non-linear mapping of carrier phases to vehicle states. This mapping approaches those used for far-constellation systems in the limit as the pseudolite locations are moved to infinity.

No Pseudo-range - Attainable pseudo-range accuracies were not sufficient to provide useful information at the scale of the experiment, so they were not used. The lack of information was addressed by the new theoretical model, which incorporated carrier-phase measurements only. This also affected how the GPS measurements were integrated with

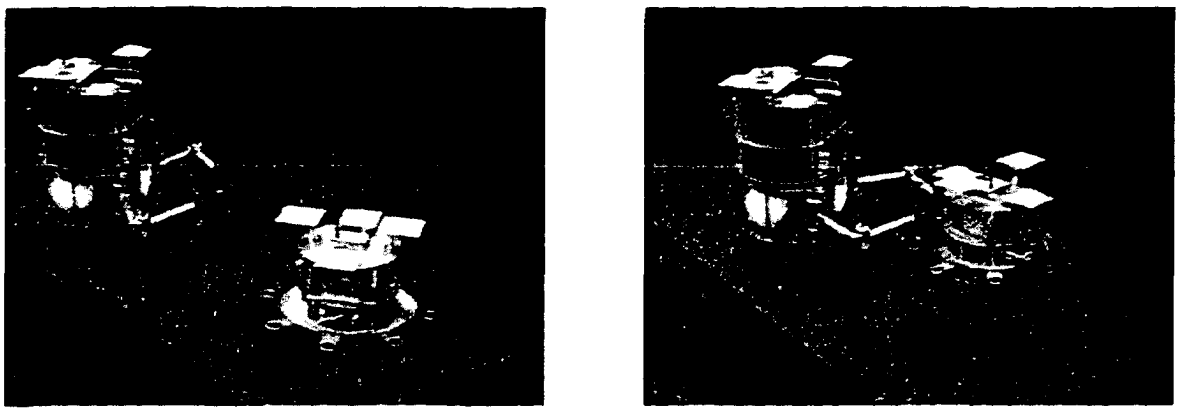

Figure 7.2: **First Experimental Demonstration of Autonomous Rendezvous Using GPS as the Only Sensor**

the real-time controller, and the method used to synchronize independent receivers. Since the pseudolites were hand-mounted above the perimeter of the workspace, new calibration techniques had to be devised to determine their locations, as well as the baselines of the receiver antennas.

Asynchronous Transmitters - In the interest of low cost and simplicity, the pseudolites were not synchronized. This was addressed in the theoretical model which used double-differenced phase measurements and a new time-bias computation algorithm to eliminate the transmitter time errors. One specific pseudolite was designed to broadcast the 50 bits/sec GPS data message and was designated as the "true-time" reference. The receiver's firmware algorithms were then modified so they would synchronize with the master pseudolite's signal.

Near-Far Problem - This issue was addressed by the helical antenna design, which permitted empirical adjustment of the beam width until the receivers maintained lock over the majority of the workspace. It was also suggested that pulsed pseudolites could be used to alleviate the near-far problem.

High Multipath Environment - The helical antenna design also helped alleviate multipath by reducing the amount of the signal reflected from walls. In addition, a method was presented for mitigating multipath effects by limiting the amount a measured signal could vary from that anticipated by a model-based predicted value.

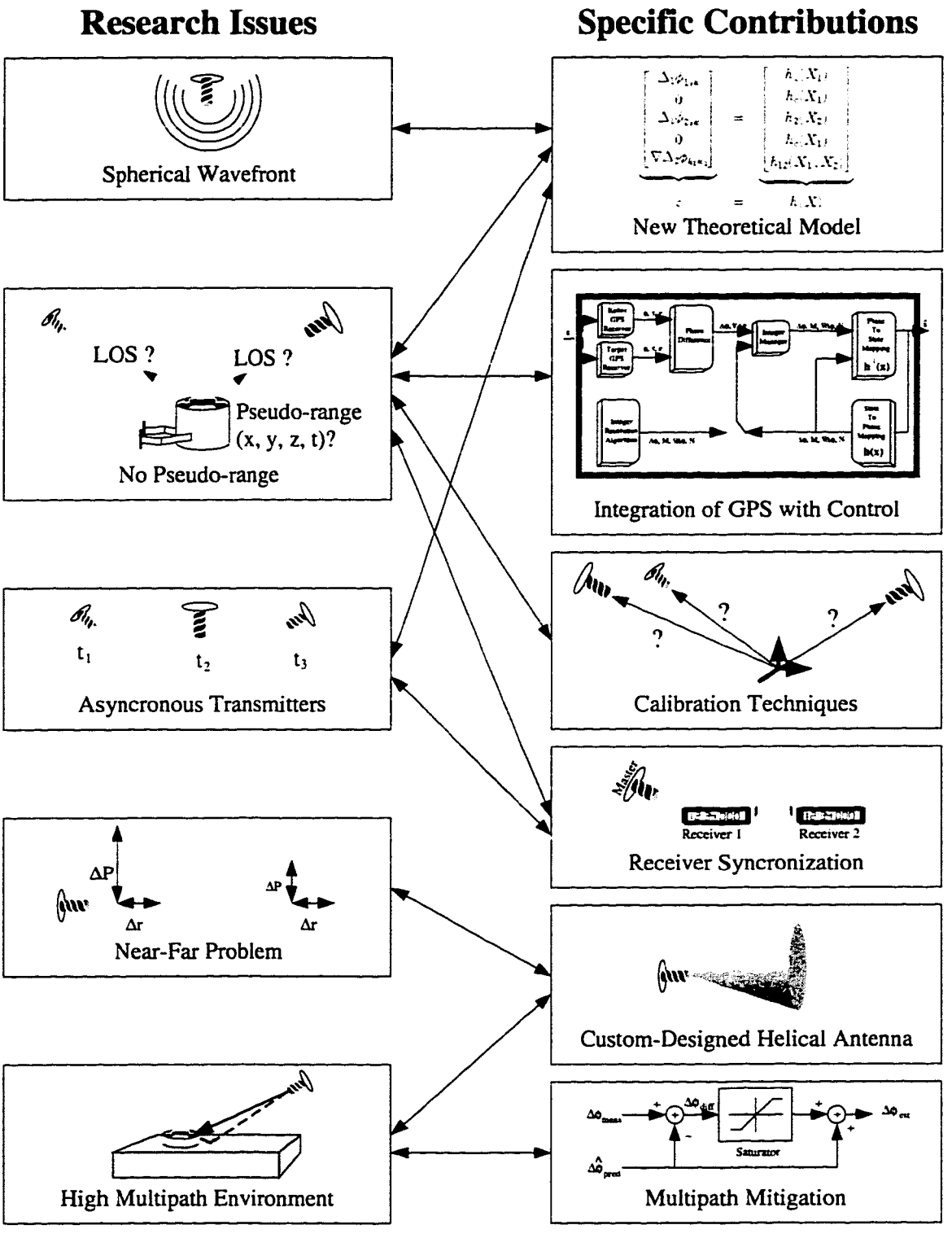

Figure 7.3: **Connectivity Between Research Issues and Thesis Contributions**

7.2 Future Research

As is often the case with basic research, this thesis project has raised a number of new ideas and issues that were completely unanticipated at the onset of the work. Two areas to be particularly fertile for future research: the use of GPS for indoor systems, and the use of GPS for real-time control. Throughout the duration of this research the author has received dozens of inquiries regarding the applicability of GPS to robotic systems, ranging from automated harvesters to hazardous waste remediation robots. Some of these systems are to operate indoors while others are to work within well-defined boundaries outdoors. In either case, pseudolite-only or pseudolite-augmented GPS sensing could be applied, although each application would require a custom-designed system. This section presents ideas on how GPS-like systems could be specifically tailored to indoor applications and also presents considerations on how GPS could be made more readily available to the rapidly growing community of engineers interested in using GPS for real-time control of autonomous vehicles.

7.2.1 Indoor GPS Systems

Fundamental Improvements to GPS Sensing

This thesis presented the first working indoor GPS-based sensing system, and as such several areas were identified for improving this baseline system. Chapter 4 presented analyses of stochastic-noise and bias error sources. Each of these analyses concluded with suggestions for reducing the errors incurred by each source. Chapter 6 discussed calibration methods, and a new one that is less sensitive to measurement noise was discussed. This new method could be implemented to better calibrate the system. Chapter 5 showed in simulation a method for initializing the system using only GPS measurements. This or a similar technique could be implemented to remove the dependence on the overhead vision system for initialization. These suggestions, along with a few others, are prioritized below according to which might have the greatest benefit to the overall system.

1. *Reduce multipath* – Strong evidence suggests that multipath is the largest error source in the system. Several methods for addressing this were suggested in Chapter 4. It would also be useful to conceive of a more rigorous way to quantitatively measure the multipath effects.

2. *Reduce antenna pattern effects* - This includes incorporating polarization and phase center variation effects in the implemented model. Closer analysis of antenna near-field pattern effects would be useful, and could potentially become a thesis topic for an electrical engineering student concentrating in electromagnetics and high-frequency design – an area somewhat outside the robotics and controls expertise in ARL.

3. *Implement Motion-Based Initialization* - This would demonstrate complete independence of the GPS sensor.

4. *Attempt to Incorporate Pseudorange* - Use of pseudo-range could substantially improve the robustness of the overall system, but would require significant modification to the current system. First, the receivers would have to be upgraded to a more capable design capable of resolving pseudorange down to less than a meter. Such a receiver would require features including a higher *internal* sampling rate, higher resolution correlators, and perhaps more channels[1]. Second, the pseudolites would have to be synchronized. This could potentially be achieved by connecting all of the transmitters to one common oscillator. Care would have to be taken to account for transmission delays, impedance matching, signal loss along the line, and noise isolation. Finally, the measurement algorithms (and implementation) would have to be modified to include the pseudo-range measurements.

5. *Use Pulsed Pseudolites* - The use of *pulsed* pseudolites [10] could potentially eliminate the near-far problem, and hence reduce the frequency of integer hand-off incurred by pseudolite signal loss/gain.

6. Implement New Calibration Method – More accurate calibration of the pseudolite positions and the receiver antenna baselines could result in a noticeable improvement in the absolute position measurements.

Indoor-Specific Sensing Systems

There is no fundamental reason why an indoor GPS-like system need be constrained to GPS frequencies. In fact, frequencies in the electromagnetic spectrum could be used with fewer regulations in an enclosed building than in an open environment. A multi-frequency system might consist of a radio-wave frequency component, a microwave frequency component

[1]Trimble Navigation's latest 12-channel *Force* receiver may meet these needs, but at a cost

(GPS), and a light-wave component. The lowest frequency would be used to maintain lock when the other signals are blocked by physical structures in the environment. The intermediary frequency would be used to resolve positions to the several-centimeter level, while the light-wave component could improve the accuracy to the sub-millimeter level. Such a system would differ from light-wave-only systems in that it would operate *homogeneously* throughout the workspace, in comparison with laser-based systems which operate only in very-specific workspace locations.

Another possibility is to use a dedicated frequency for each transmitter (FDMA - Frequency Division Multiple Access), rather than using spread-spectrum techniques (CDMA - Code Division Multiple Access) [2]. This will effectively eliminate the near-far problem associated with spread-spectrum techniques, and thus increase the size of the usable workspace.

7.2.2 GPS for Real-Time Control

There are two large and predominantly disparate communities that are just starting to merge technologies – the GPS community and the real-time automated systems community. The former has great experience in radio-frequency design and application-specific embedded control, while the latter is more experienced with complex multi-sensor autonomous real-time apparatus, such as robotics. Each of these can greatly benefit from the other. Bringing the two together will enable systems with unprecedented capabilities, including autonomous spacecraft, aircraft, automobiles, and mining and harvesting equipment.

It is not possible for the GPS equipment manufacturers to conceive of all the possible applications of this technology – the real-time automated systems community is the end-user, and will drive the product requirements. GPS equipment manufacturers will have to either be extremely flexible and capable of customizing products to suit diverse applications, or choose very specific market niches.

It is suggested here that GPS equipment manufacturers could support a very broad market with a modular open-architecture receiver. Such a receiver would largely be used within the research community and would allow users to tailor the functionality to their needs at any level. In turn, the new capabilities developed by the research community could be refined and incorporated into new products by the GPS equipment manufacturers.

[2] GLONASS, the Russian equivalent of GPS, is an FDMA system wherein each satellite transmits on its own dedicated frequency.

To date, the GPS receiver has primarily been developed as a stand-alone peripheral device. In contrast, new applications require close coupling between the GPS receiver and other components in the system, including the control computer and other sensors. An open-architecture receiver will permit the real-time automated systems developers to obtain information at any level from the GPS receiver, down to the raw measurables of the GPS signal. A modular, open-architecture would not only make it easier for outside users to integrate their custom systems, it would also simplify the manufacturer's internal maintenance and development.

The terms "modular" and "open-architecture" are popular buzz words in the engineering community, so the following sections are provided to clarify what is meant by these terms.

Modular Open-Architecture Receiver

The modular open-architecture receiver is comprised of a computer running a real-time operating system, a single-board GPS module (or set of modules) that plugs into the computer's expansion ports, and software to control the GPS hardware and interface to the user's application. The user's application may reside on the same processor as the GPS receiver software, or it could reside on a separate computer and communicate via direct memory access to the processor running the GPS code, depending on the processing requirements of the application. Receivers designed along these lines are just starting to gain attention in the GPS community [49], [44].

Modular Hardware

The basic building block of the GPS receiver is a single channel consisting of an RF front-end and a signal correlator that can track a single satellite. The user adds channels (or blocks of channels) by merely plugging hardware modules into standard computer expansion ports (such as PCI, S-BUS, or VME). This could be likened to adding more memory to one's computer by adding Serial In-line Memory Modules (SIMMS). Typical applications currently use only six channels. It is not unrealistic for future applications to require a hundred channels or more[3]. Modules should be capable of synchronous operation via a

[3]As an example, imagine a system that must track full ranges of motion in three-dimensions in space. This would likely require a minimum of eight antennas distributed around a spacecraft, times twelve channels per antenna (without antenna multiplexing channels), which totals 96 channels.

common oscillator and antenna input lines should be readily shared between modules.

Modular Software

The dominant issue for real-time autonomous systems (such as autonomous mobile robots) is software complexity management. The software on these systems must typically integrate several diverse sensors, actuators, and control algorithms. As a result, the industry has produced modular software architectures for managing these complexities [38]. High-end GPS receivers have reached the level of sophistication that they should be developed in a similar manner to these real-time autonomous systems.

Modularization of GPS receiver software requires thoughtful separation of the functionality of different levels of code, with clean and concise interfaces between each. For example, signal processing should be clearly separated from higher-level navigation code, and data-communication code (to external devices) should likewise be separate.

Use of industry standards and commercial products will lead to well-designed, modular software. Therefore, industry standards and commercial products should be used as much as possible. The receiver code should be built upon a flexible, efficient, and capable commercial real-time operating system and programmed in a high-level language. Using a standard real-time operating system and programming in a high-level language has several advantages over using in-house real-time operating systems and coding in assembly language:

- High-level code and commercial operating systems will remove dependency on any particular type of microprocessor. Upgrades to newer, more capable processors will be trivial. A greater customer base can be supported as well. For example, with the number of emerging space applications, the ability to port GPS receiver software to radiation-hardened space-qualified processors will be critical. Well-designed software should require little more than re-compilation for the new processor.

- A standard real-time operating system will enable deterministic sample rates, rather than polled or "as computed" results. This is a necessary feature of any sensor used in discrete-time control.

- Engineers within the GPS product development group will have a greater understanding of the whole product (beyond their individual area of contribution), since it will be easier to read and understand other engineers' code.

- Members of the engineering community as a whole are more likely to be familiar with commercial operating systems and high-level programming languages. Use of these standards will reduce the learning curve for new employees who must maintain and build upon products they did not originally design.

These recommendations are not without counter arguments. It may be claimed that code based on a high-level language will be slow. This claim is generally unfounded given today's compilers which can optimize code – sometimes better than a hand-coded assembly language program. This is especially true for RISC architectures which do not lend themselves well to hand-coded assembly language.

Use of a commercial operating system will incur the cost of royalty fees on each product sold; however, this should be weighed against the cost of design, maintenance, and upgradability of an in-house real-time operating system. There has traditionally been concern about the kernel size of a full-blown commercial real-time operating system; however, the leading commercial real-time operating systems can currently be tailored to a minimum kernel size for embedded controllers.

The stated benefits address the issue of complexity management. Hardware is inexpensive and growing ever more capable and cheaper. The greater cost exists in constant engineering re-design due to system complexity.

Open Architecture

The purpose of an open architecture is to offer the user complete flexibility in use of the product. The user has access to all interfaces and the relevant portions of the source code. In this way, the customer can tailor existing code to his or her particular application.

For example, suppose an aerospace company wanted to purchase a commercial GPS receiver for use in satellite navigation. The receiver, perhaps designed for land use, would perform better if algorithms such as GPS satellite searching strategies were modified for conditions on orbit. With an open-architecture receiver, the aerospace company could use its own in-house experience to modify the code as necessary. These modifications could in turn be re-sold to the GPS receiver manufacturer and introduced as a new product. With a closed-architecture receiver, the GPS receiver manufacturer would have to dedicate its own workforce, not necessarily experienced in the area of interest, to make the necessary modifications.

The idea of openly distributing proprietary technologies, in particular software, is counterintuitive in the realm of traditional business strategy, but has been demonstrated as a powerful strategy in not-so-traditional high-tech markets. Companies that have successfully adopted open-architecture schemes include Mathworks (MatLab numeric computation and visualization software) and Sun Microsystems (SPARC workstation and Network File System) [28]. The essential feature of an open architecture is that it enables a company to virtually "employ" the entire community of customers using its product.

A Modular Open-Architecture Receiver Designed Using ControlShell

One approach toward modularizing receiver code would be to use commercially available Computer Aided Software Engineering (CASE) tools[4]. The diagrams shown in Figures 7.4 and 7.5 provide an example of how a GPS receiver could be designed using *ControllShell*. Using this tool, the engineer *graphically* designs system software. Each block in the diagram represents a "C++" software component (an instance of a "C++" class), and the connecting lines are signals communicated between each module. The components shown in these diagrams actually perform the lowest level functions of a real GPS receiver – establishing code and carrier lock for a single channel.

The first diagram is a finite-state machine which manages the mode of the feedback control loop for locking on to the signal. The second diagram *is* the feedback control loop. The goal of the process is to simultaneously track the C/A code and carrier phase. The progression of the control modes is visually apparent from the state diagram. The process begins in an open search mode in which the receiver searches in broad sweeps over the space of carrier frequency versus C/A code phase until it finds a significant correlation. At this point the state transitions to a new mode of control (Find_Corr_Peak) to find the peak of the correlation by fine-adjusting the code phase at a fixed frequency. Once this process finds the code phase that produces a maximum correlation value, it transitions to yet another mode of control in which the internally-generated carrier frequency is fine-tuned to match the frequency of the incoming signal (Auto_Freq_Control). A final mode of control is then entered to simultaneously maintain lock on the code and carrier phase. The state diagram also shows how the system reverts back to the coarse modes of control whenever tracking is

[4]Examples include Real-Time Innovation's *ControlShell*, MathWork's *Simulink*, Integrated Systems' *System Build* and National Instrument's *LabView*(R)

lost. The entire control loop is executed on the order of 1 kHz and is trigger by the epoch interrupt for the given channel.

The feedback control loop shown in the second diagram collects raw measurements from the hardware module via a device driver component. These measurements are then passed through one of four control algorithms, depending on the state of the system. The updated command signal for both the code phase and carrier frequency are then fed back to the hardware device driver component. Higher-level code may generate signals such as Doppler measurements (feed-forward carrier frequency and feed-forward code phase) to assist the control algorithms. The entire control loop is executed at 1 kHz and is triggered by the epoch interrupt for this particular channel.

This approach to software design addresses the issue of complexity management, with advantages that include:

- *The diagram is the code* – The software design is explicit and easy to understand at a glance. Greater detail can be obtained by looking inside any particular component to view its implementation algorithm.

- *The design is self documenting* – Any changes to the design immediately show up in the diagram, and therefore little or no additional effort needs to be dedicated to documentation.

- *Implementation can be changed without modification of interfaces* – The algorithms inside components can be modified without changing overall interface. For example, if an engineer designed a new algorithm for searching over the C/A code phase/carrier-frequency space, the algorithm could be incorporated by merely updating the code within the Open_Freq_Search component, without affecting the overall appearance or function of the rest of the design. As another example, if the physical hardware module were to change (perhaps another vendor's hardware were to be used), the code could be updated by merely replacing the Hardware_Module_Device_Driver component with a new one that handles the new hardware, again without affecting the rest of the design.

- *Ease of adding more channels* – The diagram can merely be duplicated to add more channels to the overall system.

- *Hierarchical separation of software is easily attained* – Higher-level software, such as navigation algorithms, can easily build upon lower-levels by creating new software diagrams. Additionally, process timing is maintained by the underlying real-time operating system.

This basic building-block design has been developed and run in simulation by artificially generating the measurements that the Hardware_Module_Device_Driver would normally produce. Addition of a real hardware module and higher-level navigation code could more thoroughly prove this design concept.

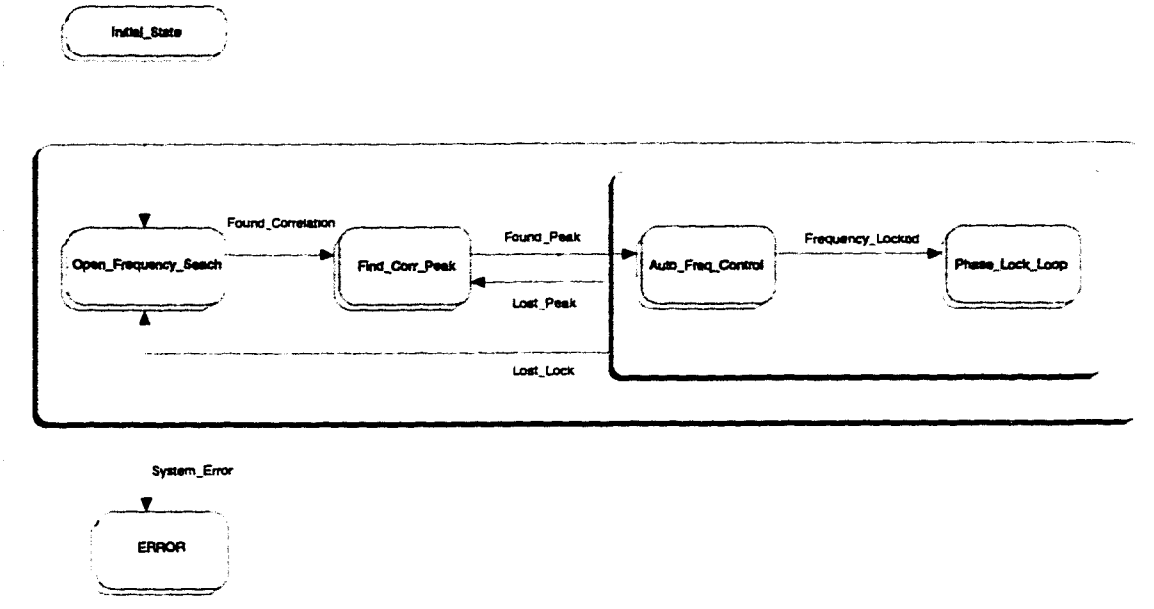

Figure 7.4: **Single-Channel Code- and Phase-Lock State Diagram**

This finite state machine controls the signal processing feedback loop for locking on to C/A code and carrier phase. Transitions from one state to another change the mode of control in the feedback control loop. Transitions are induced whenever a particular mode of control achieves its goal. For instance, the mode of control switches from Find_Correlation_Peak to Automatic_Frequency_Control whenever a correlation peak is detected.

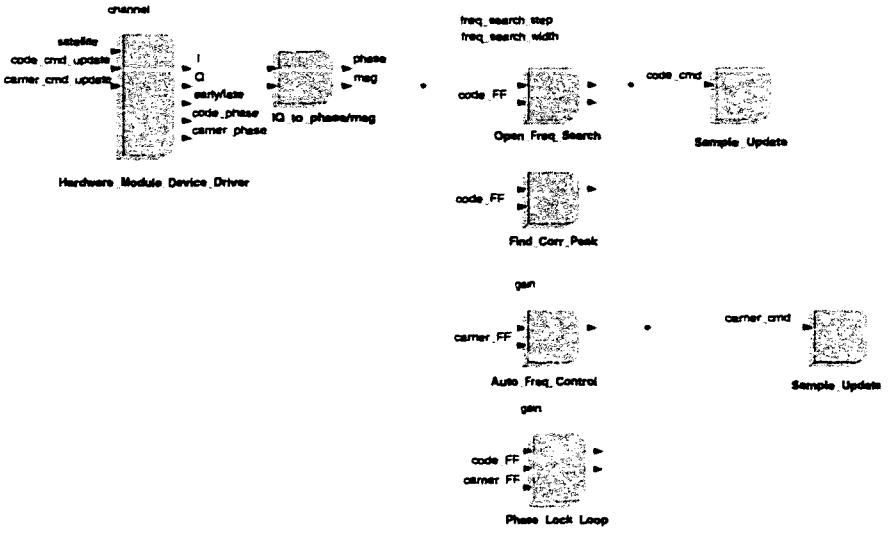

Figure 7.5: **Single-Channel Code- and Phase-Lock Control Loop**

This control loop diagram shows the flow of data through the system, from the measurement at the hardware module (via the Hardware_Module_Device_Driver), through the control algorithms, then fed back as command signals to the hardware module. The various modes of control are switched by the finite state machine shown in the previous diagram.

Integration of GPS Receiver with Control Algorithms

The open-architecture receiver design would permit tighter coupling between system control algorithms and the physical hardware, since both the receiver software and the control-algorithm software could reside on the same processor. This will not only enable the control algorithms to interact directly with the raw measurables, but will also reduce communication delays between the controller and the sensor.

One example of how this tighter coupling could be advantageous is in the direct feed-forward of the controller's acceleration commands to the GPS receiver's phase estimator. For instance, the controller knows when it is turning on an actuator, such as a thruster, and the effect of this on the physical plant can be predicted by the plant dynamics. The predicted effect can then be mapped to a corresponding expected phase velocity and acceleration. This

can then be fed-forward into the receiver's phase lock loop to maintain seamless phase lock, even when the controller's commanded accelerations are very large.

Integration of GPS Receiver with Other Sensors

GPS offers a new approach to sensing quantities that have traditionally been measured with other instruments, such as accelerometers, compasses, lasers, and even cameras, to name a few. GPS sensors can augment these sensors to form a more robust system. Again, an open-architecture receiver design would permit direct integration of these instruments with the receiver's phase-lock control loops.

Accelerometers, rate gyros and compasses could be used to maintain navigation for periods of signal block-out due to satellite occlusion. Montgomery [27] has demonstrated the ability to seamlessly re-gain GPS signal lock after a short period of occlusion by using rate gyros to compute solutions through the block-out period.

Other instruments such as laser interferometers and cameras could be used for fine-resolution control after GPS has situated the instruments into positions that are within their useful range. For example, after the main experimental objectives of this thesis were completed, the robot vehicle was retrofitted with a local camera that could sense both the robot's manipulator endpoints and the target vehicle. Since the camera is located on-board the vehicle, it cannot sense the target until the target is within less than half a meter in range. It was relatively straight-forward to demonstrate a combined GPS-receiver/local-camera sensing system in which the GPS sensor was used as a macro sensor to measure relative locations until the target was within range of the local camera. The local camera was then used to perform the final grasping of the target. This combined sensing system proved to have a capture success rate of nearly 100%, which was more reliable than the GPS-only system initially demonstrated. Additionally, the configuration of these sensors is very realistic for an operational space vehicle, as GPS could be used as a macro sensor for navigation, while a local camera could be used for fine manipulation of objects in the immediate vicinity of the robot.

7.3 Space Flight System Considerations

Applications of GPS to the International Space Station

The idea of using a near-constellation positioning system to supplement NAVSTAR GPS for navigation around the International Space Station was briefly discussed in the introduction. The concept is to place pseudolites in various locations around the station to aid vehicle navigation around the structure, as shown in Figure 7.6. The reasons for augmenting the NAVSTAR system are threefold.

- It will increase the number of measurements that a GPS-guided vehicle can use to determine its position relative to the station, especially in cases in which the NAVSTAR satellites are occluded by the space-station structure itself.
- It will enable the station to serve as a differential reference station. The pseudolite beacons on the station could combine the functions of a receiver and a transmitter, as initially demonstrated by Cobb [10], and thus directly provide differential measurements with respect to the station.
- It will provide much better geometric resolution for use of differential carrier phase measurements. That is, a set of local transmitters will make it possible to use differential carrier phase measurements for centimeter-level positioning by enabling initialization of integer cycle ambiguities as the vehicle moves around the station.

Although the physical configuration is different, the concepts are very similar to those being pursued by the Federal Aviation Administration for landing aircraft using a Local Area Augmented System (LAAS). The goal of LAAS is to augment NAVSTAR GPS with ground-based *pseudolite integrity beacons* in order to enable FAA category III landings[5]. With such a system in place, the shuttle could be "automatically landed" (docked) to the station, as could autonomous supply and maintenance vehicles. Issues such as the near-far problem could be resolved with pulsed pseudolites, as described in [10].

[5]FAA category III requirements are the most stringent, and require knowledge of the aircraft's position to less than a third of a meter.

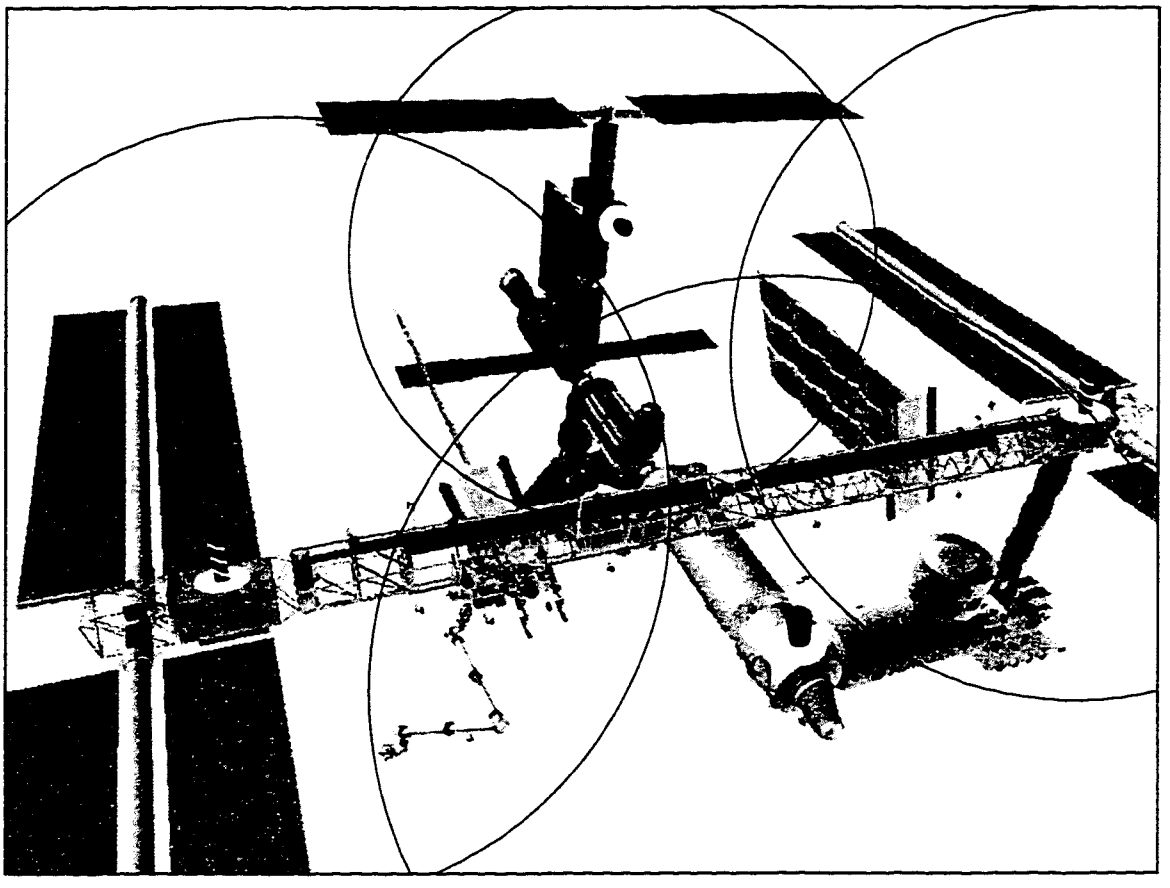

Figure 7.6: **The International Space Station Outfitted with a Near-Constellation Positioning System**

This diagram shows how pseudolites might be added to the International Space Station to augment the NAVSTAR GPS. The addition of such a system could greatly improve the accuracy and robustness of GPS-guided vehicles in the vicinity of the station. The spheres show the effective wave front emanating from each of the pseudolites. Pulsed pseudolites might be used to extend the useful range of each pseudolite signal to well beyond the size of the station structure. Original photo courtesy NASA

LEO Rendezvous

The experiments demonstrated in this thesis used pseudolites exclusive of NAVSTAR GPS satellites. A comparable rendezvous procedure in space would be performed with NAVSTAR satellites exclusive of pseudolites, *unless* one of the vehicles carried its own pseudolite transmitter (or transmitters). The motivation for this is that it is extremely unlikely one

could resolve the cycle ambiguities between the two vehicles without an additional local signal to provide observability of the relative motion between the two vehicles. The concept of outfitting vehicles with transmitters as well as receivers has much potential and is discussed further in the following section.

Multi-vehicle Spacecraft Formations

Multiple space vehicles flying in a controlled formation can perform spatially-distributed science missions without the need for interconnected spacecraft. With kilometer-length baselines between vehicles these spacecraft could collectively form a telescope capable of detecting planets in solar systems beyond our own. A self-contained GPS system would maintain formation of the spacecraft to a few centimeters, while a laser metrology system would maintain precise alignment of the telescope's optical components down to a few nanometers. The spacecraft would use these precisely aligned optical components to interferometrically resolve the collected light from distant objects. A system similar to this has been proposed by Blackwood and Colavita [3] and is currently under investigation within the NASA New Millennium Program. Figure 7.7 shows a conceptual photo of a multi-vehicle cluster in deep space.

The means for sensing and aligning the formation would vary depending on whether the vehicles are in earth orbit where other spacecraft could aid the navigation, or in deep space where the spacecraft would have to maintain formation autonomously. In either case, GPS and/or GPS-derivative technologies could be employed to sense the relative positions of the spacecraft with respect to one another. Other sensors such as star-trackers could be incorporated to provide absolute attitude information, but GPS would still be necessary for relative positioning. The following discussion focuses on the situation in which no NAVSTAR GPS satellites are in range of the vehicle cluster. Some requirements of the GPS sensor include:

- Each vehicle must be able to transmit and receive GPS signals. There are several issues to be resolved regarding the configuration of the vehicles, including the minimum number of vehicles necessary to maintain an autonomous formation, the number of transmitting and receiving sources on each vehicle, the degree of observability of a given configuration, and the range of motion over which each vehicle can receive signals from and transmit signals to the other vehicles. These matters must be further

Figure 7.7: **A Multi-vehicle Spacecraft Cluster For Deep-Space Observations**

Multiple vehicles could perform spatially-distributed science missions in deep space by using a GPS-based system for sensing relative positions to maintain formation. Each vehicle would be equipped with GPS transmitters as well as receivers in order to establish formation.

analyzed and proven on laboratory prototypes before operational systems can be planned.

- Relative positions must be maintained to less than 1 cm accuracy and relative attitudes to less than 0.05 deg accuracy. These tolerances must be met in order to engage a higher accuracy laser metrology system for alignment of science instruments. The 1 cm tolerance is based on an estimate of the control authority of the laser metrology system, and the 0.05 deg value is based on the maximum tolerable angular deviation to hit a 1 m target at a range of 1 km.

- Clocks on each spacecraft must be automatically synchronized. In order to extract range information from the GPS signals, the signals must be broadcast simultaneously. The NAVSTAR GPS satellites achieve this through atomic clocks and periodic corrections of ephemerides from ground stations. The time bias of the clocks on all vehicles in the formation will need to be resolved continuously along with the position solution.

- The dynamic range of the GPS system must extend from approximately 1 m to 1 km. Since all of the vehicles in the formation will almost certainly be launched as a single tightly packed cluster, the GPS system must function between the two extreme distances of near contact and the baseline of the fully deployed formation. This represents a dynamic range in power of 60 dB.

- The cluster of vehicles must have the ability to re-establish the formation if signal lock is momentarily lost. If any vehicle looses its place in formation, it will have to resolve the integer cycle ambiguities between itself and the other spacecraft. Techniques similar to those described in Chapter 5 could be used to re-establish the formation. For instance, an initial estimate of the stray vehicle's location could be established simply through measured signal strengths, and then motions could be induced on the stray vehicle to collect phase measurements to resolve the integers.

- The formation must operate autonomously, with only high-level commands from earth. Large communication delays to the deep space cluster lead to the obvious conclusion that the formation will have to be commanded from a very high level. Commands would be issued in a manner similar to the way the robot was commanded in this thesis, with instructions such as "point at that star" and "increase spatial resolution".

Resolution of the issues presented above will require a considerable amount of ground testing beyond theoretical analysis. The experimental apparatus used for this thesis could easily be modified and extended to serve as a proof-of-concept testbed for formation-flying spacecraft technologies. The greatest difference between the apparatus used in this thesis and the one currently under discussion is that the latter is completely self-contained, with no signals coming from external sources. This means that the pseudolite transmitters would have to be mounted on-board each of the vehicles.

The GPS *transceiver* is a recent innovation of the Stanford GPS Laboratory [10]. This device combines the functionality of a GPS receiver and a pseudolite transmitter and offers several advantages over separate transmitters and receivers[6]. There are fewer antennas since transmission and reception are time multiplexed on the same antenna. This reduces the number of line bias parameters that can drift out of calibration, as well as reducing the amount of uncertainty introduced by antenna phase center variation. Also, by combining transmitter and receiver hardware the number of clocks is reduced; thus there are fewer unknown clock biases. It is suggested that an autonomous self-regulating formation could be made feasible through the use of this type of device, and demonstrating a procedure for doing this would have several fundamental contributions to the field.

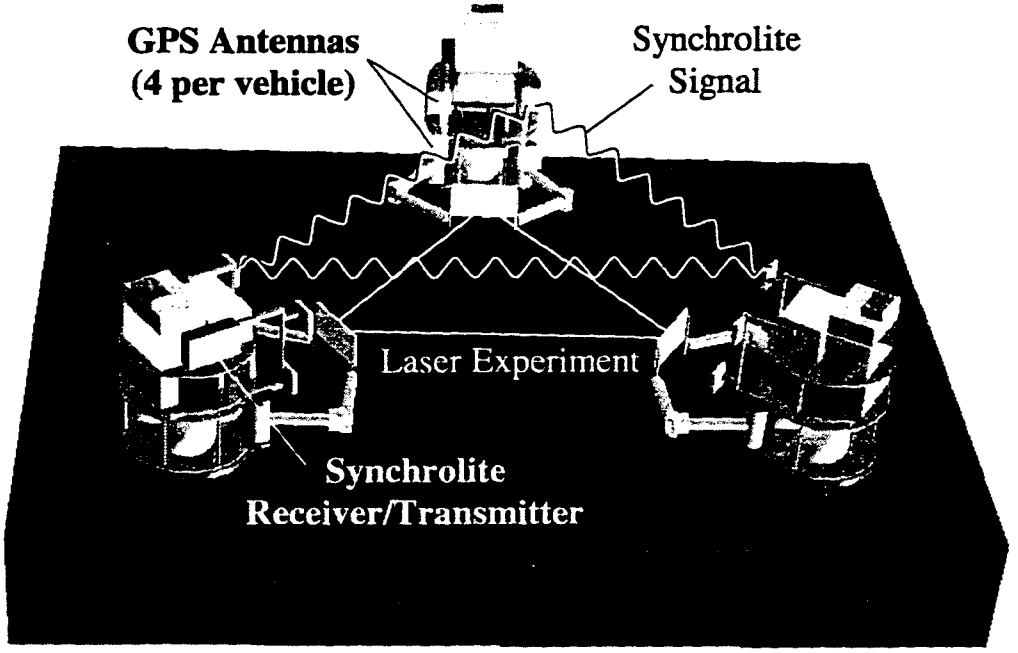

Figure 7.8: **Formation Flying with Laser Reflection Experiment**

[6]The GPS transceiver has alternatively been referred to as an "omni-marker" and a "synchrolite" by its designers

The Mars Positioning System (MPS)

Logistic studies on robotic and manned missions to Mars indicate that the planetary navigational requirements constitute a significant portion of the technical challenge [26]. It is conceivable that GPS-like systems could be employed to form the navigational infrastructure for on-going exploration of Mars. The system would essentially be an extra-planetary equivalent to NAVSTAR GPS, except the ground segment would consist of a number of GPS transceivers (or synchrolites) distributed across the surface of the planet. Placement of the system could be performed through a major, dedicated mission, or in increments as extended payloads on near-future rover missions.

The deployment of a system similar to NAVSTAR GPS around Mars would enable the exploration components of the mission to take advantage of well-proven navigational technologies used on earth. A nice feature of this system is that it could meet the navigational needs for several missions, both robotic and manned. In fact, the functionality of the system could be incrementally tested as missions progress in sophistication from short-range robotic missions to long-range robotic missions to manned exploration.

A dedicated-deployment scheme for placing such a system in orbit around Mars is shown in the rudimentary diagram of Figure 7.9. Several launches would be required, and each launch would transport a number of orbiters and ground transceivers. Distribution of the orbiters and the ground transceivers would be accomplished by slightly modifying each of their trajectories while in transit to the planet. The orbiters and ground transceivers would communicate with each other, each providing an estimate of its own position and an estimate of the other components positions. After some period of time, the positions of all the components in the system would converge and the system could then be used for navigation by exploration vehicles.

A second method for deploying components of the Mars Positioning System would be to include GPS transceivers on near-future missions, including orbiters and rovers, such as NASA's *Mars Pathfinder*. The orbiting transceivers could take advantage of the baseline spacecraft's bus for power and communication, while ground transceivers could be distributed as supplemental payloads on rovers.

The feasibility and cost of a Mars equivalent to GPS is an open research topic. An initial study might answer some basic questions:

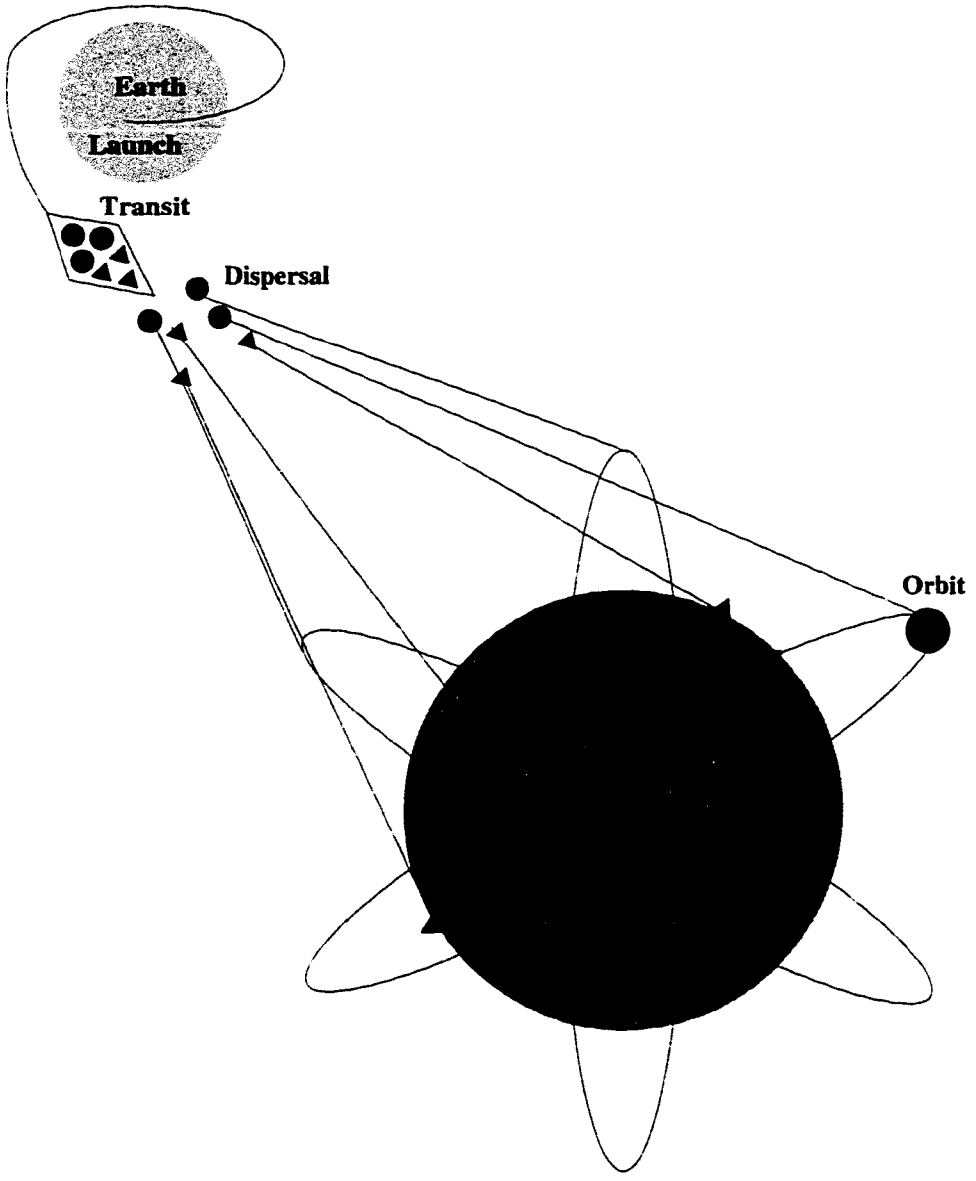

Figure 7.9: **Mars Positioning System**

This simple diagram shows the basic concept for placing a navigation system equivalent to GPS in orbit around Mars. Such a system could address a significant portion of the technical challenges of Mars exploration missions. Clusters of orbiters and ground transceivers are launched simultaneously. The vehicles are then dispersed while in transit to Mars such that they achieve different orbits and ground locations. Once in place, the components communicate with each other to refine estimates of their locations and autonomously regulate their orbits.

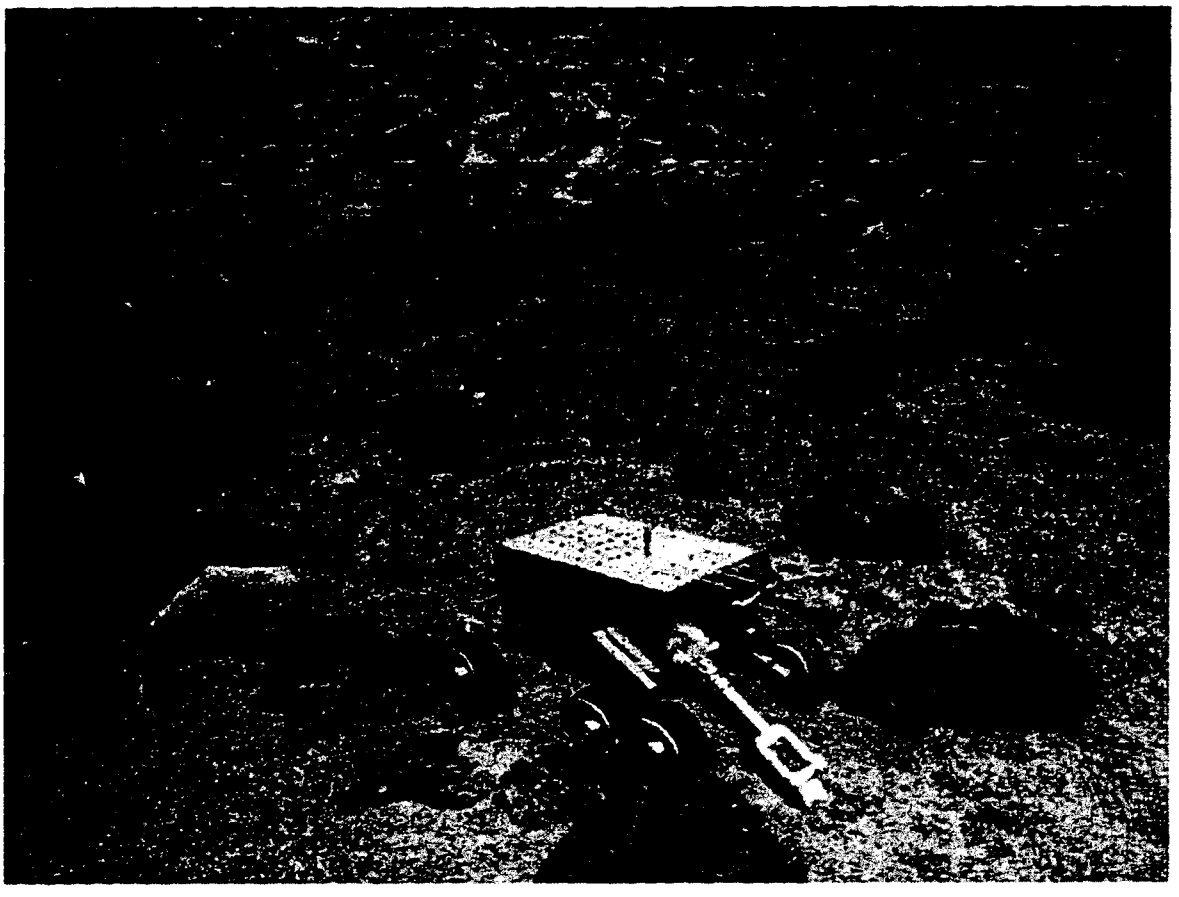

Figure 7.10: **NASA's** *Mars Pathfinder Mission*

Future versions of NASA's current Mars rovers could greatly benefit from a GPS-like navigation network around Mars. The navigation network would consist of ground-based and orbiting transceivers. Rovers might even potentially be used to deploy portions of the ground networks of GPS pseudolites to form the navigational infrastructure needed for manned exploration. Photo courtesy NASA Jet Propulsion Laboratories

- Can a system composed of several orbiting vehicles and ground transceivers actually converge on the proper locations of all components in the system? How well would the initial locations need to be known?
- How many orbiters and ground transceivers would be needed?
- What kind of accuracies could be expected from the system?
- How could the system be launched?

- Can the necessary distribution of ground transmitters and orbits be achieved?
- How would the transmitters be powered? Would solar energy suffice?
- How could redundancy best be afforded in the event of lost components?
- How would the communications network operate?
- How much would the system cost, especially in comparison with other proposed planetary navigation methods?

The technology that makes the Mars Positioning System worthy of consideration is the GPS transceiver. Advances in this technology will come about as earth-based GPS systems become more autonomous. Also, work towards reducing the maintenance costs of NAVSTAR GPS may eventually lead to a completely autonomous, self-regulating GPS system in earth orbit, from which an equivalent autonomous Mars Positioning System could be derived.

Appendix A

Near-Constellation in the Limit

This appendix demonstrates the generality of the parametric representation used in this thesis by showing that the fundamental measurement equations for the Near-Constellation system are equivalent to those for a Far-Constellations system in the limit as the transmitters are moved out to infinity.

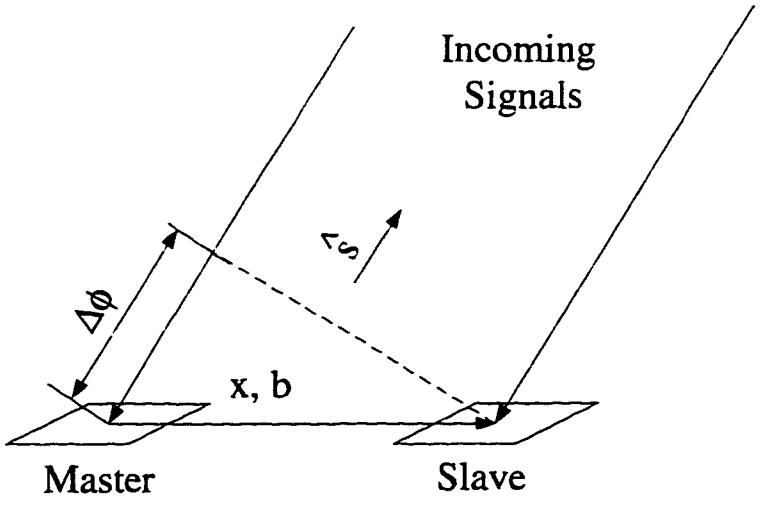

Figure A.1: **Variable Definitions for Linear Far-Constellation System**

This diagram shows the relationship between the measurements, the known parameters, and the unknown variables. $\Delta\phi$ and $\hat{s}$ are the measured differential carrier phase and line-of-sight unit vector to the satellite, b is the known baseline between the master and slave antennas in the vehicle frame, R is the unknown attitude of the vehicle, and x is the unknown baseline in the inertial frame.

Figure 3.4 shows the variable definitions for the Near-Constellation situation and Figure A.1 shows the definitions for the Far-Constellation system. To achieve the analogous situation between Figure 3.4 and Figure A.1 it is assumed that the origin of the vehicle frame and the center of the master antenna are coincident.

The intra-vehicle single-difference phase measurement equation for the Far-Constellation situation is given by:

$$\Delta\phi_{FC} = \hat{s}^T x \;=\; \hat{s}^T R b$$

The single-difference phase measurement equation for the Near-Constellation situation is given by:

$$\Delta\phi_{NC} = |(P + Rb) - Q| - |P - Q|$$

The objective is to show

$$\lim_{|P-Q|\to\infty} \Delta\phi_{NC} = \hat{s}^T R b$$

where

$$\hat{s}^T = \frac{(P-Q)^T}{|P-Q|}$$

This can be simplified to showing:

$$\lim_{|a|\to\infty} |a+b| - |a| = \frac{a^T}{|a|} b$$

Proceeding:

$$|a+b| - |a| = \frac{(a+b)^T(a+b)}{|a+b|} - \frac{a^T a}{|a|} \;=\; \frac{(a+b)^T a}{|a+b|} + \frac{(a+b)^T b}{|a+b|} - \frac{a^T a}{|a|}$$

Taking it to the limit $|a| \to \infty$:

$$= \frac{a^T a}{|a|} + \frac{a^T b}{|a|} - \frac{a^T a}{|a|} \;=\; \frac{a^T b}{|a|}$$

QED.

Appendix B

Maple Equations

The following is a list of *Maple* equations that describe the Phase-to-State mapping algorithm for the 3D reduce-dynamics case. These equations were directly converted to "C" code and used both in simulation and experiments. These *Maple* equations were generated from Matlab scripts which handled automatic indexing of all the variables. Implementation of the other algorithms derived in this thesis, including the 2D-EKF phase-to-state mapping, initialization and calibration schemes, were implemented in similar ways.

```
with(linalg):
readlib(C):
readlib(cost):
readlib(optimize):
mag := proc(a, b);
   ((a[1,1]-b[1,1])^2 + (a[2,1]-b[2,1])^2 + (a[3,1]-b[3,1])^2)^(1/2);
end:
# Antenna baseline vectors, axial directions, and orientation matrices
B11 := matrix(3, 1, [b11x, b11y, b11z]);
A11 := matrix(3, 1, [0, 0, 1]);
B12 := matrix(3, 1, [b12x, b12y, b12z]);
A12 := matrix(3, 1, [0, 0, 1]);
B13 := matrix(3, 1, [b13x, b13y, b13z]);
A13 := matrix(3, 1, [0, 0, 1]);
```

```
B14 := matrix(3, 1, [b14x, b14y, b14z]);
A14 := matrix(3, 1, [0, 0, 1]);
P1 := matrix(3, 1, [p1x, p1y, p1z]);
R1 := matrix(3, 3, [[1 - 2*e12*e12 - 2*e13*e13,
 2*(e11*e12 - e13*e14),
 2*(e11*e13 + e12*e14)],
[2*(e11*e12 + e13*e14),
 1 - 2*e11*e11 - 2*e13*e13,
 2*(e12*e13 - e11*e14)],
[2*(e11*e13 - e12*e14),
 2*(e12*e13 + e11*e14),
 1 - 2*e11*e11 - 2*e12*e12]]);
V1 := matrix(3, 1, [Q2EA1*e11, Q2EA1*e12, Q2EA1*e13]);
# Antenna positions
P11 := add(P1, multiply(R1, B11));
P12 := add(P1, multiply(R1, B12));
P13 := add(P1, multiply(R1, B13));
P14 := add(P1, multiply(R1, B14));

# Pseudolite positions
Q1 := matrix(3, 1, [q1x, q1y, q1z]);
Q2 := matrix(3, 1, [q2x, q2y, q2z]);
Q3 := matrix(3, 1, [q3x, q3y, q3z]);
Q4 := matrix(3, 1, [q4x, q4y, q4z]);
Q5 := matrix(3, 1, [q5x, q5y, q5z]);
Q6 := matrix(3, 1, [q6x, q6y, q6z]);
# Phase measurement equations
# vehicle 1, antenna 1, pseudolite 1:6
phi111 := mag(P11,Q1) + Tv1+ det(multiply(transpose(V1),A11));
phi112 := mag(P11,Q2) + Tv1+ det(multiply(transpose(V1),A11));
phi113 := mag(P11,Q3) + Tv1+ det(multiply(transpose(V1),A11));
phi114 := mag(P11,Q4) + Tv1+ det(multiply(transpose(V1),A11));
phi115 := mag(P11,Q5) + Tv1+ det(multiply(transpose(V1),A11));
```

```
phi116 := mag(P11,Q6) + Tv1+ det(multiply(transpose(V1),A11));

# vehicle 1, antenna 2, pseudolite 1:6
phi121 := mag(P12,Q1) + Tv1+ det(multiply(transpose(V1),A12));
phi122 := mag(P12,Q2) + Tv1+ det(multiply(transpose(V1),A12));
phi123 := mag(P12,Q3) + Tv1+ det(multiply(transpose(V1),A12));
phi124 := mag(P12,Q4) + Tv1+ det(multiply(transpose(V1),A12));
phi125 := mag(P12,Q5) + Tv1+ det(multiply(transpose(V1),A12));
phi126 := mag(P12,Q6) + Tv1+ det(multiply(transpose(V1),A12));

# vehicle 1, antenna 3, pseudolite 1:6
phi131 := mag(P13,Q1) + Tv1+ det(multiply(transpose(V1),A13));
phi132 := mag(P13,Q2) + Tv1+ det(multiply(transpose(V1),A13));
phi133 := mag(P13,Q3) + Tv1+ det(multiply(transpose(V1),A13));
phi134 := mag(P13,Q4) + Tv1+ det(multiply(transpose(V1),A13));
phi135 := mag(P13,Q5) + Tv1+ det(multiply(transpose(V1),A13));
phi136 := mag(P13,Q6) + Tv1+ det(multiply(transpose(V1),A13));

# vehicle 1, antenna 4, pseudolite 1:6
phi141 := mag(P14,Q1) + Tv1+ det(multiply(transpose(V1),A14));
phi142 := mag(P14,Q2) + Tv1+ det(multiply(transpose(V1),A14));
phi143 := mag(P14,Q3) + Tv1+ det(multiply(transpose(V1),A14));
phi144 := mag(P14,Q4) + Tv1+ det(multiply(transpose(V1),A14));
phi145 := mag(P14,Q5) + Tv1+ det(multiply(transpose(V1),A14));
phi146 := mag(P14,Q6) + Tv1+ det(multiply(transpose(V1),A14));


# Eliminate clock errors
# 1) First differences between master ant. and slave ant. on vehicle
# 1, for pseudolites 1:6
Dphi121 := phi111 - phi121;
Dphi122 := phi112 - phi122;
Dphi123 := phi113 - phi123;
```

```
Dphi124 := phi114 - phi124;
Dphi125 := phi115 - phi125;
Dphi126 := phi116 - phi126;
Dphi131 := phi111 - phi131;
Dphi132 := phi112 - phi132;
Dphi133 := phi113 - phi133;
Dphi134 := phi114 - phi134;
Dphi135 := phi115 - phi135;
Dphi136 := phi116 - phi136;
Dphi141 := phi111 - phi141;
Dphi142 := phi112 - phi142;
Dphi143 := phi113 - phi143;
Dphi144 := phi114 - phi144;
Dphi145 := phi115 - phi145;
Dphi146 := phi116 - phi146;

#  3) Second differences between master antenna measurements
#     of the vehicles
DDphi12 :=  phi111 - phi112;
DDphi23 :=  phi112 - phi113;
DDphi34 :=  phi113 - phi114;
DDphi45 :=  phi114 - phi115;
DDphi56 :=  phi115 - phi116;
DDphi61 :=  phi116 - phi111;
# Form the measurement equations for first differences
hs := matrix(19, 1, [
Dphi121,
Dphi122,
Dphi123,
Dphi124,
Dphi125,
Dphi126,
Dphi131,
```

```
Dphi132,
Dphi133,
Dphi134,
Dphi135,
Dphi136,
Dphi141,
Dphi142,
Dphi143,
Dphi144,
Dphi145,
Dphi146,
1-(e11*e11+e12*e12+e13*e13+e14*e14)
]);
hd := matrix(6, 1, [
DDphi12,
DDphi23,
DDphi34,
DDphi45,
DDphi56,
DDphi61]);
# Form linearized observation matrix
Hs := matrix(19, 7, [
[diff(hs[1,1], p1x), diff(hs[1,1], p1y), diff(hs[1,1], p1z),
diff(hs[1,1], e11), diff(hs[1,1], e12), diff(hs[1,1], e13),
diff(hs[1,1], e14)],
[diff(hs[2,1], p1x), diff(hs[2,1], p1y), diff(hs[2,1], p1z),
diff(hs[2,1], e11), diff(hs[2,1], e12), diff(hs[2,1], e13),
diff(hs[2,1], e14)],
[diff(hs[3,1], p1x), diff(hs[3,1], p1y), diff(hs[3,1], p1z),
diff(hs[3,1], e11), diff(hs[3,1], e12), diff(hs[3,1], e13),
diff(hs[3,1], e14)],
[diff(hs[4,1], p1x), diff(hs[4,1], p1y), diff(hs[4,1], p1z),
diff(hs[4,1], e11), diff(hs[4,1], e12), diff(hs[4,1], e13),
```

```
diff(hs[4,1], e14)],
[diff(hs[5,1], p1x), diff(hs[5,1], p1y), diff(hs[5,1], p1z),
diff(hs[5,1], e11), diff(hs[5,1], e12), diff(hs[5,1], e13),
diff(hs[5,1], e14)],
[diff(hs[6,1], p1x), diff(hs[6,1], p1y), diff(hs[6,1], p1z),
diff(hs[6,1], e11), diff(hs[6,1], e12), diff(hs[6,1], e13),
diff(hs[6,1], e14)],
[diff(hs[7,1], p1x), diff(hs[7,1], p1y), diff(hs[7,1], p1z),
diff(hs[7,1], e11), diff(hs[7,1], e12), diff(hs[7,1], e13),
diff(hs[7,1], e14)],
[diff(hs[8,1], p1x), diff(hs[8,1], p1y), diff(hs[8,1], p1z),
diff(hs[8,1], e11), diff(hs[8,1], e12), diff(hs[8,1], e13),
diff(hs[8,1], e14)],
[diff(hs[9,1], p1x), diff(hs[9,1], p1y), diff(hs[9,1], p1z),
diff(hs[9,1], e11), diff(hs[9,1], e12), diff(hs[9,1], e13),
diff(hs[9,1], e14)],
[diff(hs[10,1], p1x), diff(hs[10,1], p1y), diff(hs[10,1], p1z),
diff(hs[10,1], e11), diff(hs[10,1], e12), diff(hs[10,1], e13),
diff(hs[10,1], e14)],
[diff(hs[11,1], p1x), diff(hs[11,1], p1y), diff(hs[11,1], p1z),
diff(hs[11,1], e11), diff(hs[11,1], e12), diff(hs[11,1], e13),
diff(hs[11,1], e14)],
[diff(hs[12,1], p1x), diff(hs[12,1], p1y), diff(hs[12,1], p1z),
diff(hs[12,1], e11), diff(hs[12,1], e12), diff(hs[12,1], e13),
diff(hs[12,1], e14)],
[diff(hs[13,1], p1x), diff(hs[13,1], p1y), diff(hs[13,1], p1z),
diff(hs[13,1], e11), diff(hs[13,1], e12), diff(hs[13,1], e13),
diff(hs[13,1], e14)],
[diff(hs[14,1], p1x), diff(hs[14,1], p1y), diff(hs[14,1], p1z),
diff(hs[14,1], e11), diff(hs[14,1], e12), diff(hs[14,1], e13),
diff(hs[14,1], e14)],
[diff(hs[15,1], p1x), diff(hs[15,1], p1y), diff(hs[15,1], p1z),
diff(hs[15,1], e11), diff(hs[15,1], e12), diff(hs[15,1], e13),
```

```
diff(hs[15,1], e14)],
[diff(hs[16,1], p1x), diff(hs[16,1], p1y), diff(hs[16,1], p1z),
diff(hs[16,1], e11), diff(hs[16,1], e12), diff(hs[16,1], e13),
diff(hs[16,1], e14)],
[diff(hs[17,1], p1x), diff(hs[17,1], p1y), diff(hs[17,1], p1z),
diff(hs[17,1], e11), diff(hs[17,1], e12), diff(hs[17,1], e13),
diff(hs[17,1], e14)],
[diff(hs[18,1], p1x), diff(hs[18,1], p1y), diff(hs[18,1], p1z),
diff(hs[18,1], e11), diff(hs[18,1], e12), diff(hs[18,1], e13),
diff(hs[18,1], e14)],
[diff(hs[19,1], p1x), diff(hs[19,1], p1y), diff(hs[19,1], p1z),
diff(hs[19,1], e11), diff(hs[19,1], e12), diff(hs[19,1], e13),
diff(hs[19,1], e14)]]);
Hd := matrix(6, 7, [
[diff(hd[1,1], p1x), diff(hd[1,1], p1y), diff(hd[1,1], p1z),
diff(hd[1,1], e11), diff(hd[1,1], e12), diff(hd[1,1], e13),
diff(hd[1,1], e14)],
[diff(hd[2,1], p1x), diff(hd[2,1], p1y), diff(hd[2,1], p1z),
diff(hd[2,1], e11), diff(hd[2,1], e12), diff(hd[2,1], e13),
diff(hd[2,1], e14)],
[diff(hd[3,1], p1x), diff(hd[3,1], p1y), diff(hd[3,1], p1z),
diff(hd[3,1], e11), diff(hd[3,1], e12), diff(hd[3,1], e13),
diff(hd[3,1], e14)],
[diff(hd[4,1], p1x), diff(hd[4,1], p1y), diff(hd[4,1], p1z),
diff(hd[4,1], e11), diff(hd[4,1], e12), diff(hd[4,1], e13),
diff(hd[4,1], e14)],
[diff(hd[5,1], p1x), diff(hd[5,1], p1y), diff(hd[5,1], p1z),
diff(hd[5,1], e11), diff(hd[5,1], e12), diff(hd[5,1], e13),
diff(hd[5,1], e14)],
[diff(hd[6,1], p1x), diff(hd[6,1], p1y), diff(hd[6,1], p1z),
diff(hd[6,1], e11), diff(hd[6,1], e12), diff(hd[6,1], e13),
diff(hd[6,1], e14)]]);
C(hs, optimized);
```

```
cost(optimize(hs));
C(hd, optimized);
cost(optimize(hd));
C(Hs, optimized);
cost(optimize(Hs));
C(Hd, optimized);
cost(optimize(Hd));
```

Appendix C

An Algorithm for Visual Tracking in Three-Dimensions

GPS sensing can be combined with a local vision sensor to create an overall more robust system. In 1992 Kemper and Zimmerman implemented an algorithm to track objects in three dimensions, six-degrees of freedom using the robot's on-board local vision system. It was found that this technique worked quite well, even for large angular deflections of the viewed object. The algorithm was developed by Hung, Yeh, and Hartwood [48] required certain assumptions and knowledge of the object to be tracked:

- The pattern is a planar quadrangle.
- The distance between each of the of the points on the object are known.
- Each point can be uniquely distinguished from the others (for initial identification).

The raw data that obtained from the vision system was merely a set of points and their coordinates, as observed by the camera on its image plane. These points needed to be correlated to the appropriate points on the object before the algorithm could convert them to range/orientation information.

To simplify the process of distinguishing the points on the object, the object was outfitted with *five* Light Emitting Diodes (LEDs). Four were located at the vertices of a square, and the fifth one was located inline with one pair and closer to one of the pair, as shown in Figure C.1.

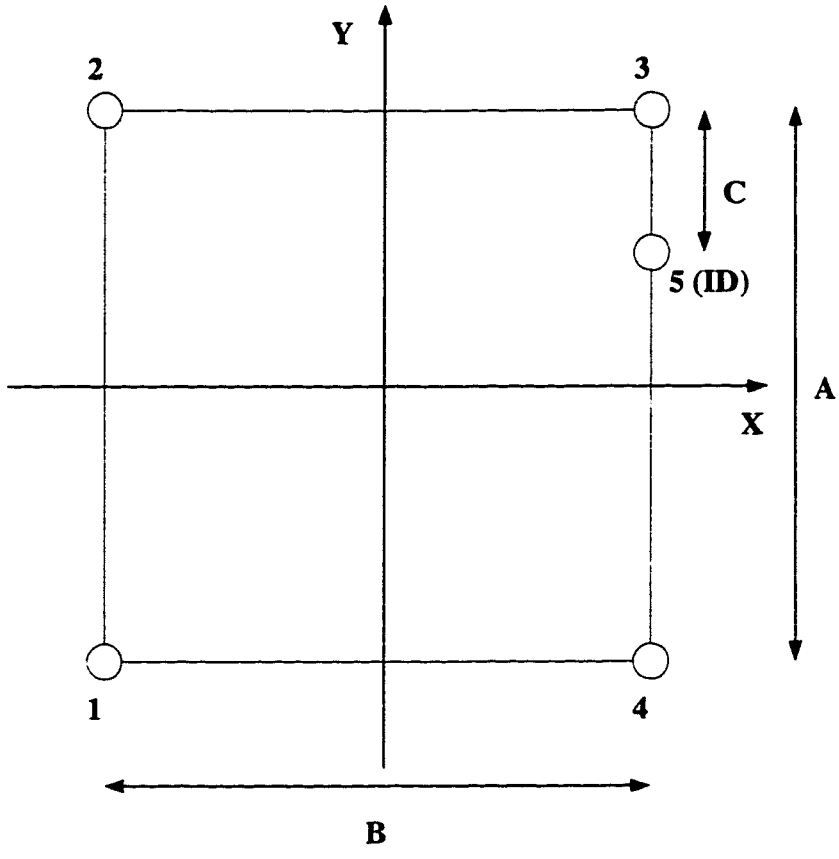

Figure C.1: **Fiducial Markings on Object for Visual Sensing in Three Dimensions**

Five LEDs were used as fiducial markings on an object to be visually tracked in three dimensions. The algorithm requires four coplanar points, and a fifth was added to simplify the process of uniquely identifying each of the LEDs from the camera's image-plane measurements

After the points were all identified, their coordinates in the camera image-plane were supplied as inputs to the algorithm, and the corresponding three-dimensional position and orientation of the object in the robot frame were generated.

Identification of the points to their corresponding place on the oject was accomplished as follows:

1. Start with a set of five unordered points, pp[0-4], determine their correspondence to the five points on the object corner[0-3] and extraLED.

2. Determine which three of the five points are in a line:

```
found = FALSE;
foundagain = FALSE;

pp[0] = &p1;
pp[1] = &p2;
pp[2] = &p3;
pp[3] = &p4;
pp[4] = &p5;

ii = -1;
while((ii<2) && !foundagain) {
  ii++;
  jj = ii;
  while ((jj<3) && !foundagain) {
    jj++;
    kk = jj;
    while ((kk<4) && !foundagain) {
      kk++;
      sub(pp[ii],pp[jj],&tmp1);
      sub(pp[jj],pp[kk],&tmp2);
      cross(&tmp1,&tmp2,&tmp3);
      if (dot(&tmp3,&tmp3) < TOL) {      /* points are in line */
        if (!found) {
          found = TRUE;
        } else {
          foundagain = TRUE;             /* too many points in line */
          found = FALSE;
        }
        i=ii;
        j=jj;
        k=kk;
      }
```

```
    }
  }
}
```

3. Order the three colinear points based on the ratio of the lengths of the vectors subtended by the points.

```
if (found) {
  lenij = sqrt(dot(&tmp1,&tmp1));
  lenjk = sqrt(dot(&tmp2,&tmp2));
  ratio = lenij/lenjk;
  if (dot(&tmp1,&tmp2) > 0) {        /* ijk or kji */
    extraLED = j;
    if (ratio>1) {                   /* kji */
      corner3 = k;
      corner4 = i;
      id = 1/(1+ratio);
    } else {                         /* ijk */
      corner3 = i;
      corner4 = k;
      id = ratio/(1+ratio);
    }
  } else {                           /* ikj, jki, jik, or kij */
    if (ratio>2) {                   /* jki */
      corner3 = j;
      corner4 = i;
      extraLED = k;
      id = 1/ratio;
    } else if (ratio>1) {            /* ikj */
      corner3 = i;
      corner4 = j;
      extraLED = k;
```

```
    id = (ratio-1)/ratio;
  } else if (ratio>0.5) {          /* kij */
    corner3 = k;
    corner4 = j;
    extraLED = i;
    id = 1-ratio;
  } else {                         /* jik */
    corner3 = j;
    corner4 = k;
    extraLED = i;
    id = ratio;
  }
}
```

4. Now that the three colinear point have been properly ordered, the other two must be considered. Corners 1 and 2 form a line nearly parallel to 3 and 4. The dot product of the vectors (12) and (34) will be positive if they are parallel and negative if antiparallel.

```
corner1=0;
while((corner1==i) || (corner1==j) || (corner1==k))
  {corner1++;}
corner2=corner1+1;
while((corner2==i) || (corner2==j) || (corner2==k))
  {corner2++;}

sub(pp[corner1],pp[corner2],&tmp1);
sub(pp[corner3],pp[corner4],&tmp2);
if (dot(&tmp1,&tmp2)>0) {
  temp = corner1;
  corner1 = corner2;
  corner2 = temp;
```

```
    }
    sprintf(pointState1.name,"point%d",corner1+1);
    sprintf(pointState2.name,"point%d",corner2+1);
    sprintf(pointState3.name,"point%d",corner3+1);
    sprintf(pointState4.name,"point%d",corner4+1);
    sprintf(pointState5.name,"point%d",extraLED+1);
  } else {
    if (foundagain) {
      printf("Found too many colinear points!\n");
    } else {
      printf("Could not find three colinear points!\n");
    }
  }
```

Bibliography

[1] P. Axelrad and B.W. Parkinson. Closed loop navigation and guidance for gravity probe b orbit insersion. *Journal of the Institute of Navigation*, 36(1):45–61, Spring 1989.

[2] Constantine A. Balanis. *Antenna Theory, Analysis and Design.* Harper and Row, New York NY, 1982.

[3] Gary H. Blackwood and M. Mark Colavita. Technology development for separated spacecraft interferometers. A Proposal by the Jet Propulsion Laboratory to the New Millenium Technology for Interuments and Microelectromechanical Systems (MEMS) IPDT, June 1995.

[4] James J. Spilker Bradford W. Parkinson. *Global Positioning System: Theory and Application.* American Institute of Aeronautics and Astronautics, Inc., Washington, DC, 1996.

[5] P.E. Braisted and R.F. Eschenback. Global positioning system coarse acquisition code receiver: Differential phase measurement system, 1989. United States Patent 4,847,862.

[6] Vincent W. Chen. *Experiments in Adaptive Control of Multiple Cooperating Manipulators on a Free-Flying Space Robot.* PhD thesis, Stanford University, Stanford, CA 94305, December 1992. Also published as SUDAAR 631.

[7] Thomas Clark. Personal correspondence, July 1996.

[8] Clark E. Cohen, B. Pervan, et. al. Real-Time Flight Test Evaluation of the GPS Marker Beacon Concept for Category III Kinematic GPS Precision Landing. In *Proceedings of the Institute of Navigation GPS-93 Conference*, Salt Lake City UT, September 1993.

[9] Clark E. Cohen, Boris Pervan, et. al. Flight Test Results of Autocoupled Approaches Using GPS and Integrity Beacons. In *Proceedings of the Institute of Navigation GPS-93 Conference*, Salt Lake City UT, September 1994.

[10] H. S. Cobb. *Theory, Design, and Applications of GPS Pseudo-Satellites.* PhD thesis, Stanford University, Department of Aeronautics and Astronautics, Stanford, CA 94305, Publication Pending 1996.

[11] Clark Emerson Cohen. *Attitude Determination Using GPS.* PhD thesis, Stanford University, Department of Aeronautics and Astronautics, Stanford, CA 94305, December 1992.

[12] Andrew R. Conway. *Autonomous Control of an Unstable Helicopter Using Carrier Phase GPS Only.* PhD thesis, Stanford University, Stanford, CA 94305, March 1995. Also published as SUDAAR 664.

[13] John J. Craig. *Introduction to Robotics.* Addison Wesley, Menlo Park CA, 1989.

[14] David Lawrence, H. Stewart Cobb, et. al. Maintaining GPS Positioning in Steep Turns Using Two Antennas. In *Proceedings of the Institute of Navigation GPS-95 Conference*, Palm Springs CA, September 1995.

[15] William C. Dickson. *Experiments in Cooperative Manipulation of Objects by Free-Flying Robot Teams.* PhD thesis, Stanford University, Department of Aeronautics and Astronautics, Stanford, CA 94305, December 1993. Also published as SUDAAR 643.

[16] Don Knight. A New Method of Instantaneous Ambiguity Resolution. In *Proceedings of the Institute of Navigation GPS-94 Conference*, Salt Lake City UT, September 1994.

[17] Frank Bauer, E. Glenn Lightsey, et. al. Pre-Flight Testing of the SPARTAN GADACS Experiment. In *Proceedings of the Institute of Navigation GPS-94 Conference*, Salt Lake City UT, September 1994.

[18] Arthur Gelb. *Applied Optimal Estimation.* The M.I.T. Press, Cambridge MA, 1986.

[19] J. Kurt Brock, Rich Fuller, Brian Kemper, Dave Mleczko, et. al. GPS Attitude Determination and Navigation Flight Experiment. In *Proceedings of the Institute of Navigation GPS-95 Conference*, Palm Springs CA, September 1995.

[20] Warren Jasper. *Experiments in Thrusterless Robot Locomotion Control for Space Applications.* PhD thesis, Stanford University, Stanford, CA 94305, September 1990. Also published as SUDAAR 595.

[21] John Carl Adams, Andrew Robertson, Johnathan How, Kurt R. Zimmerman. Technologies for Spacecraft Formation Flying. In *Proceedings of the Institute of Navigation GPS-96 Conference*, Kansas City MO, September 1996.

[22] A. Wayne Deaton Jorge I. Galdos, Triveni N. Upadhyay and James J. Lomas. GPS Relative Navigation for Automatic Spacecraft Rendezvous and Capture. In *Proceedings of the National Telesystems Conference*, Atlanta GA, June 1993.

[23] K.M. Joseph and P.S. Deem. Precision orientation: A new gps application. In *Proceedings of the International Telemetering Conference*, San Diego CA, October 1983.

[24] Ross Koningstein. *Experiments in Cooperative-Arm Object Manipulation with a Two-Armed Free-Flying Robot.* PhD thesis, Stanford University, Department of Aeronautics and Astronautics, Stanford, CA 94305, October 1990. Also published as SUDAAR 597.

[25] E. G. Lightsey. *Development and Application of a GPS Receiver for Space.* PhD thesis, Stanford University, Department of Aeronautics and Astronautics, Stanford, CA 94305, Publication Pending 1996.

[26] Steve Merrihew. Personal correspondence, August 1996.

[27] Paul Y. Montgomery. *Carrier Differential GPS As a Sensor For Automatic Control: Development of a Full-State Estimation and Flight Control System for an Autonomous Aircraft Based on the Global Positioning System.* PhD thesis, Stanford University, Stanford, CA 94305, August 1996. Also published as SUDAAR 688.

[28] Geoffrey A. Moore. *Crossing the Chasm.* HarperBusiness, New York, NY, 1995.

[29] NAVSTAR. GPS Interface Control Document ICD-GPS-200. NAVSTAR Technical Document IRN-200B-PR-001, ARINC Research Corporation, July 1992.

[30] O. Leisten and G. Ffoulkes-Jones. Performance of a Miniature Dialetrically Loaded Volute Antenna. In *Proceedings of the Institute of Navigation GPS-95 Conference*, Palm Springs CA, September 1995.

[31] G. Pardo-Castellote and S. A. Schneider. The Network Data Delivery Service: Real-Time Data Connectivity for Distributed Control Applications. In *Proceedings of the International Conference on Robotics and Automation*, San Diego, CA, May 1994. IEEE, IEEE Computer Society.

[32] Real-Time Innovations, Inc., 954 Aster, Sunnyvale, CA 94086. *StethoScope Real-Time Graphical Monitoring and Data Collection Utility User's Manual*, 3.2 edition, December 1990.

[33] Real-Time Innovations, Inc., 954 Aster, Sunnyvale, CA 94086. *ControlShell: Object-Oriented Framework for Real-Time System Software User's Manual*, 4.0a edition, June 1991.

[34] Real-Time Innovations, Inc., 954 Aster, Sunnyvale, CA 94086. *NDDS: The Network Data-Delivery Service User's Manual*, 1.7 edition, November 1994.

[35] J. Russakow. *Experiments in Manipulation and Assembly by Two-Arm, Free-Flying Space Robots.* PhD thesis, Stanford University, Stanford, CA 94305, December 1995. Also published as SUDAAR 674.

[36] S. Schneider. *Experiments in the Dynamic and Strategic Control of Cooperating Manipulators.* PhD thesis, Stanford University, Stanford, CA 94305, September 1989. Also published as SUDAAR 586.

[37] S. A. Schneider. Real-time innovations, inc. 954 Aster, Sunnyvale, CA. email: info@rti.com.

[38] S. A. Schneider, V. W. Chen, and G. Pardo-Castellote. ControlShell: A Real-Time Software Framework. In *Proceedings of the AIAA/NASA Conference on Intelligent Robots in Field, Factory, Service and Space*, volume II, pages 870–7, Houston, TX, March 1994. AIAA, AIAA.

[39] Thomas A. Clark Bruce R. Schupler and Roger L. Allshouse. Signal characteristics of gps user antennas. *Journal of the Institute of Navigation*, 41(3):277–295, Fall 1994.

[40] H.D. Stevens, E.S. Miles, S. M. Rock, and R.H. Cannon. Object-Based Task-Level Control: A Hierarchical Control Architecture for Remote Operation of Space Robots.

In *Proceedings of the AIAA/NASA Conference on Intelligent Robotics in Field, Factory, Service, and Space*, pages 264–73, Houston TX, March 1994.

[41] Susan Gomez, Robert Panneton, Penny Saunders, et. al. GPS Mulitpath Modeling and Verification Using Geometrical Theory of Diffraction. In *Proceedings of the Institute of Navigation GPS-95 Conference*, Palm Springs CA, September 1995.

[42] Oceaneering Space Systems. Space station/office of advanced concepts and technology robotics technology study, September 1993. Prepared by OSS and McDonnnell Douglas Aerospace for Space Station Level I Code DE Engineering Prototype Development and The Office of Advanced Concepts and Technology Telerobotics Program.

[43] H. Teague. *Flexible Structure Estimation and Control Using GPS.* PhD thesis, Stanford University, Department of Aeronautics and Astronautics, Stanford, CA 94305, Publication Pending 1997.

[44] Tony Haddrell. The XR5-PC12 - Position and Time/Frequency from a Single Plug-in Module. In *Proceedings of the Institute of Navigation GPS-95 Conference*, Palm Springs CA, September 1995.

[45] M. A. Ullman. *Experiments in Autonomous Navigation and Control of Multi-Manipulator Free-Flying Space Robots.* PhD thesis, Stanford University, Stanford, CA 94305, March 1993. Also published as SUDAAR 630.

[46] David Wells. *Guide to GPS Positioning.* Canadian GPS Associates, Ottawa, Ontario, Canada, 1986.

[47] Edward Wilson. *Experiments in Neural Network Control of a Free-Flying Space Robot.* PhD thesis, Stanford University, Stanford, CA 94305, March 1995.

[48] Y. Hung, P. Yeh, and D. Harwood. Passive Ranging to Known Planar Point Sets. Computer Science Technical Report Series N00014-83-K-0236, Center for Automation Research, University of Maryland, June 1984.

[49] Yves Theroux. Open-Architecture Design for GPS Applications. In *Proceedings of the Institute of Navigation GPS-95 Conference*, Palm Springs CA, September 1995.

[50] K. R. Zimmerman and R. H. Cannon Jr. GPS-Based Control for Space Vehicle Rendezvous. In *Proceedings of the ASCE: Robotics for Challenging Environments*, Albuquerque NM, February 28 - March 3 1994.

[51] K. R. Zimmerman and R. H. Cannon Jr. GPS-Based Control for Space Vehicle Rendezvous. In *Proceedings of the Institute of Navigation GPS-94 Conference*, Salt Lake City UT, September 1994.

[52] Lubomyr V. Zyla and Moises N. Montez. Use of two gps receivers in order to perform space vehicle rendezvous. In *Proceedings of the Institute of Navigation GPS-93 Conference*, Salt Lake City UT, September 1993.